

MASTER'S THESIS
CHAIR OF THEORETICAL SOLID STATE PHYSICS
FACULTY OF PHYSICS
LUDWIG-MAXIMILIANS-UNIVERSITÄT MÜNCHEN



**Towards exploiting non-abelian symmetries
in
the Dynamical Mean-Field Theory
using
the Numerical Renormalization Group**

Katharina Maria Stadler
March 28, 2013

Supervisor:
Prof. Dr. Jan von Delft

MASTERARBEIT
LEHRSTUHL FÜR THEORETISCHE FESTKÖRPERPHYSIK
FAKULTÄT FÜR PHYSIK
LUDWIG-MAXIMILIANS-UNIVERSITÄT MÜNCHEN



**Zur Ausnutzung nicht-abelscher Symmetrien
in
der Dynamischen Molekularfeldtheorie
unter Anwendung
der Numerischen Renormalisierungsgruppe**

Katharina Maria Stadler
28. März 2013

Betreuer:
Prof. Dr. Jan von Delft

Name	Katharina Stadler
Studienrichtung	Master Physik
E-Mail	Katharina.M.Stadler@physik.uni-muenchen.de

Erklärung

Hiermit erkläre ich, die vorliegende Arbeit selbstständig verfasst zu haben und keine anderen als die in der Arbeit angegebenen Quellen und Hilfsmittel benutzt zu haben.

München, 28. März 2012

Katharina Stadler

Acknowledgement

I would like to thank Jan von Delft for the opportunity to write my master thesis in his group. I could gather a great deal of experience during the last year. In particular, the trip to Paris was a true enrichment. In this regard, I thank Michel Ferrero and the group of Antoine Georges for three great and informative days in the Ecole Polytechnique and for providing QMC data. My special thanks goes to Andreas Weichselbaum, who is a deeply committed and patient supervisor. I really learned a lot in numerous intensive discussions. In particular, I would also like to thank Markus Hanl, whom I could ask so many questions and who explained all the basics to me. A big thank you goes to my roommate Katharina Eissing for a really great time with a lot of coffee, tea and conversations. And last but not least, I thank all group members and our secretary, Stéphane Schoonover.

Contents

1	Introduction	1
2	Dynamical Mean-Field Theory (DMFT)	5
2.1	Basic idea of DMFT	6
2.2	Model Hamiltonians	8
2.2.1	The Hubbard model	8
2.2.2	Model Hamiltonians from the local density approach (LDA)	9
2.3	Derivation of the DMFT equations	9
2.3.1	Local nature of the self-energy in infinite dimensions	9
2.3.2	On-site lattice Green's function	12
2.3.3	Non-interacting lattice density of states	13
2.3.4	Mapping onto an effective quantum impurity model	15
2.3.5	The self-consistency procedure	17
3	Numerical Renormalization Group (NRG)	21
3.1	Basic method	22
3.1.1	Single impurity Anderson Hamiltonian (SIAM)	22
3.1.2	Logarithmic discretization	23
3.1.3	Mapping onto the Wilson tight-binding chain	25
3.1.4	Iterative renormalization group procedure	27
3.1.5	Renormalization group flow	30
3.2	NRG in Matrix Product State (MPS) formulation	31
3.2.1	Basis states in terms of MPS	31
3.2.2	Abelian and non-abelian symmetries	32
3.2.3	Complete basis sets and full density matrix NRG	33
3.2.4	Calculation of spectral functions	34
3.2.5	Discarded weight in NRG	36
4	Combining DMFT and NRG	39
4.1	Calculation of the self-energy	39
4.2	The logarithmic discretization grid within DMFT	41
4.2.1	Variation of the conventional logarithmic discretization grid	41
4.2.2	Zitko's adaptive logarithmic discretization grid	49
5	One-band Hubbard model	55
5.1	The Mott-Hubbard metal-insulator transition (MIT)	57
5.2	Fermi-liquid theory	63

CONTENTS

5.3	Fermi liquid physics and resilient quasiparticles	65
6	Two-band Hubbard-Kanamori model	73
6.1	Realistic modeling of strongly correlated materials	73
6.2	The DMFT equations for multi-band models	76
6.3	Hund's coupling in the two-band Hubbard-Kanamori model	78
6.3.1	The two-band Hubbard-Kanamori Hamiltonian in the context of DMFT and NRG	78
6.3.2	The effect of Hund's coupling on the metal-insulator transition (MIT) . .	80
6.3.3	Comparison of NRG and Quantum Monte Carlo results	86
7	Conclusion and Outlook	91
	Appendix	93
A	Equation of motion for the retarded Green's function	93
B	$G_{\text{latt}}(\omega)$ for a multi-band model	95
C	$G_{\text{imp}}(\omega)$ and $\Sigma(\omega)$ for a multi-band model	97
D	G_{latt} and non-interacting DOS for the Bethe lattice	101
	Bibliography	105

Chapter 1

Introduction

The realistic description of strongly correlated materials, especially in three dimensions, is a huge challenge in condensed-matter physics. As the strength of electron-electron interactions is comparable to or larger than the kinetic energy, perturbative methods cannot be applied to these materials.

Strongly correlated materials typically exhibit partially filled d- or f-shells which are associated with narrow bandwidths of only a few electron-volts. Examples are transition metals and their oxides (especially the 3d-shell from Ti to Cu and also the 4d-shell from Zr to Ag), rare earth and actinide elements (4f-shell from Ce to Yb and 5f from Th to Lr) but also certain organic compounds [1]. Since the d- and f-orbitals are spatially more confined than the s- or p-shells of simple metals or semiconductors, the overlap between orbitals of neighboring atoms is smaller, which leads to narrow bands and accordingly lower kinetic energies. Thus, on average, electrons reside longer on one atomic orbital, enhancing electron-electron interactions. This implies that the electron motion is dominated by strong correlation effects.

These correlations give rise to intriguing quantum many-body phenomena like the metal-insulator transition from a high-conductivity to an insulating phase (as in V_2O_3), itinerant (anti)ferromagnetism (like in iron and nickel), large thermoelectric response, volume changes across phase transitions (in actinides and lanthanides), the colossal magnetoresistance effect (in manganites) and high temperature superconductors [2]. A very basic observation is the Mott phenomenon which describes the localization of electrons as a consequence of strong Coulomb repulsion. Even high temperature cuprate superconductors are widely assumed to be doped Mott insulators [3]. The investigation of these fascinating strong correlation effects is a challenging task for most analytical and numerical methods, as several competing mechanisms dominate the physics for a wide range of energy scales and lead to a nonperturbative nature of the many-body problem.

The Dynamical Mean-Field Theory (DMFT) [4] provides a nonperturbative many-body approach to strongly correlated systems. It has been developed over the last 25 years and is one of the most successful approaches for treating both local correlations and band structure information on an equal footing.

Within the DMFT framework, one maps a *lattice* model onto an *effective single-site* quantum impurity model in a *self-consistent* manner. Like in the Weiss mean-field theory of classical statistical mechanics, spatial fluctuations are frozen out by this process, which leads to a purely local self-energy within DMFT. However, in contrast to the classical case where *all* fluctuations are neglected, the DMFT approach fully incorporates local quantum fluctuations in the quantum

impurity problem, thus capturing the local dynamics of the many-body problem. Although, this mapping is exact in the limit of infinite lattice coordination number only, it may be regarded as a useful approximation for three-dimensional systems.

For quantum impurity models several non-perturbative methods exist, such as Quantum Monte Carlo simulations (QMC) or the Numerical Renormalization Group (NRG) approach. Quantum Monte Carlo codes are widely used and have been highly refined over the last few decades. However, the data is obtained on the imaginary (Matsubara) frequency axis and has to be analytically continued to the real axis, a procedure that is mathematically ill-defined in principle, and in practice notoriously difficult to perform accurately, especially for complex models. Furthermore, possible limitations are very low temperatures and also the so called “sign problem” for fermionic systems. In contrast, the NRG method allows to calculate physical quantities directly on the real frequency axis. It is able to provide reliable data for effectively zero temperature and thus is worth exploiting as an alternative to Quantum Monte Carlo approaches.

In combination with ab-initio band-structure calculations, DMFT has proved to be a successful method for the investigation of realistic strongly correlated materials. Nevertheless, this technique has to be improved further to deal with increasingly complex systems, requiring in turn, more efficient solvers for the effective quantum impurity model.

In this thesis, the Numerical Renormalization Group code, that has been developed by Andreas Weichselbaum in the group of Jan von Delft at the Ludwig-Maximilians-Universität München, is used as impurity solver within the Dynamical Mean-Field Theory. It is one of the most evolved codes in the field of NRG. Using the full density matrix approach with complete many-body basis sets, it can handle arbitrary temperatures [5]. Moreover, it is, to date, the only NRG framework, that is able to exploit arbitrary abelian and non-abelian symmetries, which leads to a significant reduction of numerical effort and makes it highly suitable for the investigation of multi-band models in the presence of intrinsic symmetries such as channel symmetry. The goal of this work is to explore the potential of our program in the context of DMFT.

The outline of this thesis is as follows. In Chapter 2, the concept of the Dynamical Mean-Field Theory is presented. It can be regarded as an extension of the classical mean-field theory to quantum many-body problems. We explain the underlying physical ideas of the DMFT method by taking the example of the one-band Hubbard model, the most fundamental model for strongly correlated materials. Later on, we also refer to its applicability to more complex model Hamiltonians, as provided by the local density approach (LDA), an ab-initio band structure calculation technique. The basic approximation within DMFT is to use a purely local self-energy. In the limit of infinite lattice coordination, this approximation becomes exact, which can be rationalized using a scaling argument in perturbation theory. Beside the local self-energy, another important quantity within DMFT, the local retarded lattice Green’s function, is introduced. The significance of the lattice type under consideration is discussed afterwards. Finally, we show how the lattice model can be mapped onto a single-site quantum impurity model by a self-consistent procedure.

At the beginning of Chapter 3, we review the basics of the Numerical Renormalization Group method. In a second part, we concentrate on more recent developments in the field of NRG and concisely present the outstanding features of our NRG program, including the incorporation of arbitrary abelian and non-abelian symmetries, the implementation of a complete many-body basis set, the full density matrix approach for finite temperatures and the definition of a discarded weight within NRG.

In Chapter 4, we reveal the peculiarities that emerge, when combining the DMFT and NRG approach. First, we review how to calculate the self-energy within NRG. Thereafter, we discuss

variations of the NRG logarithmic discretization grid, that are required when NRG is employed within DMFT. This is followed by a first consistency check for our DMFT+NRG program, using the one-band Hubbard model in Chapter 5. We investigate the Mott-Hubbard metal-insulator transition which occurs for an integer filling of the lattice. Then we reproduce several results for a hole-doped system, given in [6], on a quantitative level.

As a major application, we study the two-band Hubbard-Kanamori model in Chapter 6. A short introduction to the ideas of realistic modeling of strongly correlated materials reveals to what extent a two-band model is appropriate to describe transition metal compounds. Before investigating the two-band Hubbard-Kanamori Hamiltonian in detail, including an analysis of possible symmetries of the system, we extend the DMFT equations to multi-band models. Special attention is directed to the effect of Hund's coupling on the metal-insulator transition in the two-band model. Finally, we explicitly compare NRG to QMC results. Note that all QMC data were kindly provided by our collaborator Michel Ferrero from the Centre de Physique Théorique, Ecole Polytechnique, France (thus labeled with MF).

The thesis is completed by evaluating the present stage of our DMFT+NRG program and giving a brief outlook to possible future directions.

Chapter 2

Dynamical Mean-Field Theory (DMFT)

The first step towards the Dynamical Mean-Field Theory (DMFT) was given by W. Metzner and D. Vollhardt in 1989. In their pioneering work [7] they studied the Hubbard model of correlated lattice fermions in the limit of infinite dimensions. With properly applied scaling of the Hamiltonian, diagrammatic treatments are drastically simplified compared to finite dimensions, while the competing physical mechanism between the kinetic energy and the electron-electron interaction is maintained. This new limit of infinite lattice coordination gave better insight to different approximation schemes for strongly correlated problems.

The basic DMFT framework was established in 1992 by A. Georges and G. Kotliar [8]. They extended the idea of the classical mean-field theory to quantum many-body problems and mapped the complex quantum lattice problem onto a single-site effective problem - the quantum impurity (Anderson) model, that consists of a correlated local impurity system with a small number of degrees of freedom, coupled to a macroscopic non-interacting bath, whose structure has to be determined in a self-consistent manner. The quantum impurity model can be solved with previously developed methods (such as Monte Carlo or NRG). In the limit of infinite dimensions, the mapping can be carried out exactly.

That construction led to an intensive investigation of various model Hamiltonians and opened a new direction of research, including the study of realistic models of strongly correlated materials. Here material specific informations, like several orbitals, the actual lattice type and the corresponding density of states, are taken into account. A recent extension of the DMFT method, called Cluster-DMFT, accounts for short-range spatial correlations and is able to treat inhomogeneous materials, such as disordered alloys, thin films or multi-layered nanostructures [9],[10, Chapter 1]. A detailed review of the Dynamical Mean-Field Theory and its applications is provided by A. Georges, G. Kotliar, W. Krauth and M.J. Rozenberg in [4]. An introduction to DMFT in the context of realistic modeling of strongly correlated materials can be found in [10].

2.1 Basic idea of DMFT

To understand the basic ideas of the Dynamical Mean-Field Theory for quantum lattice problems, it is advisable to revisit the underlying physical concept of the mean-field theory for the familiar classical Ising model

$$H = \sum_{\langle ij \rangle} J_{ij} S_i S_j - h \sum_i S_i \quad (2.1)$$

with ferromagnetic coupling $J_{ij} > 0$ between spins of different neighboring lattice sites i and j and an external magnetic field h . The number of nearest neighbors defines the coordination number z .

The main notion of the mean-field approach is to reduce a complex lattice model to a single site problem with effective parameters, that exhibits less degrees of freedom. The dynamics of the whole lattice is then represented by the interaction of the degrees of freedom at the single site with an external field, the Weiss effective field, which is comprised of all the other degrees of freedom at the other sites. The effective single site Hamiltonian can be written in terms of the Weiss field h_{eff} and the spin degree of freedom at a given site $i = 0$:

$$H_{\text{eff}} = - \left(\sum_{\langle j \rangle} J_{ij} \langle S \rangle_j + h \right) S_0 = - (zJm + h) S_0 = -h_{\text{eff}} S_0. \quad (2.2)$$

The effective bath h_{eff} is obtained by neglecting correlated spin fluctuations

$$\langle [S_i - \langle S \rangle][S_j - \langle S \rangle] \rangle = 0, \quad (2.3)$$

which leads to the thermal average of the magnetization $\langle S \rangle_j$. For translationally invariant systems we get $\langle S \rangle_j = m$ and $J_{ij} = J$. The sum over lattice sites j can then be simplified to a product with the lattice coordination number z .

With this, one arrives from Eq. (2.2) at the well-known mean-field equation for the magnetization at finite temperature T ($\beta = \frac{1}{k_B T}$),

$$m = \tanh(\beta h + z\beta J m), \quad (2.4)$$

which can be reformulated in terms of the Weiss effective field,

$$h_{\text{eff}} = zJ \tanh(\beta h_{\text{eff}}) + h. \quad (2.5)$$

Eq. (2.4) and Eq. (2.5) have the form of a self-consistency condition for the magnetization and the Weiss field, respectively.

The approximation of neglecting correlated spin fluctuations becomes exact in the limit of an infinite coordination number z . For lower dimensions, z serves as a control parameter for the validity of the mean-field approximation. Yet, to obtain a sensible limit $z \rightarrow \infty$, where physical quantities like the effective magnetic field h_{eff} remain finite, we have to rescale the coupling constant J as

$$J = \frac{J^*}{z}, \quad J^* = \text{const}. \quad (2.6)$$

The basic steps of the Weiss mean-field theory can be directly extended to quantum many-body problems [4] (see Fig. 2.1 for the one-band Hubbard model):

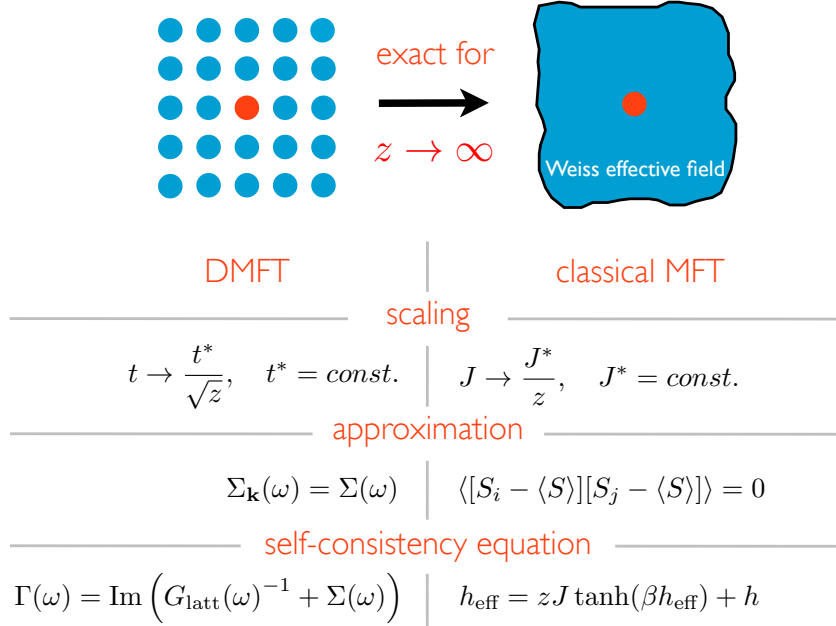


Figure 2.1: Basic steps of DMFT compared to the classical Weiss mean-field theory. In both methods a complex lattice problem is mapped onto an effective single-site problem. The dynamics of the whole lattice is then represented by the interaction of the degrees of freedom at the single site with an external field, the Weiss effective field, which is comprised of all the other degrees of freedom at the other sites. The Weiss field (the static magnetic field h_{eff} for the classical Ising model and the dynamical hybridization function $\Gamma(\omega)$ for the quantum case) is determined by a self-consistency condition. The mapping is based on an approximation (neglecting correlated spin fluctuations in the classical case and a momentum independence in the self-energy in DMFT), that is exact in the limit of infinite lattice coordination $z \rightarrow \infty$. In this limit, physical quantities (like the ferromagnetic coupling J for the Ising model and the hopping amplitude t for the Hubbard model (see Sec. 2.2.1)) have to be rescaled.

A complex quantum lattice problem is mapped onto a single-site quantum impurity problem (Anderson model), that has to fulfill a self-consistency condition (see Sec. 2.3.5). The whole lattice dynamics is then captured by the local single-particle retarded lattice Green's function (see Sec. 2.3.2)

$$G_{\mu\nu}^R(t) = -i\Theta(t)\langle\{\hat{c}_\mu(t), \hat{c}_\nu^\dagger\}\rangle_T \quad (2.7)$$

with the fermionic annihilation (creation) operator $\hat{c}_{\mu,\nu}^{(\dagger)}$, acting locally on one specific lattice site with possible quantum labels μ, ν (e.g. for different spins or several orbitals) and the (real) time evolution in the Heisenberg picture $\hat{c}_\mu(t) = e^{i\hat{H}t}\hat{c}_\mu e^{-i\hat{H}t}$. As we will use the retarded Green's function throughout this thesis we will skip the superscript R from now on.

The basic approximation within DMFT is to freeze out spatial fluctuations by introducing a purely local (site-diagonal) self-energy

$$\Sigma_{ij}(\omega) \xrightarrow{z \rightarrow \infty} \Sigma(\omega)\delta_{ij}, \quad (2.8a)$$

or expressed in the Fourier space, a momentum-independent self-energy

$$\Sigma_{\mathbf{k}}(\omega) \xrightarrow{z \rightarrow \infty} \Sigma(\omega). \quad (2.8b)$$

Yet, in contrast to the classical case, where the magnetization is static, the DMFT approximation fully incorporates local temporal quantum fluctuations. Hence, we achieve a dynamical (frequency dependent) mean-field theory for the quantum case. As for the Ising model, the approximation becomes exact in the limit of infinite lattice coordination also for quantum lattice problems (which was shown by W. Metzner and D. Vollhardt in 1989 [7]). In this limit appropriate scaling of the investigated Hamiltonian leads to a local nature of perturbation theory and therefore to a momentum-independent self-energy. Again the coordination number constitutes a control parameter for the validity of the approach. As z is reasonably large in three dimensions (e.g. $z = 6$ for a cubic lattice and $z = 12$ for a face centered cubic lattice), we can apply the DMFT method in good approximation to three dimensional lattice problems.

2.2 Model Hamiltonians

To study the properties of strongly correlated materials, we need model Hamiltonians that can be solved numerically (with the DMFT method). The most fundamental model for strongly correlated materials is the one-band spin- $\frac{1}{2}$ Hubbard model. For more realistic descriptions, model Hamiltonians can be constructed via the local density approach (LDA).

2.2.1 The Hubbard model

The one-band spin- $\frac{1}{2}$ Hubbard model was introduced by J. Hubbard in its seminal work of 1963 [11] and is a tight-binding description for solids including interactions:

$$\hat{H} = -\mu \sum_{i\sigma} \hat{n}_{i\sigma} + \sum_{\langle ij \rangle \sigma} t_{ij} \hat{c}_{i\sigma}^\dagger \hat{c}_{j\sigma} + U \sum_i \hat{n}_{i\uparrow} \hat{n}_{i\downarrow}, \quad (2.9)$$

where $\hat{n}_i \equiv \sum_{\sigma} \hat{c}_{i\sigma}^\dagger \hat{c}_{i\sigma}$ is the particle number operator of site i . $\hat{c}_{i\sigma}^{(\dagger)}$ denote the corresponding annihilation (creation) operators for the conduction electrons with spin $\sigma = \uparrow, \downarrow$. $\sum_{\langle ij \rangle}$ is a sum over nearest neighbors i and j only.

As common for the tight binding approximation, the solid is modeled by various sites i , representing the constituent atoms (or molecules) of the material, that are arranged in a specific type of lattice. The atoms exhibit orbitals occupied by a certain number of electrons, some of which can contribute to transport by hopping between the orbitals centered around different sites. In the case of the one-band Hubbard model, only one orbital per site with maximally two electrons (one for each spin) contributes to transport.

The first term of the model Hamiltonian gives the local single-particle energy level in terms of the chemical potential μ . The second term yields the kinetic energy of the conduction electrons, which is determined by the hopping amplitude t_{ij} for an electron of spin σ to be annihilated at site j and again created at site i . This transfer amplitude (between nearest-neighbor sites i and j in the case of Eq. (2.9) or between different orbitals in general) can be calculated by considering an overlap integral between Wannier functions, representing the corresponding localized orbitals. To simplify our model, we assume the hopping amplitude to be site-independent in the following, i. e. $t_{ij} = t$. The Fourier transform of the kinetic energy part of Eq. (2.9) results in the band dispersion $\varepsilon_{\mathbf{k}}$ and the momentum distribution operator $\hat{n}_{\mathbf{k}\sigma}$:

$$\sum_{\langle ij \rangle \sigma} t \hat{c}_{i\sigma}^\dagger \hat{c}_{j\sigma} = \sum_{\mathbf{k}\sigma} \varepsilon_{\mathbf{k}} \hat{n}_{\mathbf{k}\sigma}. \quad (2.10)$$

The bandwidth of the one-band Hubbard model is determined by the hopping amplitude t (see Sec. 2.3.3).

The third term of the Hubbard Hamiltonian includes the on-site Coulomb repulsion U between electrons sitting at the same site i . The Coulomb interaction can be approximated as purely local because it is in general heavily screened for strongly correlated materials. Its implication leads to a competition between itinerancy and localization of electrons and can give rise to intriguing many-body phenomena like the “Mott-Hubbard metal-insulator transition” (MIT), which will be discussed in detail in Chapter 5.

2.2.2 Model Hamiltonians from the local density approach (LDA)

A very recent development in the field of DMFT is the realistic modeling of materials, considering the actual electronic and lattice structure - the LDA+DMFT approach. Here the art of modeling is to incorporate material specific details, but to keep the model as simple as possible at the same time in order to allow for its numerical treatment. In that sense, the Hubbard Hamiltonian is the minimal Hamiltonian for a system with a narrow band at the Fermi level, where all other degrees of freedom are projected out [10, Chapter 6]. To describe the complexity of real materials, the Hubbard model typically has to be extended (see Chapter 6).

While the DMFT method is based on model Hamiltonians with empirically determined physical parameters, the density functional theory (DFT) and its local density approach (LDA) are ab initio methods for the calculation of realistic band structures (yet without considering strong correlation effects) [10, Chapter 1]. In the LDA method an ab-initio basis of localized Wannier functions is constructed, that carries the relevant details about the structure and chemistry of a given material (like the number and type of orbitals contributing to transport) [10, Chapter 6]. These functions are then used to determine the hopping integrals (or analogously the dispersion relation) and the local electronic energy levels of the orbitals. The interaction parameters can, in principle, also be calculated from the LDA Wannier functions. However, it is still a major challenge to obtain the screened Coulomb integrals ab initio [10, Chapter 6]. Note that model Hamiltonians based on LDA contain an additional term (the “double counting correction”) that cancels the electron-electron interaction contained in the hopping term. Normally this correction is absorbed in the local electronic energy levels of the orbitals.

In Sec. 6 we give a more detailed introduction in the realistic modeling of strongly correlated materials and investigate a Hamiltonian with material specific details (two degenerate orbitals).

2.3 Derivation of the DMFT equations

In this section we want to present the basic ideas of DMFT in more detail and derive the DMFT equations which will be later solved with the NRG method. For simplicity, we concentrate on the one-band Hubbard model. Yet, the method can be adapted to more complex models in a straightforward manner (see Sec. 6.2).

2.3.1 Local nature of the self-energy in infinite dimensions

We now have a closer look how the simplification of a momentum-independent self-energy arises for the limit $z \rightarrow \infty$. As for the classical case we have to ensure a non-trivial limit for physical

quantities (like the internal energy per site), which leads to a scaling condition for the Hubbard Hamiltonian. While the interaction term, as well as the term containing the chemical potential, are purely local and therefore not affected by the number of nearest neighbors z , the kinetic energy per site diverges with growing coordination number and has to be properly rescaled to retain the competition between the kinetic and the interaction energy. This can be easily understood from the corresponding non-interacting density of states (DOS)

$$\rho_0(\varepsilon) = \frac{1}{N_B} \sum_{\mathbf{k}} \delta(\varepsilon - \varepsilon_{\mathbf{k}}) \quad (2.11)$$

with $\int_{-\infty}^{\infty} \rho_0(\varepsilon) d\varepsilon = 1$. Following the argumentation of W. Metzner and D. Vollhardt [7], we consider a simple d -dimensional hypercubic lattice with dispersion relation

$$\varepsilon_{\mathbf{k}} = -2t \sum_{i=1}^d \cos \mathbf{k}_i \quad (2.12)$$

and coordination number $z = 2d$. The DOS can be interpreted as the probability density to find an one-particle excitation of energy $\varepsilon = \varepsilon_{\mathbf{k}}$ for randomly chosen \mathbf{k}_i . In the limit $d \rightarrow \infty$, the dispersion relation is then a sum over essentially independent random numbers $-2t \cos \mathbf{k}_i$ with the only constraint that $\sum_{i=1}^d \cos \mathbf{k}_i = -\frac{\varepsilon}{2t}$. As a consequence, one can apply the central limit theorem, leading to a gaussian DOS [10, Chapter 3],

$$\rho_0^H(\varepsilon) \xrightarrow{d \rightarrow \infty} \frac{1}{2t\sqrt{\pi d}} \exp \left[- \left(\frac{\varepsilon}{2t\sqrt{d}} \right)^2 \right], \quad (2.13)$$

that retains a finite width only if the hopping amplitude scales like

$$t = \frac{t^*}{\sqrt{z}} = \frac{t^*}{\sqrt{2d}}, \quad t^* = \text{const.} \quad (2.14)$$

The rescaled Hamiltonian

$$\hat{H} = -\mu \sum_{i\sigma} \hat{n}_{i\sigma} + \sum_{\langle ij \rangle \sigma} \frac{t^*}{\sqrt{z}} \hat{c}_{i\sigma}^\dagger \hat{c}_{j\sigma} + U \sum_i \hat{n}_{i\uparrow} \hat{n}_{i\downarrow} \quad (2.15)$$

has now a well-defined limit $z \rightarrow \infty$ and the kinetic energy per site remains finite by construction. The kinetic energy can be written in terms of the full interacting fermion propagator G_{ij} :

$$E_{\text{kin}} = \sum_{\langle ij \rangle} \frac{t^*}{\sqrt{z}} \langle \hat{c}_i^\dagger \hat{c}_j \rangle = \lim_{t \rightarrow 0^+} \sum_{\langle ij \rangle} \frac{t^*}{\sqrt{z}} \int_{-\infty}^{\infty} \frac{d\omega}{2\pi i} G_{ij}(\omega) e^{i\omega t}. \quad (2.16)$$

(Note that we have skipped the spin index for convenience, as it will not affect the following derivations. It can be simply reintroduced afterwards.) As the kinetic energy per site is of order 1 for $z \rightarrow \infty$, we can derive from the above expression that G_{ij} has to scale like

$$G_{ij} \sim \mathcal{O} \left(\frac{1}{\sqrt{z}} \right) \quad \text{for } |i - j| = 1, \quad (2.17a)$$

$$G_{ii} \sim \mathcal{O}(1), \quad (2.17b)$$

since the sum over all nearest-neighbors yields an order z while the scaling of the hopping amplitude goes like $1/\sqrt{z}$ [10, Chapter 5].

This scaling behavior leads to strong simplifications in perturbation theory in $z \rightarrow \infty$, including a momentum-independent self-energy [4]. This may be best demonstrated diagrammatically using the skeleton expansion for the self-energy of the Hubbard model in real space (see Fig. 2.2), which solely consists of full interacting propagator lines G_{ij} (double lines) and local interaction vertices (dashed lines).

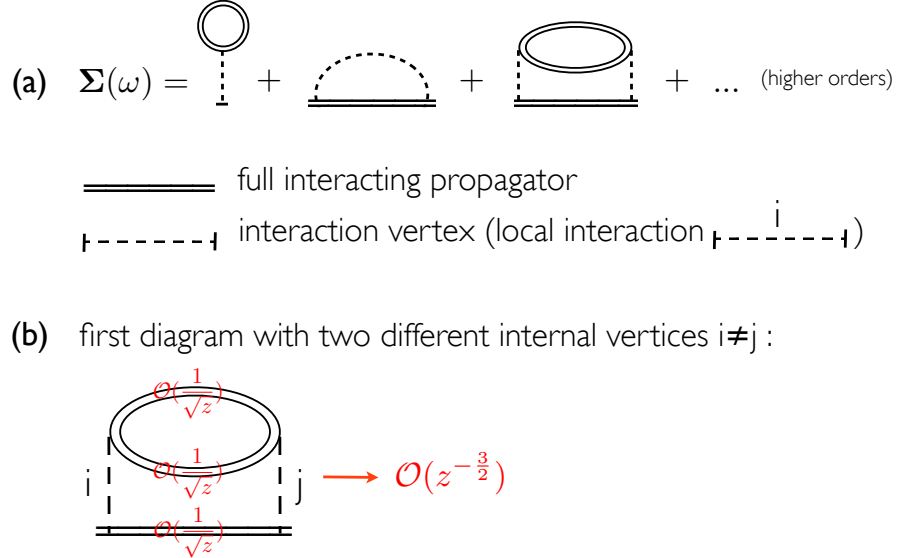


Figure 2.2: Panel (a) shows the skeleton expansion for the self-energy of the Hubbard model as in [10, Chapter 5] with arrows and labels omitted. The full interacting propagator lines G_{ij} scale like $1/\sqrt{z}$ for $i \neq j$. For the second order diagram (depicted in panel (b)) we see that it vanishes as $1/\sqrt{z}$. The three independent propagator lines give a factor of $z^{-\frac{3}{2}}$. The sum over nearest neighbors yields another factor of order z . So in the limit $z \rightarrow \infty$ this diagram scales like $1/\sqrt{z}$ and therefore does not contribute to the self-energy.

It can be easily shown that two different internal vertices $i \neq j$ are at least connected by three independent propagator lines, each of which scale like $1/\sqrt{z}$ (see the second order diagram in Fig. 2.2 (b) as example). So a factor of at least $z^{-\frac{3}{2}}$ is obtained for each diagram (of order ≥ 2 and with different internal vertices $i \neq j$). The sum over nearest neighbors yields another factor of order z . Thereby, any non-local contribution of the skeleton perturbation expansion vanishes at least as $1/\sqrt{z}$ and all diagrams fully collapse to a single site in the limit of infinite coordination number $z \rightarrow \infty$ [4]. Thus the self-energy becomes a purely local quantity in real space,

$$\Sigma_{ij}(\omega) \xrightarrow{z \rightarrow \infty} \Sigma(\omega) \delta_{ij}, \quad (2.18a)$$

and its Fourier transform is momentum independent,

$$\Sigma_{\mathbf{k}}(\omega) \xrightarrow{z \rightarrow \infty} \Sigma(\omega). \quad (2.18b)$$

Yet, the self-energy is still frequency dependent. So the DMFT approximation Eq. (2.18b) only freezes out spatial fluctuations but completely accounts for temporal quantum fluctuations, which are at the bottom of the interesting features of strongly correlated materials [4].

Although this derivation of the DMFT approximation is based on a perturbative expansion of the self-energy with a finite radius of convergence [12], the central statement of a momentum-independent self-energy and all subsequent DMFT equations are proven to be non-perturbative (see for example the cavity method in [4]). The fact that the DMFT approximation becomes exact in the limit of infinite coordination ensures that physical constraints, such as causality of the self-energy, are retained within the DMFT approach [1].

In complete analogy, the DMFT approximation can be adapted to more complex models than the one-band Hubbard Hamiltonian discussed above.

2.3.2 On-site lattice Green's function

In the previous section, it was shown that all the diagrams in the skeleton expansion of the self-energy collapse to a single site. So, the self-energy reduces to a functional that only depends on the local Green's function. As a consequence, the two central quantities in DMFT are the (retarded) on-site lattice Green's function and the local self-energy, which are both dynamical and able to capture genuine correlation effects [10, Chapter 1].

For translationally invariant lattice Hamiltonians (such as the one-band Hubbard Hamiltonian) and skipped spin index, one can write the retarded lattice Green's function in momentum space as

$$G_{\text{latt},\mathbf{k}}(\omega) \equiv \langle \hat{c}_{\mathbf{k}} | \hat{c}_{\mathbf{k}}^\dagger \rangle_\omega = \frac{1}{\omega + \mu - \varepsilon_{\mathbf{k}} - \Sigma_{\text{latt},\mathbf{k}}(\omega)} \quad (2.19)$$

with all the interaction effects considered by the self-energy $\Sigma_{\text{latt},\mathbf{k}}(\omega)$. Note that vectors, as well as matrices, are printed in bold. Using the DMFT approximation, we arrive at the simplified form

$$G_{\text{latt},\mathbf{k}} = \frac{1}{\omega + \mu - \varepsilon_{\mathbf{k}} - \Sigma_{\text{latt}}(\omega)} = G_{\text{latt},\mathbf{k}}^0(\omega - \Sigma_{\text{latt}}(\omega)) \quad (2.20)$$

with the non-interacting expression for the retarded lattice Green's function

$$G_{\text{latt},\mathbf{k}}^0(\omega) = \frac{1}{\omega + \mu - \varepsilon_{\mathbf{k}}}. \quad (2.21)$$

A general derivation of the above equations, based on an equation of motion ansatz (see Appendix A), is given in Appendix B. $\omega \equiv \omega^+ = \omega + i\delta$ with the positive infinitesimal δ accounts for causality of the retarded Green's function. The local or on-site lattice Green's function (which is chosen to be at site $\mathbf{r} = 0$, for convenience) can then be calculated as the Fourier transform

$$G_{\text{latt}}(\omega) = \frac{1}{N_B} \sum_{\mathbf{k}} G_{\text{latt},\mathbf{k}}(\omega) e^{i\mathbf{k}(\mathbf{r}=0)} \quad (2.22a)$$

$$= \frac{1}{N_B} \sum_{\mathbf{k}} \frac{1}{\omega + \mu - \varepsilon_{\mathbf{k}} - \Sigma_{\text{latt}}(\omega)} \quad (2.22b)$$

$$= \int_{-\infty}^{\infty} d\varepsilon \frac{\rho_0(\varepsilon)}{\omega + \mu - \varepsilon - \Sigma_{\text{latt}}(\omega)}, \quad (2.22c)$$

where N_B denotes the number of \mathbf{k} -points of the Brillouin zone and $\rho_0(\varepsilon)$ is the non-interacting density of states (DOS) of the specific lattice (see Sec. 2.3.3 for details). Note that although the self-energy is purely local within DMFT, the Hubbard model is not reduced to a purely local model as hopping between different lattice sites still enters via the momentum-dependent

dispersion relation $\varepsilon_{\mathbf{k}}$.

As we mainly want to investigate transport properties, we are interested in the local density of states (spectral function)

$$A(\omega) \equiv -\frac{1}{\pi} \text{Im} G_{\text{latt}}(\omega). \quad (2.23)$$

It obeys the sum rule

$$\int_{-\infty}^{\infty} d\omega A(\omega) = 1, \quad (2.24)$$

which is especially important for the DMFT approach, and can generally be expressed in Lehman representation as a sum over δ -functions. From the Fourier transform $G_{\mu\mu}(\omega)$ of the expression in Eq. (2.7), we obtain

$$A_{\mu}(\omega) = \sum_{ab} \frac{e^{-\beta E_a} + e^{-\beta E_b}}{Z} |\langle a | \hat{c}_{\mu} | b \rangle|^2 \delta(\omega - (E_b - E_a)) \equiv A_{\mu 1}(\omega) + A_{\mu 2}(\omega) \quad (2.25)$$

with the partition function Z , eigenvalues E_a and corresponding many-body eigenstates $|a\rangle$ of the full Hamiltonian. The index μ can denote any degrees of freedom, such as spin σ and orbital m , depending on the system under consideration. The local density of states can be used to calculate the average occupation number of a specific impurity level.

$$\langle \hat{n}_{\mu} \rangle \equiv \langle \hat{d}_{\mu}^{\dagger} \hat{d}_{\mu} \rangle = \int_{-\infty}^{\infty} d\omega A_{\mu}(\omega) n_F(\omega, T) \quad (2.26a)$$

with the Fermi-Dirac distribution function $n_F(\omega, T)$, or equivalently,

$$\langle \hat{n}_{\mu} \rangle = \int_{-\infty}^{\infty} d\omega A_{\mu 2}(\omega). \quad (2.26b)$$

For the SIAM, we have $\mu \equiv \sigma$.

In essence, the goal of the DMFT procedure is to obtain the shape of the spectral function to high accuracy in order to deduce transport properties.

2.3.3 Non-interacting lattice density of states

As can be observed in Eq. (2.22c), the specific lattice type only enters via the non-interacting density of states, or equivalently over the dispersion relation in the case of Eq. (2.22b). Nevertheless, the material specific configuration of the constituent atoms is also reflected in physical parameters, such as the Coulomb interaction strength and the number of orbitals considered in the model Hamiltonian.

For model calculations, it is common to use the infinite-dimensional limit of the non-interacting DOS as an approximation to finite-dimensional lattices [10, Chapter 5]. A rather artificial, but important lattice type, that is often used for model calculations within DMFT, is the infinite Cayley tree, which is also called Bethe lattice. The corresponding lattice DOS is semi-elliptic for infinite coordination $z \rightarrow \infty$,

$$\rho_0^B(\varepsilon) = \frac{2}{\pi D} \sqrt{1 - \left(\frac{\varepsilon}{D}\right)^2}, \quad \varepsilon \in [-D, D], \quad (2.27)$$

with half bandwidth $D = 2t^*$ and rescaled nearest-neighbor hopping $t = t^*/\sqrt{z}$ [4] (see Appendix D). Another example of an infinite DOS, the gaussian hypercubic lattice DOS, has already been introduced in Sec. 2.3.1. In analogy to the Bethe lattice for infinite coordination $z \rightarrow \infty$, an effective half bandwidth $D = 2t^*$ of twice the standard deviation of the gaussian DOS is introduced for the hypercubic case:

$$\rho_0^H(\varepsilon) = \frac{1}{\sqrt{2\pi(D/2)^2}} \exp\left[-\frac{1}{2}\left(\frac{\varepsilon}{D/2}\right)^2\right], \quad \varepsilon \in [-\infty, \infty]. \quad (2.28)$$

As can be seen in Fig. 2.3 (c) the DMFT results (here the spectral function for the symmetric one-band Hubbard model with $U/D = 2$, $\mu/D = 1$ and $T/D \approx 0$) are qualitatively equal for either lattice type.

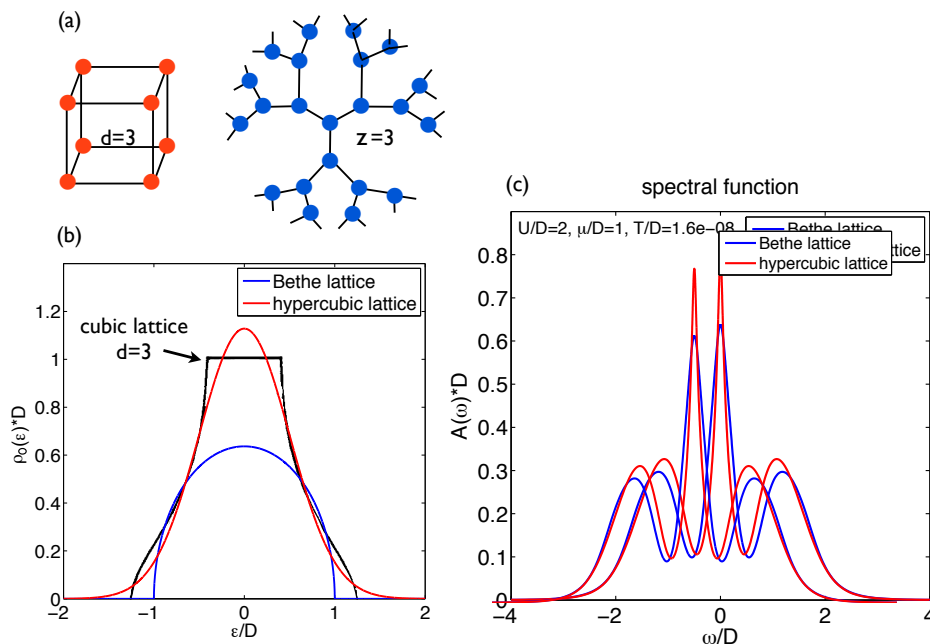


Figure 2.3: Panel (a) contains an illustration for the cubic lattice in three dimensions (red) and the Bethe lattice with coordination $z = 3$ (blue). In panel (b) the Bethe and hypercubic lattice DOS are plotted for infinite coordination $z \rightarrow \infty$. Additionally the cubic lattice DOS for three dimensions is sketched in black (curve adapted from [13]) to show that the red curve is a good approximation for the finite dimensional case $d = 3$. In panel (c) we plotted the corresponding spectral functions for the symmetric one-band Hubbard model with $U/D = 2$, $\mu/D = 1$ and $T/D \approx 0$, which are qualitatively equal for either lattice type.

Besides, there are also other DOS considered in the literature, like the DOS for the infinite version of the three-dimensional diamond lattice or the Lorentzian DOS involving long-range hopping (see [4] for details). On a model level, the Bethe DOS for infinite coordination $z \rightarrow \infty$ is often favored, as the expression for the local lattice Green's function Eq. (2.22c) can then be obtained analytically and leads to a quite simple form of the self-consistency condition (see Sec. 2.3.5). The local lattice Green's function is formally the Hilbert transform of the non-interacting density of states

$$G_{\text{latt}}(\xi) = \int_{-\infty}^{\infty} d\varepsilon \frac{\rho_0(\varepsilon)}{\xi - \varepsilon} \quad (2.29)$$

with $\xi = \omega + \mu - \Sigma(\omega)$ and $\text{Im } \xi = -\text{Im } \Sigma(\omega) > 0$ (as we consider the retarded Green's function). For the semi-elliptic DOS we obtain

$$G_{\text{latt}}(\omega) = \frac{2}{D^2} \left(\xi - \sqrt{\xi^2 - D^2} \right), \quad (2.30)$$

using a continued fraction expansion for the local retarded Green's function (see Appendix D for details).

For LDA Hamiltonians the local lattice Green's function is directly computed from the sum over the Brillouin zone in Eq. (2.22b), that explicitly contains the LDA band structure.

2.3.4 Mapping onto an effective quantum impurity model

In this section, we discuss the non-trivial part of how to compute the self-energy in the expression of the local lattice Green's function, which represents the central quantity in the DMFT approach. The big simplification was given in 1992 by A. Georges and G. Kotliar [8]: the lattice model can be mapped onto a quantum (Anderson) impurity model with effective parameters, that exhibits the same local interaction term as the original model. Impurity Anderson models and the associated Kondo physics of strongly correlated electrons have been studied intensively since the 1980's and are often well-understood due to a variety of efficient numerical codes [10, Chapter 1].

Since interaction effects only enter locally through the momentum-independent self-energy in DMFT, the self-energy of a single-site quantum impurity Hamiltonian with equal local interaction resembles that of the lattice model:

$$\Sigma_{\text{latt}}(\omega) = \Sigma_{\text{imp}}(\omega) \equiv \Sigma(\omega). \quad (2.31)$$

As a consequence, the dynamics of the lattice model, which is encoded in its local lattice Green's function, can be determined via the Green's function of the impurity model - a single site coupled to an effective bath - analogously to the classical mean-field theory, where the local magnetization is described as a spin on a single site, that is coupled to an effective magnetic field (the Weiss mean-field) [1]. So the mapping of the lattice model onto the effective quantum impurity can be written as

$$G_{\text{latt}}(\omega) \stackrel{!}{=} G_{\text{imp}}(\omega). \quad (2.32)$$

For the single-band Hubbard Hamiltonian, the effective quantum impurity model is the single impurity Anderson model (SIAM):

$$\hat{H}_{\text{SIAM}} = \hat{H}_{\text{imp}} + \hat{H}_{\text{bath}} + \hat{H}_{\text{cpl}}, \quad (2.33)$$

$$\hat{H}_{\text{imp}} = \sum_{\sigma} \varepsilon_d \hat{d}_{\sigma}^{\dagger} \hat{d}_{\sigma} + U \hat{d}_{\uparrow}^{\dagger} \hat{d}_{\uparrow} \hat{d}_{\downarrow}^{\dagger} \hat{d}_{\downarrow}, \quad (2.33a)$$

$$\hat{H}_{\text{bath}} = \sum_{k\sigma} \varepsilon_k \hat{c}_{k\sigma}^{\dagger} \hat{c}_{k\sigma}, \quad (2.33b)$$

$$\hat{H}_{\text{cpl}} = \sum_{k\sigma} V_k (\hat{d}_{\sigma}^{\dagger} \hat{c}_{k\sigma} + \text{h.c.}). \quad (2.33c)$$

For more complex lattice problems, the SIAM will be generalized to multi-band (or multi-orbital) Anderson models (see Sec. 6.2).

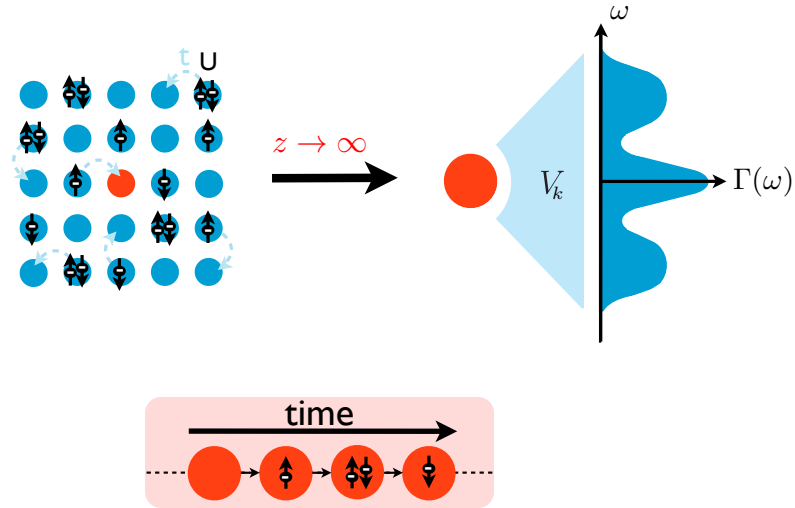


Figure 2.4: In the DMFT approach a quantum lattice problem (here the Hubbard model) is mapped self-consistently onto a single-site effective problem (the single impurity Anderson model). Left, we illustrate the Hubbard model where electrons can hop between different lattice sites with a hopping amplitude t and feel a Coulomb repulsion of strength U , when they meet on one site. On the right, we show a sketch of the SIAM (adapted from [14]), where a single impurity is coupled via the amplitude V_k to an effective bath. The effect of the environment on the impurity site is described by the Weiss field - the hybridization function $\Gamma(\omega) = \pi \sum_k V_k^2 \delta(\omega - \varepsilon_k)$. In essence, the impurity represents a given lattice site (red), the hybridization describes the influence of the remaining lattice (blue). Thus spatial correlations in the bath are frozen out while local quantum fluctuations (indicated in the red box) are completely retained by the mapping onto the local impurity model.

A given site of the lattice (at $\mathbf{r} = 0$) is represented by the impurity. $\hat{d}_\sigma^{(\dagger)}$ denotes the annihilation (creation) operator for an electron of spin $\sigma = \uparrow, \downarrow$ on the impurity. ε_d is the local energy level of the impurity site and has to be equal to the local single-particle level $-\mu$ of the lattice. As in the lattice case, the local site has four different possible quantum states. It can be unoccupied ($|0\rangle$), singly occupied with an electron of spin up or down ($|\sigma\rangle$), or doubly occupied by electrons of spin up and down ($|\uparrow\downarrow\rangle$), respectively. In the last case, the electrons feel a Coulomb repulsion of strength U . The interaction term in the SIAM is equal to the local interaction of the Hubbard model. The rest of the lattice is described by an *effective* bath of non-interacting fermions (\hat{H}_{bath}), that hybridizes with the impurity via the hopping amplitude given by V_k . $\hat{c}_{k\sigma}^{(\dagger)}$ are the corresponding annihilation (creation) operators in the bath. Thus, the local impurity model allows for charge and spin fluctuations. As the impurity is embedded in an effective environment, it may undergo transitions between different quantum phases. The effect of the external bath onto the impurity is fully contained in the hybridization function,

$$\Delta(\omega) = \sum_k \frac{V_k^2}{\omega - \varepsilon_k}. \quad (2.34)$$

With $\omega \equiv \omega^+$, $\Delta(\omega)$ is analytic in the upper complex plane. Hence, it is sufficient to concentrate

on the imaginary part,

$$\Gamma(\omega) \equiv -\text{Im } \Delta(\omega) = \pi \sum_k V_k^2 \delta(\omega - \varepsilon_k), \quad (2.35)$$

which plays the role of the effective Weiss field in DMFT. It is frequency dependent and hence dynamical. The hybridization, however, is not known a priori, but has to be determined in a self-consistent manner. The effective impurity model then reproduces the actual mean-field solution of the original many-body problem. An illustration of the self-consistent mapping onto an effective quantum impurity model is shown in Fig. 2.4.

The local interacting Green's function of the effective impurity model is completely given in terms of the hybridization function $\Delta(\omega)$ and the self-energy $\Sigma(\omega)$:

$$G_{\text{imp}}(\omega) \equiv \langle \hat{d} \| \hat{d}^\dagger \rangle_\omega = \frac{1}{\omega - \varepsilon_d - \Delta(\omega) - \Sigma(\omega)}, \quad \varepsilon_d = -\mu. \quad (2.36)$$

This can be derived from the equation of motion (see Appendix C for a detailed calculation),

$$\omega \langle \hat{d} \| \hat{d}^\dagger \rangle_\omega = \langle \{ \hat{d}, \hat{d}^\dagger \} \rangle_T - \langle [\hat{H}, \hat{d}] \| \hat{d}^\dagger \rangle_\omega. \quad (2.37)$$

In the following, we want to derive the DMFT self-consistency condition for the calculation of the Weiss effective field $\Gamma(\omega)$ and present a possible solution process to obtain finally the local lattice Green's function and the corresponding spectral function.

2.3.5 The self-consistency procedure

The mapping of an original lattice onto an effective impurity model is performed by equating the local lattice Green's function with the impurity Green's function in Eq. (2.32), $G_{\text{latt}}(\omega) \stackrel{!}{=} G_{\text{imp}}(\omega)$, which imposes a self-consistent condition for the Weiss effective field $\Gamma(\omega)$. Inserting the impurity Green's function Eq. (2.36) into Eq. (2.32) yields

$$G_{\text{latt}}(\omega)^{-1} + \Sigma(\omega) = \omega - \varepsilon_d - \Delta(\omega) = G_{\text{imp}}^0(\omega)^{-1} \quad (2.38)$$

with $\varepsilon_d = -\mu$, and a simple relation for the imaginary part,

$$\Gamma(\omega) = -\text{Im } \Delta(\omega) = \text{Im}(G_{\text{latt}}(\omega)^{-1} + \Sigma(\omega)). \quad (2.39)$$

This is the DMFT self-consistency condition, relating for each frequency the Weiss effective field and the local lattice Green's function. Thus, it leads to a closed set of DMFT equations, that can be solved iteratively and which finally fully determines the hybridization function $\Gamma(\omega)$, the local self-energy $\Sigma(\omega)$ and accordingly the local Green's function. The DMFT equations are summarized in the iterative DMFT procedure in Fig. 2.5. In principle, the self-consistency equations can be formulated differently, depending on how the impurity model is solved. Since quantum impurity models have been investigated intensively over the last decades, a variety of (partly numerically extensive) techniques are available. Quantum Monte Carlo (QMC) methods are widely used and a lot of different algorithms (like the Hirsch-Fye QMC or the continuous-time (CT) QMC) have been successfully developed. Possible limitations are very low temperatures and the so called "sign problem". Furthermore, QMC methods compute the physical quantities in dependence of imaginary Matsubara frequencies. Therefore (Pade) continuation to the real frequency axis has to be performed, which may become difficult for complex models (see Chapter 6). Other quantum impurity solvers include the Numerical Renormalization Group

(NRG), exact diagonalization, the density matrix renormalization group (DMRG) or analytical yet approximate schemes like the iterated perturbation theory or the noncrossing approximation (for a list with references see [4] and [12]).

We will use the Numerical Renormalization Group (NRG) to solve the quantum impurity model, a method that is well-established in the realm of quantum impurity problems. It offers a clear advantage in that it calculates data directly on the real frequency axis. Therefore the self-consistency procedure generates the (frequency-dependent) hybridization, which is a natural input for the NRG method.

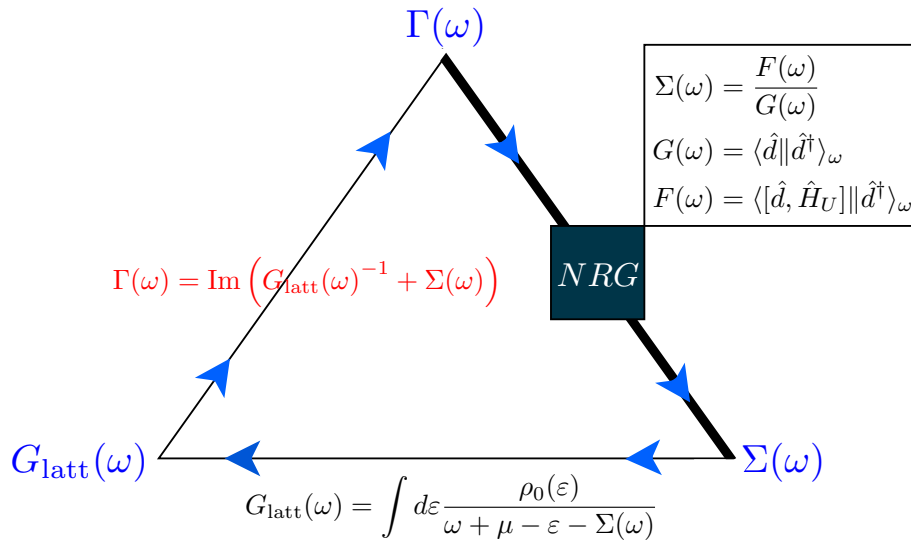


Figure 2.5: DMFT self-consistency procedure with the NRG method as “impurity solver”. Starting from an arbitrary hybridization function $\Gamma(\omega)$, we obtain the self-energy from the NRG approach, solving the effective quantum impurity problem for the first DMFT iteration. The self-energy is then inserted into the expression for the lattice Green’s function. The self-consistency condition closes the DMFT loop, yielding a new hybridization function. The iterative procedure is repeated until convergence is reached.

At the start of the calculation, we know neither hybridization nor the local Green’s function. One therefore starts the self-consistency procedure with an arbitrary input hybridization $\Gamma(\omega)$. This completely defines the quantum impurity model that has to be solved in the first iteration with the NRG method. The NRG “impurity solver”, depicted as a black box in Fig. 2.5, returns the self-energy of the SIAM, which is equal to the lattice self-energy and thus can be inserted into the integral expression Eq. (2.22c) for the lattice Green’s function. The calculation of the self-energy is not performed via the common Dyson equation $\Sigma(\omega) = G_{\text{imp}}^0(\omega)^{-1} - G_{\text{imp}}(\omega)^{-1}$, but given as the ratio of a two-particle and a one-particle Green’s function (see the box in Fig. 2.5). The details of this NRG specific approach are presented in Sec. 4.1. With the self-consistency condition Eq. (2.39), we arrive at a new hybridization function, that serves as input for the next iteration. After performing several DMFT iterations, the iterative procedure converges to

a stable and usually unique solution, independently of the initial input hybridization. Only in some special cases (e.g. close to a Mott transition) different input regimes lead to more than one stable solution [1] (see Sec. 5.1). From the converged version of the lattice (or impurity) Green's function, finally, we also have the local spectral function of the strongly correlated many-body system, and hence can investigate its dynamics.

For model calculations, it is convenient to use the semi-elliptic Bethe lattice DOS, since the DMFT self-consistency equations reduce to a compact form, i.e. without numerical integration. With the analytic expression for the lattice Green's function Eq. (2.30), $G_{\text{latt}}(\omega) = 2/D^2 (\xi - \sqrt{\xi^2 - D^2})$, and $\xi = \omega + \mu - \Sigma(\omega)$ (see Sec. 2.3.3), we can simply derive

$$\omega - \varepsilon_d - \Delta(\omega) = \omega + \mu - \left(\frac{D}{2}\right)^2 G_{\text{latt}}, \quad (2.40)$$

by inserting Eq. (2.30) into Eq. (2.38). From this equation we explicitly see that $\varepsilon_d = -\mu$ in the impurity model. Further, it leads directly to the compact expressions

$$\Delta(\omega) = \left(\frac{D}{2}\right)^2 G_{\text{latt}}(\omega) \quad \text{and} \quad \frac{\Gamma(\omega)}{\pi} \stackrel{\text{Eq. (2.23)}}{=} \left(\frac{D}{2}\right)^2 A(\omega). \quad (2.41)$$

The thick line in the illustration of the DMFT loop in Fig. 2.5 depicts that the non-trivial and numerically most time-consuming part of the DMFT self-consistency procedure is the computation of the self-energy via the impurity model. The accuracy of the ‘‘impurity solver’’ completely determines the overall success of the DMFT procedure. Especially for more evolved models with additional degrees of freedom (like multi-band Hubbard models) high numerical efficiency and flexibility of the algorithm is required. In this thesis, we introduce the powerful NRG program of our group (developed by A. Weichselbaum) in the framework of DMFT. It is a highly refined and accurate numerical code that is able to deal efficiently with complex systems in the context of symmetries, as arbitrary abelian and non-abelian symmetries can be exploited. In the next chapter we will first give an introduction to the general concept of the Numerical Renormalization Group and then present the outstanding features of our NRG code that make it, also in the DMFT framework, highly competitive. In Chapter 4, we will discuss problems that can arise when NRG is used within DMFT. Special attention is directed at the issue of a frequency-dependent hybridization function within NRG.

Chapter 3

Numerical Renormalization Group (NRG)

The Numerical Renormalization Group (NRG) was developed in the early 1970's by K. G. Wilson to solve the Kondo model in a fully nonperturbative way. In this model, a single magnetic impurity interacts with the conduction band electrons of a nonmagnetic metal describing dilute magnetic alloys. NRG has subsequently evolved to become the most reliable numerical method available for treating quantum impurity models.

A quantum impurity model consists in general of a discrete quantum system with a small number of degrees of freedom that is coupled to a macroscopic bath of non-interacting fermions (or bosons). Each system on its own can in principle be solved exactly, the coupling of both, however, leads to strongly correlated quantum many-body phenomena.

As we do not consider any bosonic problems in this work, we concentrate on the Hamiltonian for a fermionic quantum impurity system, which can be written in terms of three different parts:

$$\hat{H} = \hat{H}_{\text{imp}} + \hat{H}_{\text{bath}} + \hat{H}_{\text{cpl}}. \quad (3.1)$$

The impurity Hamiltonian \hat{H}_{imp} may contain arbitrary interactions, like Coulomb repulsion or Hund's coupling terms. Since by assumption the "impurity" has just a small number of degrees of freedom, \hat{H}_{imp} can be diagonalized exactly.

The non-interacting bath term \hat{H}_{bath} usually describes a (quasi)continuous excitation spectrum covering a broad range of energies:

$$\hat{H}_{\text{bath}} = \sum_{\mu=1}^{n_c} \sum_k \varepsilon_{k\mu} \hat{c}_{k\mu}^\dagger \hat{c}_{k\mu} \quad (3.2)$$

with $\mu = 1, \dots, n_c$ labeling different kinds of electrons like electrons from different baths (e.g. $\mu = 1, 2$ for two baths) or just electrons with different spin ($\mu = \uparrow, \downarrow$). $\hat{c}_{k\mu}^\dagger$ and $\hat{c}_{k\mu}$ create and annihilate a bath electron of type μ and energy $\varepsilon_{k\mu}$, respectively. The energy support of the bath is defined by the bandwidth of the specific problem. For a standard NRG calculation one normally chooses the interval $[-D, D]$ with $D = 1$ and the Fermi energy situated in the middle of the band at $\varepsilon_F = 0$. Within DMFT, however, the band structure changes after every iteration of the self-consistency procedure. Hence it is more convenient to define all energies in units of $D=1$ using the bandwidth of the non-interacting density of states (see Sec. 2.3.3), which remains

fixed during the entire calculation. Nevertheless, for simplicity, we will adhere to the standard NRG convention with a half bandwidth of $D = 1$ for the subsequent derivations.

The third part of the Hamiltonian \hat{H}_{cpl} couples the two subsystems.

Such an interacting quantum-mechanical system can display a variety of interesting physics depending on the system parameters and the energy scale under consideration. For the Kondo Hamiltonian there is a crossover from a high temperature regime with free impurity spin to a strong coupling regime with completely screened spin below the Kondo temperature. As a renormalization group approach, the NRG method allows to solve all relevant energy scales by performing successive diagonalization from high to low energy scales (see Sec. 3.1.4). The special about the Numerical Renormalization Group is that this can be done completely nonperturbatively in all system parameters. Thus the NRG method is highly suitable as an impurity solver within DMFT, in which the coupling of the impurity to the bath can have arbitrary strength and structure, since it is determined self-consistently by mapping a lattice model of strongly correlated electrons onto the quantum impurity model.

Since K.G. Wilson's first application of the NRG method to the Kondo problem in 1975 [15], it was continuously improved with a wide range of applications, including the description of quantum dots and also the DMFT (see e.g. R. Bulla, A.C. Hewson and Th. Pruschke 1998 [16], R. Bulla 1999 [17], R. Zitko and Th. Pruschke 2009 [18] for the one-band Hubbard model and T. Pruschke and R. Bulla 2005 [19], R. Peters and T. Pruschke 2010 [20], R. Peters and N. Kawakami 2011 [21] for the two-band Hubbard model).

In the first part of this chapter we give an overview over the basic NRG technique following the paper of H.R. Krishna-murthy, J.W. Wilkins and K.G. Wilson [22] and the review of R. Bulla, T.A. Costi and T. Pruschke [23]. The second part concentrates on more recent developments in the field of NRG based on a matrix product state (MPS) formulation as used in this work (see A. Weichselbaum and J. von Delft 2007 [5], A. Weichselbaum 2011 [24] and 2012 [25] and the dissertation of W. Mnder [14] for an overview).

3.1 Basic method

The starting point of Wilson's NRG approach is to coarse-grain the continuous bath spectral function in energy space. This leads to a model with a discrete set of states that can be mapped onto a semi-infinite tight-binding chain with exponentially decaying couplings, called Wilson chain. The Wilson chain Hamiltonian is solved numerically by iterative diagonalization. (See Fig. 3.1 and Fig. 3.2 for a sketch of the NRG steps.)

It is absolutely crucial to choose a logarithmical discretization scheme to rewrite the Hamiltonian, since this yields an exponentially enhanced low-energy resolution, as compared to a linear discretization, and allows to resolve even the lowest relevant energy scale of the system.

3.1.1 Single impurity Anderson Hamiltonian (SIAM)

For simplicity we restrict our discussion of the NRG method to the single impurity Anderson Hamiltonian (SIAM) in Eq. (2.33). A pictorial representation of the model is given in panel (a) of Fig. 3.1. The effective bath of non-interacting fermions is described by the annihilation (creation) operators $\hat{c}_{k\sigma}^{(\dagger)}$, which fulfill the standard fermionic anticommutation relation $\{\hat{c}_{k\sigma}, \hat{c}_{k'\sigma'}^\dagger\} = \delta_{kk'}\delta_{\sigma\sigma'}$. The imaginary part of the hybridization function, $\Gamma(\omega) = \pi \sum_k V_k^2 \delta(\omega - \varepsilon_k)$, completely

encodes the influence of the bath onto the impurity. So any reformulation of the Hamiltonian, which leaves the hybridization $\Gamma(\omega)$ unchanged, leads to the same physics with respect to the impurity of the SIAM.

As demonstrated for a constant hybridization in [22], a possible one-dimensional energy representation of the SIAM Hamiltonian Eq. (2.33) is achieved by replacing the discrete bath operators $\hat{c}_{k\sigma}^{(\dagger)}$ by the continuum annihilation (and creation) bath operators $\hat{a}_{\varepsilon\sigma}^{(\dagger)}$ via the transformation

$$\hat{c}_{k\sigma}^{(\dagger)} \rightarrow \frac{\hat{a}_{\varepsilon\sigma}^{(\dagger)}}{\sqrt{\rho(\varepsilon)}}. \quad (3.3)$$

$\rho(\varepsilon)$ denotes the non-interacting density of states for the continuous reformulation

$$\sum_k \rightarrow \int_{-1}^1 d\varepsilon \rho(\varepsilon). \quad (3.4)$$

The transformation in Eq. (3.3) is defined such that the standard fermionic anticommutation relation $\{\hat{a}_{\varepsilon\sigma}, \hat{a}_{\varepsilon'\sigma'}^\dagger\} = \delta(\varepsilon - \varepsilon')\delta_{\sigma\sigma'}$ applies. Note that with this, the operators $\hat{a}_{\varepsilon\sigma}^{(\dagger)}$ acquire unit (energy) $^{-\frac{1}{2}}$, and thus only the combination in Eq. (3.3) is dimensionless.

The bath then covers a continuous excitation spectrum and the Hamiltonian reads

$$\hat{H} = \hat{H}_{\text{imp}} + \sum_{\sigma} \int_{-1}^1 d\varepsilon \varepsilon \hat{a}_{\varepsilon\sigma}^\dagger \hat{a}_{\varepsilon\sigma} + \sum_{\sigma} \int_{-1}^1 d\varepsilon \sqrt{\frac{\Gamma(\varepsilon)}{\pi}} (\hat{d}_{\sigma}^\dagger \hat{a}_{\varepsilon\sigma} + \text{h.c.}), \quad (3.5)$$

with the energy representation of the hybridization function

$$\Gamma(\varepsilon) \equiv \pi \rho(\varepsilon) V^2(\varepsilon). \quad (3.6)$$

It is this continuous form of the Hamiltonian Eq. (3.5) that needs to be discretized.

3.1.2 Logarithmic discretization

For the logarithmic discretization of the conduction band, K. G. Wilson [15] introduced a discretization parameter $\Lambda > 1$, which defines the discretization points as

$$\epsilon_n = \Lambda^{-n}, \quad n = 0, 1, 2, \dots, \quad (3.7)$$

with $\epsilon_n > \epsilon_{n+1}$, leading to intervals

$$I_n = \begin{cases} [-\epsilon_{|n|}, -\epsilon_{|n+1|}] & \text{for } n < 0 \\ [\epsilon_{|n+1|}, \epsilon_{|n|}] & \text{for } n > 0 \end{cases} \quad (3.8)$$

with logarithmically decreasing width $d_n \equiv \epsilon_n - \epsilon_{n+1} = \Lambda^{-(n+1)}(\Lambda - 1)$. Typical values for Λ are 1.5 up to 4, depending on the complexity of the impurity site. In principle, the continuum limit is recovered by taking $\Lambda \rightarrow 1$.

The continuous energy support of the bath can now be coarse-grained in terms of the logarithmic intervals

$$\int_{-1}^1 d\varepsilon \rightarrow \sum_n \int_{I_n} d\varepsilon, \quad (3.9)$$

resulting in the exact representation of the coupling term \hat{H}_{cpl} ,

$$\sum_{\sigma} \int_{-1}^1 d\varepsilon \sqrt{\frac{\Gamma(\varepsilon)}{\pi}} (\hat{d}_{\sigma}^{\dagger} \hat{a}_{\varepsilon\sigma} + \text{h.c.}) = \sum_{\sigma} (\hat{d}_{\sigma}^{\dagger} \sum_n \gamma_n \hat{a}_{n0\sigma} + \text{h.c.}). \quad (3.10)$$

Here we have introduced

$$\hat{a}_{n0\sigma} \equiv \frac{1}{\gamma_n} \int_{I_n} d\varepsilon \sqrt{\frac{\Gamma(\varepsilon)}{\pi}} \hat{a}_{\varepsilon\sigma} \equiv \int_{I_n} d\varepsilon \Phi_{n\sigma}^*(\varepsilon) \hat{a}_{\varepsilon\sigma}, \quad (3.11)$$

where

$$\gamma_n = \sqrt{\int_{I_n} d\varepsilon \frac{\Gamma(\varepsilon)}{\pi}} \quad (3.12)$$

represents a proper normalization, such that $\hat{a}_{n0\sigma}^{(\dagger)}$ are standard fermionic operators, that destroy (create) particles of spin σ in the bath interval I_n , respectively. In principle, they can be completed into a basis set of orthonormal polynomials (labeled by the integer p)

$$\hat{a}_{np\sigma} = \int_{I_n} d\varepsilon \Phi_{np}^*(\varepsilon) \hat{a}_{\varepsilon\sigma}, \quad (3.13)$$

such that the continuous bath operators can be written as

$$\hat{a}_{\varepsilon\sigma} = \sum_{np} \Phi_{np}(\varepsilon) \hat{a}_{np\sigma}. \quad (3.14)$$

By construction, the impurity directly couples to the $p = 0$ components of the conduction band states only. Thus the hybridization term is still represented exactly, neglecting the $p \neq 0$ states for the discretization of the conduction band term. In contrast, the bath Hamiltonian is approximated by

$$\sum_{\sigma} \int_{-1}^1 d\varepsilon \varepsilon \hat{a}_{\varepsilon\sigma}^{\dagger} \hat{a}_{\varepsilon\sigma} \approx \sum_{n\sigma} \xi_n \hat{a}_{n0\sigma}^{\dagger} \hat{a}_{n0\sigma}. \quad (3.15)$$

While in general $\langle np\sigma | \hat{H}_{\text{bath}} | np'\sigma \rangle \neq \delta_{pp'}$, we only keep the terms $p = p' = 0$ for the representative energies ξ_n in the intervals I_n :

$$\xi_n \equiv \langle n0\sigma | \hat{H}_{\text{bath}} | n0\sigma \rangle = \frac{\int_{I_n} d\varepsilon \Gamma(\varepsilon) \varepsilon}{\int_{I_n} d\varepsilon \Gamma(\varepsilon)}, \quad (3.16)$$

where $|np\sigma\rangle \equiv \hat{a}_{np\sigma}^{\dagger} | \rangle$ and $| \rangle$ denotes the vacuum state.

Altogether the discretization procedure approximates the bath Hamiltonian by only one single state per interval (see Fig. 3.1 (b)), which replace the originally infinite many continuous states in that interval, while keeping the overall coupling of the impurity to the bath exact,

$$\hat{H} = \hat{H}_{\text{imp}} + \sum_{n\sigma} \xi_n \hat{a}_{n0\sigma}^{\dagger} \hat{a}_{n0\sigma} + \sum_{\sigma} (\hat{d}_{\sigma}^{\dagger} \sum_n \gamma_n \hat{a}_{n0\sigma} + \text{h.c.}). \quad (3.17)$$

The coarse graining influences the calculation of physical quantities. Firstly, it has the the shortcoming of (slightly) misrepresenting the effective hybridization of the bath. This, however,

can be systematically improved upon ([26] and [27]). Second and more importantly, the Wilson chain lost its character as a true thermal bath by eliminating a large degree of fermionic levels. A general method to increase the resolution of physical quantities and to reduce artificial oscillations due to the discretization is to average over the obtained data of various (N_z) discretization grids for fixed Λ (“z-averaging”) [28]. To this end, one introduces a parameter z , uniformly distributed in $(0, 1]$, that shifts the original discretization points:

$$\epsilon_1^z = 1 \quad \text{and} \quad \epsilon_n^z = \Lambda^{2-n-z} \quad \text{for} \quad n = 2, 3, \dots \quad (3.18)$$

However, the z-averaging procedure cannot replace the true continuum limit $\Lambda \rightarrow 1$ by taking the limit $N_z \rightarrow \infty$.

In this work, we will mainly use a slight variation of the grid given in Eq. (3.18) and Eq. (3.17) to discretize the Hamiltonian (see Sec. 4.2.1). Moreover, we exploit the fact that within DMFT we only have to calculate the self-energy with NRG. As R. Bulla pointed out in 1998 [16], this quantity can be determined via the ratio of a two-particle and a one-particle retarded Green’s function (see Sec 4.1). This “self-energy-trick” leads to a reduction of systematic errors for the calculation of the self-energy within NRG and significantly reduces artificial oscillations, dispensing with the need for a discretization correction.

As we will discuss in detail in Sec. 4.2, an appropriate choice of the discretization intervals is absolutely essential within DMFT. As one has to handle hybridization functions of arbitrary shape, the concrete way of discretizing the Hamiltonian can have strong impact on the overall efficiency and accuracy of the NRG calculations. Therefore we will also investigate an alternative discretization scheme in Sec. 4.2.2, which was suggested by R. Zitko in 2009 [27] and takes the actual shape of the hybridization function into account. It is based on the requirement to exactly reproduce the conduction band density of states after z-averaging of the bath alone.

3.1.3 Mapping onto the Wilson tight-binding chain

The next step of the NRG procedure is an exact mapping of the discrete Hamiltonian onto a semi-infinite tight-binding chain. The coupling term of the Hamiltonian directly leads to the introduction of a new conduction band state,

$$\hat{f}_{0\sigma} = \frac{1}{\sqrt{\xi_0}} \sum_n \gamma_n \hat{a}_{n0\sigma}, \quad (3.19)$$

with normalization constant

$$\xi_0 = \sum_n \gamma_n^2 = \int_{-1}^1 d\varepsilon \frac{\Gamma(\varepsilon)}{\pi}, \quad (3.20)$$

representing all bath states that are directly coupled to the impurity. This motivates a complete unitary transformation from the set of bath operators $\hat{a}_{n0\sigma}^{(\dagger)}$ to a new set of mutually orthogonal operators $\hat{f}_{n\sigma}^{(\dagger)}$ that exhibit only nearest-neighbour coupling [22]. The transformation can be achieved by a standard tridiagonalization procedure (e.g. Lanczos algorithm, see Sec. 4.2.1). As a result, we obtain the Wilson chain Hamiltonian:

$$\hat{H} = \hat{H}_{\text{imp}} + \sqrt{\xi_0} \sum_{\sigma} (\hat{d}_{\sigma}^{\dagger} \hat{f}_{0\sigma} + \text{h.c.}) + \sum_{\sigma, n=0}^{\infty} [\varepsilon_n \hat{f}_{n\sigma}^{\dagger} \hat{f}_{n\sigma} + t_n (\hat{f}_{n\sigma}^{\dagger} \hat{f}_{n+1\sigma} + \text{h.c.})]. \quad (3.21)$$

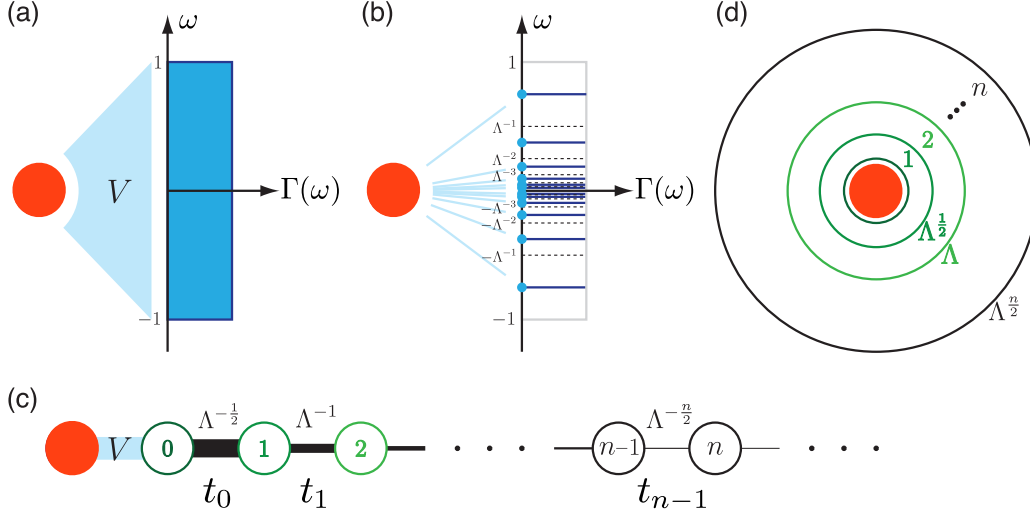


Figure 3.1: Sketch of the main steps for mapping an impurity model onto a Wilson chain. Here we consider the SIAM with a constant hybridization function Γ (or k -independent V , respectively). Panel (a) shows the impurity model, where an impurity (red) is coupled to a non-interacting fermionic bath via the hybridization V . The first step of Wilson's NRG approach is to coarse-grain the energy band by logarithmic discretization and to integrate out the bath degrees of freedom in every interval. This leads to a model with a discrete set of states (blue circles) as depicted in (b), that still features the same coupling to the impurity as in the original model. The discretized Hamiltonian is then mapped onto a semi-infinite tight-binding chain shown in panel (c). The exponentially decaying couplings of the Wilson chain are illustrated by thinning bonds between the different sites. The coupling of the impurity to the first Wilson chain site is again given by V . Panel (d) presents the physical interpretation of the Wilson chain sites as a sequence of shells with exponentially growing size, centered around the impurity. Figure adapted from [14].

The very first site of this semi-infinite tight-binding chain represents the impurity ($\hat{d}_\sigma^{(\dagger)}$), which is coupled to the first site of the conduction band ($\hat{f}_{0\sigma}^{(\dagger)}$) with strength $\sqrt{\xi_0}$. All other sites of the chain belong to the bath and couple to their next neighbor via the hopping matrix elements t_n . The on-site energies are given by ε_n , where $\varepsilon_n = 0$ for all n if $\Gamma(\omega) = \Gamma(-\omega)$. For a constant hybridization Γ , one can derive an analytical expression for t_n [15]:

$$t_n = \left(\frac{(1 + \Lambda^{-1})(1 - \Lambda^{-n-1})}{2\sqrt{1 - \Lambda^{-2n-1}}\sqrt{1 - \Lambda^{-2n-3}}} \right) \Lambda^{-\frac{n}{2}} \quad n \gg 1 \quad \left(\frac{1 + \Lambda^{-1}}{2} \right) \Lambda^{-\frac{n}{2}}. \quad (3.22)$$

For a non-constant hybridization $\Gamma(\omega)$, t_n is calculated numerically. Either way, due to the underlying logarithmic coarse graining, the hopping matrix elements fall off exponentially for large n :

$$t_n \xrightarrow{n \gg 1} \Lambda^{-\frac{n}{2}}. \quad (3.23)$$

Note that we will later refer to $t_n \sim \Lambda^{-\frac{n+1}{2}}$ for large n , which is convention. This behavior is a direct consequence of the logarithmic discretization Eq. (3.7) and is of major conceptual importance for the whole method to work. The tight-binding chain with exponentially decreasing couplings is depicted in Fig. 3.1(c).

While the operator $\hat{d}_\sigma^{(\dagger)}$ of the impurity part of the SIAM Hamiltonian Eq. (2.33a) acts on the

impurity site, the operator $f_{n\sigma}^{(\dagger)}$ annihilates (or creates) a particle at site n of the Wilson chain. The physical interpretation of these Wilson chain sites is a sequence of shells in the bath, centered around the impurity in position space (see Fig. 3.1 (d)). The wave function corresponding to the Wilson chain operator $\hat{f}_{0\sigma}$ shows a maximum closest to the impurity. Therefore $\hat{f}_{0\sigma}^{(\dagger)}$ annihilates (or creates) electrons at the location of the impurity. Analogously, the operators $\hat{f}_{n\sigma}^{(\dagger)}$ ($n > 0$) act on shells further away from the impurity. The size of the spherical shells is growing exponentially, which is related to the exponential decrease of the hopping matrix elements [15]. In the case of the SIAM Hamiltonian with only $n_c = 2$ different types of electrons (spin up and spin down), every site of the Wilson chain can display four different states $|\sigma_n\rangle = \{|0\rangle, |\uparrow\rangle, |\downarrow\rangle, |\uparrow\downarrow\rangle\}$, an unoccupied, a singly occupied with spin up or spin down and a doubly occupied site n . Therefore the Hilbert space for one site has dimension $d = 2^{(n_c=2)} = 4$. If we consider a more complex model with two impurity levels, where each couples to a separate conduction electron band, the site dimension increases to $d = 2^{(n_c=4)} = 16$. Altogether, the size of the Hilbert space for the whole chain Hamiltonian grows like $d_{\text{imp}} d^{n+1}$, when considering the Wilson chain up to and including site n . Here d_{imp} represents the local dimension of the impurity site. Therefore this many-body system can generally not be solved exactly. Yet, there is a controlled numerical procedure to tackle such problems, presented in the following.

3.1.4 Iterative renormalization group procedure

The Wilson chain Hamiltonian Eq. (3.21) can be solved using an iterative renormalization group (RG) procedure invented by K.G. Wilson [15]. This introduces a series of Hamiltonians \hat{H}_N :

$$\hat{H}_N = \Lambda^{\frac{N}{2}} \left[\hat{H}_{\text{imp}} + \sqrt{\xi_0} \sum_{\sigma} (\hat{d}_{\sigma}^{\dagger} \hat{f}_{0\sigma} + \text{h.c.}) + \sum_{\sigma, n=0}^N \varepsilon_n \hat{f}_{n\sigma}^{\dagger} \hat{f}_{n\sigma} + \sum_{\sigma, n=0}^{N-1} t_n (\hat{f}_{n\sigma}^{\dagger} \hat{f}_{n+1\sigma} + \text{h.c.}) \right] \quad (3.24)$$

with a scaling factor $\Lambda^{\frac{N}{2}}$, canceling the N -dependence of t_{N-1} , which will be useful for the investigation of flow diagrams in Sec. (3.1.5). The original Hamiltonian is then obtained as

$$\hat{H} = \lim_{N \rightarrow \infty} \Lambda^{-\frac{N}{2}} \hat{H}_N. \quad (3.25)$$

From Eq. (3.24) one arrives at the recursion relation

$$\hat{H}_N = \sqrt{\Lambda} \hat{H}_{N-1} + \Lambda^{\frac{N}{2}} \sum_{\sigma} \varepsilon_N \hat{f}_{N\sigma}^{\dagger} \hat{f}_{N\sigma} + \Lambda^{\frac{N}{2}} \sum_{\sigma} t_{N-1} (\hat{f}_{N-1\sigma}^{\dagger} \hat{f}_{N\sigma} + \text{h.c.}), \quad (3.26)$$

which can be interpreted as a renormalization group transformation R :

$$\hat{H}_N = R(\hat{H}_{N-1}) \quad (3.27)$$

(see Sec. (3.1.5) for a discussion of the RG aspect). Using Eq. (3.26) and

$$\hat{H}_0 = \Lambda^{-\frac{1}{2}} \left[\hat{H}_{\text{imp}} + \sum_{\sigma} \varepsilon_0 \hat{f}_{0\sigma}^{\dagger} \hat{f}_{0\sigma} + \sqrt{\xi_0} \sum_{\sigma} (\hat{d}_{\sigma}^{\dagger} \hat{f}_{0\sigma} + \text{h.c.}) \right] \quad (3.28)$$

as starting point, we can solve the Wilson chain Hamiltonian Eq. (3.25) by iterative diagonalization.

First we diagonalize the Hamiltonian \hat{H}_0 exactly and obtain a set of eigenstates and eigenenergies. Then we continue with \hat{H}_1 .

For a general RG step from site $N - 1$ to N , one applies the strategy in Fig. 3.2:

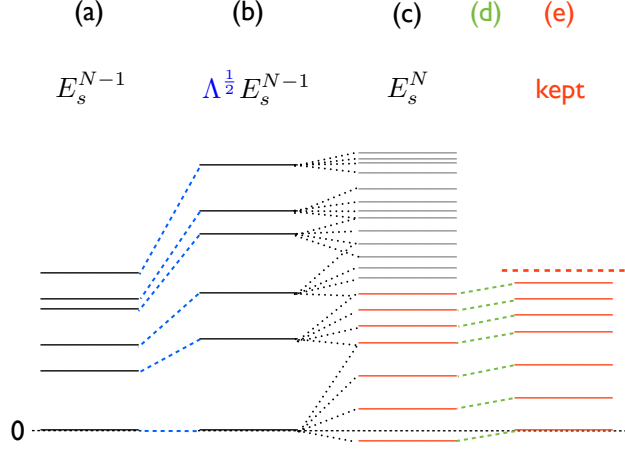


Figure 3.2: General RG step from site $N - 1$ to N : The many-particle spectrum E_s^{N-1} of iteration $N-1$, shown in (a), is rescaled by $\Lambda^{\frac{1}{2}}$, as depicted in (b). Then a new site N of the Wilson chain is added, lifting the degeneracy of the eigenenergies E_s^{N-1} by diagonalization of the new system. This leads to the eigenenergies E_s^N with respect to site N in (c), which are shifted in (d) such that the new ground state has zero energy. In (e) the state space of shell N is truncated with respect to a certain energy E_{keep} , indicated by the dashed red line.

- (a) In the preceding iteration \hat{H}_{N-1} was diagonalized as $\hat{H}_{N-1} |s\rangle_{N-1} = E_s^{N-1} |s\rangle_{N-1}$ with eigenenergies E_s^{N-1} and eigenstates $|s\rangle_{N-1}$.
- (b) The first term in the recursion relation Eq. (3.26) rescales the eigenenergies E_s^{N-1} with level spacing of order 1, by $\sqrt{\Lambda}$.
- (c) Then a new site of the Wilson chain is added via the second and third term of Eq. (3.26), which can be regarded as a perturbation of order $\Lambda^{-\frac{1}{2}} < 1$, lifting the degeneracy of the eigenenergies E_s^{N-1} . As the new site is represented by a basis set $|\sigma_N\rangle$ of dimension d , the Hilbert space for \hat{H}_N grows by a factor of d , leading to an enlarged basis set $|s, \sigma\rangle_N = |\sigma_N\rangle \otimes |s\rangle_{N-1}$ for the matrix representation of \hat{H}_N . Diagonalization of this matrix yields the new eigenvalues $E_{s'}^N$ with corresponding eigenstates $|s'\rangle_N$, which are connected to the old states $|s\rangle_{N-1}$ via an unitary transformation $A^{[N]}$:

$$|s'\rangle_N = \sum_{\sigma_N s} [A^{[\sigma_N]}]_{s s'} |\sigma_N\rangle |s\rangle_{N-1}. \quad (3.29)$$

$A^{[N]}$ stands for all of the d matrices $[A^{[\sigma_N]}]_{s s'} = (\langle s|_{N-1} \langle \sigma_N|) |s'\rangle_N$. This specific formulation of the unitary transformation exhibits the structure of so called matrix product states (MPS). It will turn out in Sec. 3.2 that an implementation of the whole NRG procedure in terms of MPS is quite powerful.

- (d) In a next step, the ground state energy of iteration N is set to zero, for convenience.

(e) As already pointed out, it is numerically not feasible to keep all the eigenstates and eigenenergies during the complete iterative procedure as the Hilbert space grows exponentially with the added sites of the Wilson chain. Hence, we have to truncate the state space from a certain iteration N_0 onwards (typically $N_0 \approx 5$ for the one-band model) and fix the size of the Hilbert space, which can be done by keeping only the D lowest lying eigenstates.

This truncation scheme is motivated by the fact that an additional site can be seen as a perturbation of relative strength $\Lambda^{-\frac{1}{2}}$. In perturbation theory, the influence of high-energy states on the low-energy spectrum is small, if the perturbation is weak compared to the energy of the high lying levels. Thus, the basic NRG assumption of energy scale separation can be justified for sufficiently large Λ (typically $\Lambda \gtrsim 2$).

Instead of keeping a fixed number of states, we can also truncate with respect to a fixed rescaled energy E_{keep} , which corresponds more to the idea of energy scale separation. Each site of the Wilson chain features a characteristic energy scale or resolution

$$\omega_N = a\Lambda^{-\frac{N}{2}} \quad (3.30)$$

with a chosen such that the rescaled couplings approach unity for sufficiently large Wilson chains: $\lim_{N \rightarrow \infty} \left(\frac{t_{N-1}}{\omega_N} \right) = 1$. So E_{keep} is kept fixed and is given in units of ω_N for the different sites N .

Indeed, there is a priori no guarantee for a specific truncation parameter D or E_{keep} to give good results. One way to test the validity of the truncation scheme is to vary the truncation parameter and observe its influence on the outcome. In this work however, we use a quantitative criterion (called discarded weight) to analyze convergence for a given NRG calculation, which can be extracted from the same NRG run (see Sec. 3.2.5 and A. Weichselbaum 2011 [24] for more details).

We stop our iterative procedure by discarding all states at the Wilson chain site N_{max} , which is determined through the required energy resolution for the actual physical problem.

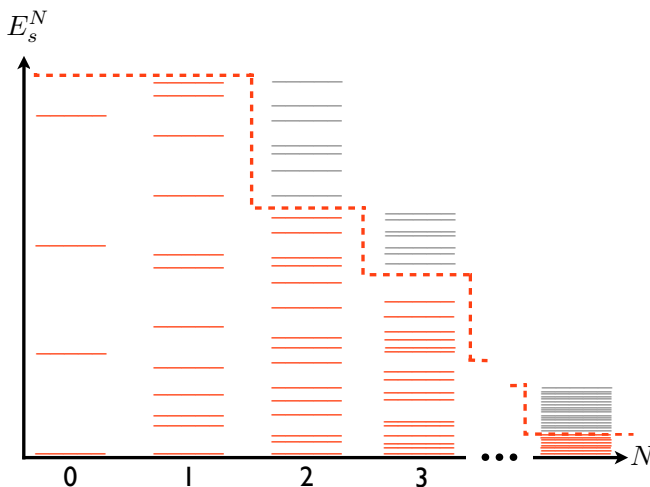


Figure 3.3: Sketch of the unscaled energy levels of the different Wilson chain sites with ground state energies set to zero. While the kept states are successively refined with every step of the iterative procedure the discarded states remain degenerate. Adapted from [14].

Remarkably, it is possible to construct a complete basis from all discarded states of all iterations as will be presented in Sec. 3.2.3, which can then be used to calculate physical quantities.

Altogether the iterative procedure, described here, leads successively to an increasing resolution of the low energy spectrum (described by the kept states), while the discarded high-energy states remain degenerate (see Fig. 3.3).

3.1.5 Renormalization group flow

As indicated by Eq. (3.27) the whole iterative procedure can be interpreted as a RG transformation. In general, a RG transformation R maps a certain Hamiltonian $\hat{H}(\vec{K})$, depending on a set of parameters \vec{K} , on a Hamiltonian of the same form with renormalized parameters \vec{K}' : $R(\hat{H}(\vec{K})) = H(\vec{K}')$ [23]. The parameters normally display a RG flow to certain fixpoints. However in the case of NRG, the Hamiltonian does not have the same form before and after the RG transformation, except for the case that the system reached a stable fixed point (up to even-odd alternations). Nevertheless it is possible to extract information about the physics of the impurity model by analyzing the flow of the (rescaled) eigenenergies E_s^N along the Wilson chain sites N . Depending on the specific model the energy flow diagram can show different fixed points regimes, which are connected to different physical behavior of the system. For the SIAM with constant hybridization function, three different regimes can be found: the free orbital regime for very small N , the local moment regime for intermediate N and the strong coupling regime below T_K , which is also called Fermi-liquid fixed point (see [22] for a detailed discussion and Fig. 3.4 for a plot). Within DMFT the flow diagram also gives a hint to the physics of the system. For the one-band Hubbard model, for example, a Fermi-liquid fixed point is reached in the metallic regime (see Sec. 5 for more details on the one-band Hubbard model).

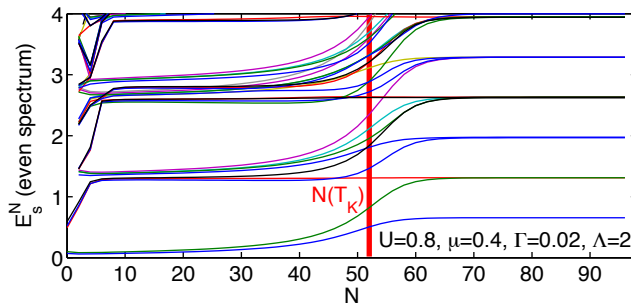


Figure 3.4: Energy flow diagram for the symmetric SIAM with constant hybridization $\Gamma = 0.02$, $U = 0.8$, $\varepsilon_d = -U/2$, $\Lambda = 2$ and $E_{\text{keep}} = 7$. Here only even NRG iterations are plotted as fermionic finite-size systems show even-odd oscillations in their many-particle spectrum (a similar picture is obtained for odd iterations). For the first few sites we find the free orbital regime where the impurity is hardly affected by the coupling to the bath. Between sites $N \approx 10$ and $N \approx 35$ the impurity still features a definite spin but exhibits spin fluctuations. The Kondo temperature ($T_K = 1.348 \cdot 10^{-8}$) is associated with the crossover (at around $N = 52$) to the strong coupling regime where the local impurity moment is completely screened by the conduction band electrons.

3.2 NRG in Matrix Product State (MPS) formulation

During the whole iterative RG procedure, we have to keep track of all the calculated kept and discarded states and the corresponding eigenenergies. Eq. (3.29) suggests to use the unified framework of matrix product states (MPS), as each step of the iterative diagonalization can be expressed as a basis transformation in terms of A-matrices. For a general introduction to MPS we refer the reader to [29]. In the following, we want to denote operators with a hat and their matrix representation without hat, respectively.

3.2.1 Basis states in terms of MPS

Reinserting the definition of the basis states Eq. (3.29) for all iterations up to N, this expresses an arbitrary eigenstate $|s'\rangle_N^X$ in terms of a sum over a product of matrices:

$$|s'\rangle_N^X = \sum_{\sigma_N s} [A_{KK}^{[\sigma_N]}]_{ss'} |\sigma_N\rangle |s\rangle_{N-1}^K \quad (3.31)$$

$$= \sum_{\sigma_N \dots \sigma_0 \sigma_{\text{imp}}} [A_{KK}^{[\sigma_0]} \dots A_{KK}^{[\sigma_{N-1}]} A_{KX}^{[\sigma_N]}]_{\sigma_{\text{imp}} s} |\sigma_N\rangle \otimes |\sigma_{N-1}\rangle \otimes \dots \otimes |\sigma_0\rangle \otimes |\sigma_{\text{imp}}\rangle \quad (3.32)$$

with $X = K$ or D for kept or discarded states, respectively. $|\sigma_{\text{imp}}\rangle$ represents the impurity basis. The A-matrices, written as $[A_{KK}^{[\sigma_N]}]_{ss'}$, are three dimensional tensors in the space spanned by $|s\rangle_{N-1}^K$, $|\sigma_N\rangle$ and $|s'\rangle_N^X$. As shown in Fig. 3.5, the MPS formulation has an intuitive diagrammatical representation.

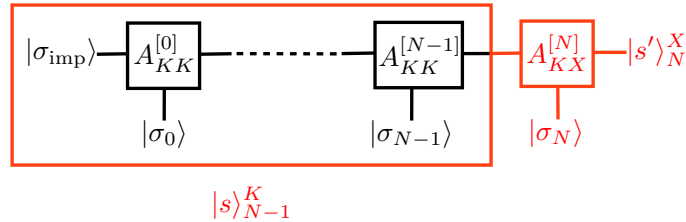


Figure 3.5: Diagrammatical representation of Eq. (3.32). The red part depicts the basis transformation Eq. (3.31). The indices of the corresponding A-matrix appear as legs: s to the left, σ_N at the bottom and s' to the right. In the red box $|s\rangle_{N-1}^K$ is represented in terms of A-matrices as in Eq. (3.32). Connected legs symbolize contractions over the related indices. Figure adapted from [14].

The MPS structure of Eq. (3.32) also makes the evaluation of operators more transparent. Consider the Wilson chain operators in Eq. (3.26). We only store the matrix representation $[f_{N\sigma, \text{loc}}^{(\dagger)}]_{\sigma_N \sigma'_N}$ in terms of the local state space $|\sigma_N\rangle$, and transform it into the required basis by means of the A-matrices:

$$[f_{N\sigma}^{(\dagger)}]_{ss'}^{KK} = {}^K_N \langle s | \hat{f}_{N\sigma}^{(\dagger)} | s' \rangle_N^K = \sum_{\sigma_N \sigma'_N s''} [A_{KK}^{[\sigma_N]}]_{s'' s} [f_{N\sigma, \text{loc}}^{(\dagger)}]_{\sigma_N \sigma'_N} [A_{KK}^{[\sigma'_N]}]_{s'' s'}. \quad (3.33)$$

In addition, there are several other numerical issues, like the handling of fermion signs, emanating from their anti-commutation relations (see [14] for more details), and the implementation of symmetries (see next section). All in all the MPS language allows a very elegant and transparent numerical treatment of the NRG method.

3.2.2 Abelian and non-abelian symmetries

For numerically expensive models, like multi-band models, where the required dimension of the kept state space can get extremely large, it is absolutely crucial to exploit as many symmetries of the model Hamiltonian as possible. Only recently, a general framework for the implementation of non-abelian and abelian symmetries in the context of matrix-product and tensor network states was established by A. Weichselbaum [25]. It uses a computationally straightforward unified tensor representation for quantum symmetry spaces, called QSpace.

Basis states labeled in terms of abelian symmetries, like particle (or charge) conservation, lead to a block-diagonal structure in the matrix representation of the Hamiltonian and subdivide general operators into symmetry sectors due to well-defined selection rules. As a result, all non-zero matrix elements are organized within a few dense data blocks, reducing numerical effort. In the presence of non-abelian symmetries (like $SU(2)_{\text{spin}}$) the matrix elements of these data blocks are not independent of each other and it is possible to further compress them.

To this end, one introduces $|qn; q_z\rangle$ to label the state space in terms of the symmetry eigenbasis. $q \equiv (q^1, q^2, \dots, q^{n_s})$ are the quantum (q-) labels for the irreducible representation of the symmetries S^λ ($\lambda = 1, 2, \dots, n_s$) of the Hamiltonian \hat{H} , with $[\hat{H}, S_\alpha^\lambda] = 0$ and $[S_\alpha^\lambda, S_{\alpha'}^{\lambda'}] = 0$ for $\lambda \neq \lambda'$, resulting in symmetry blocks q . S_α^λ is a specific generator for the symmetry S^λ .

The multiplet index n stands for a particular multiplet within a specific set of conserved quantum numbers, q .

The internal structure of each multiplet in q is given by additional quantum labels q_z^λ (called z-labels), which are completely determined by the symmetries under consideration.

Using this state space label structure, the basis transformation Eq. (3.29) can be written as

$$|\tilde{Q}\tilde{n}; \tilde{Q}_z\rangle = \sum_{Qn; Q_z} \sum_{ql; q_z} \left(A_{Q\tilde{Q}}^{[q]} \right)_{n\tilde{n}}^{[l]} \cdot C_{Q_z\tilde{Q}_z}^{[q_z]} \times |Qn; Q_z\rangle |ql; q_z\rangle, \quad (3.34)$$

where $|Qn; Q_z\rangle$ represents the basis states of the Wilson chain and $|ql; q_z\rangle$ indicates the local state space of one specific site. The basic observation is now that the A-tensors are split into two parts. $\left(A_{Q\tilde{Q}}^{[q]} \right)_{n\tilde{n}}^{[l]}$ acts only on the multiplet level, which leads to a strong size reduction of the A-tensors. The internal multiplet structure, defined by the z-labels, is fully taken care of by the Clebsch Gordan coefficients $C_{Q_z\tilde{Q}_z}^{[q_z]}$.

In the description of operators, the Clebsch Gordan coefficient space also factorizes. Based on the Wigner Eckart theorem, the matrix representation of a specific irreducible operator set \hat{F}^q reads

$$\langle Q'n'; Q'_z | \hat{F}_{q_z}^q | Qn; Q_z \rangle = \left(F_{Q'Q}^{[q]} \right)_{nn'}^{[1]} \cdot C_{Q_zQ'_z}^{[q_z]} \quad (3.35)$$

with the reduced matrix elements $\left(F_{Q'Q}^{[q]} \right)_{nn'}^{[1]} = \langle Q'n' || \hat{F}^q || Qn \rangle$ on the multiplet level. The superscript [1] indicates that we consider a single irreducible operator set.

So all tensor objects, which are relevant for NRG calculations can be split into two (rank-3) structures, operating in the reduced multiplet space and the Clebsch Gordan coefficient space,

respectively. As the final data structure is the same for both spaces, a general tensor representation (of arbitrary rank), the QSpace, is introduced, which allows a well-organized, unified treatment of all NRG operations in terms of symmetries (see [25] for all the details). The QSpace formulation is valid for general non-abelian symmetries (such as $SU(N)$), the symplectic symmetry group, point symmetries and also abelian symmetries. Thus, a maximum number of symmetries can be exploited for a certain model which leads to an enormous gain in numerical efficiency.

3.2.3 Complete basis sets and full density matrix NRG

As already mentioned before, the matrix product states, obtained from the iterative diagonalization, do not span the whole Hilbert space of the chain Hamiltonian as states have been discarded on the way. However, F. B. Anders and A. Schiller pointed out that complete many-body basis sets can be constructed out of the discarded states of all iterations, which, importantly, also represent approximate eigenstates of the full Hamiltonian (see [30] and [30]). Therefore, it is possible to calculate physical quantities like spectral functions very accurately (see [5] for a detailed discussion). These complete basis sets are also easily implemented in the QSpace formalism introduced above.

Up to and including site N_0 , we have a complete set of eigenstates $\{|s\rangle_N^K\}$ for \hat{H}_N if $N \leq N_0$, as for these iterations no states have been truncated. If we want to span the complete Fock space $\mathcal{F}_{N_{\max}}$ of the full chain, we have to include all subsequent sites $N+1$ to N_{\max} by a set of $d^{(N_{\max}-N)}$ degenerate “environmental” states $|e_N\rangle \equiv |\sigma_{N_{\max}}\rangle \otimes \cdots \otimes |\sigma_{N+1}\rangle$, build out of their local state spaces. Then we can write the complete Fock space as

$$\mathbb{1}^{(d_{\text{imp}} d_{N_{\max}+1})} = \sum_{se} |se\rangle_{N_0}^K |se\rangle_{N_0}^K \langle se| \quad (3.36)$$

with $|se\rangle_N^K = |e_N\rangle \otimes |s\rangle_N^K$ for $N \leq N_0$. Analogously, we can define the states

$$|se\rangle_N^X = |e_N\rangle \otimes |s\rangle_N^X \quad (3.37)$$

for $N_0 < N < N_{\max}$ with $X = K, D$ for sites of the Wilson chain, where states have already been discarded. For a general site N , these states can be regarded as approximate eigenstates of the full chain Hamiltonian $\hat{H}_{N_{\max}}$,

$$\hat{H}_{N_{\max}} |se\rangle_N^X \approx E_s^N |se\rangle_N^X, \quad (3.38)$$

with the eigenenergies E_s^N still $d^{(N_{\max}-N)}$ -fold degenerate. Eq. (3.38) is referred to as “NRG-approximation”, emphasizing the basic NRG argument of energy scale separation in this context. The accuracy in energy is determined by the characteristic energy scale ω_N of shell N .

By construction, the discarded states of different shells are orthogonal to each other,

$${}^D_M \langle se | s' e' \rangle_N^D = \delta_{MN} \delta_{e_N e'_N} \delta_{ss'}, \quad (3.39)$$

and also to the kept states of the same shell and shells still to follow:

$${}^K_M \langle se | s' e' \rangle_N^D = \begin{cases} 0 & M \geq N \\ \delta_{e_N e'_N} [A_{KK}^{[\sigma_{M+1}]} \cdots A_{KD}^{[\sigma_N]}]_{ss'} & M < N. \end{cases} \quad (3.40)$$

The overlap of kept states with discarded states of later shells is determined by the A-matrices that map the kept states on the discarded ones.

Using these considerations, we can now introduce complete basis sets for the full Fock space $\mathcal{F}_{N_{\max}}$, given by the discarded states of all iterations,

$$\mathbb{1}(d_{\text{imp}}d_{N_{\max}+1}) = \sum_{N>N_0}^{N_{\max}} \sum_{se} |se\rangle_N^D \langle se|_N^D, \quad (3.41)$$

where we have defined all states of the last iteration N_{\max} as discarded states, for convenience. For the calculation of physical quantities, like spectral functions, we need to perform thermal averages $\langle \dots \rangle = \text{Tr}[\hat{\rho} \dots]$ with the full thermal density matrix $\hat{\rho} = e^{-\beta \hat{H}}/Z$, which can be expressed in terms of the complete basis sets using the NRG-approximation Eq. (3.38) [5]:

$$\hat{\rho} \approx \sum_{N>N_0}^{N_{\max}} \sum_{se} |se\rangle_N^D \frac{e^{-\beta E_s^N}}{Z} \langle se|_N^D = \sum_{N>N_0} w_N \hat{\rho}_{DD}^{[N]} \quad (3.42)$$

with $\beta = \frac{1}{k_B T}$. The eigenenergies E_s^N represent non-rescaled energies relative to a common energy reference. So the full thermal density matrix can be written in terms of properly normalized thermal density matrices for the discarded states of shells $N > N_0$,

$$\hat{\rho}_{DD}^{[N]} = \frac{1}{Z_N} \sum_s e^{-\beta E_s^N} |se\rangle_N^D \langle se|_N^D, \quad (3.43)$$

with $Z_N = \sum_s^D e^{-\beta E_s^N}$ such that $\text{Tr}[\rho_{DD}^{[N]}] = 1$, that enter a sum over all shells $N > N_0$ with relative weight

$$w_N = \frac{Z_N d^{(N_{\max}-N)}}{Z} \quad \text{and} \quad \sum_{N>N_0}^{N_{\max}} w_N = 1. \quad (3.44)$$

The factor $d^{(N_{\max}-N)}$ in w_N takes account of the degeneracy of the environmental states.

In contrast to the widely used ‘‘single-shell approximation’’ $w_N = \delta_{NN_T}$ (with N_T defined by the Wilson chain sites with characteristic energy scales of order of the temperature), the relative weights w_N in the full (thermal) density matrix (FDM) approach [5] are peaked around the shell, corresponding to the energy scale of temperature, with a finite width of several (5 to 10) iterations. Therefore, given a long enough Wilson chain, all relevant shells for a given temperature are automatically included. Thereafter, the Wilson chain effectively terminates on its own.

Calculating physical quantities, the complete basis sets avoid double counting of basis states as occurred in previous methods. General local operators \hat{B} (acting on sites up to N_0) can be simply expressed in terms of the complete basis sets by F. B. Anders and A. Schiller (see [5, Eq. (6)] and [14, Sec. 4.5.2]). Eq. (3.42) can be fully taken care of within the NRG. When tracing out partial environments from earlier shells, these density matrices become reduced density matrices, similar to the ones introduced by W. Hofstetter in his density-matrix (DM)-NRG [31]. The latter, however, was still based on heuristic patching schemes. Moreover, FDM-NRG also allows to fully take care of fermionic signs [32].

3.2.4 Calculation of spectral functions

We can now use the complete basis set and the FDM-NRG approach for the calculation of spectral functions to describe the impurity dynamics in thermal equilibrium. The general definition

of a spectral function reads

$$\mathcal{A}^{BC}(\omega) = \int \frac{dt}{2\pi} e^{i\omega t} \langle \hat{B}(t) \hat{C} \rangle_T \quad (3.45)$$

and the corresponding Lehman representation

$$\mathcal{A}^{BC}(\omega) = \sum_{a,b} \langle b | \hat{C} | a \rangle \frac{e^{-\beta E_a}}{Z} \langle a | \hat{B} | b \rangle \delta(\omega - E_{ba}) \quad (3.46)$$

with $Z = \sum_a e^{-\beta E_a}$ and $E_{ba} = E_b - E_a$. In FDM formulation we get

$$\mathcal{A}^{BC}(\omega) = \sum_N w_N \mathcal{A}_N^{BC}(\omega). \quad (3.47)$$

Expressed in terms of discarded states only, it is possible to calculate $\mathcal{A}^{BC}(\omega)$ by performing a single “backward run” from the last Wilson chain site to the first one, while all eigenstates and eigenenergies were calculated before in a “forward run” (see [24] for a detailed explanation). This way, sum rules, as $\int d\omega \mathcal{A}^{BC}(\omega) = \langle \hat{B} \hat{C} \rangle_T$, are fulfilled to high accuracy ($\sim 0.01\%$ after broadening of the discrete data) [24].

After a NRG run we obtain Eq. (3.47) as a sum over discrete data points (ω_j, a_j) :

$$A_{\text{raw}}(\omega) = \sum_j a_j \delta(\omega - \omega_j). \quad (3.48)$$

To broaden this sequence of δ -peaks we define a broadening kernel $K(\omega, \omega')$ representing a log-Gaussian function with frequency-dependent width (dealing with the fact that we have less dense data at large frequencies due to the logarithmic discretization) above a certain frequency ω_0 . Below ω_0 , a smooth transition from the log-Gaussian to a regular Gaussian of width ω_0 sets in to get finite values for $\omega \rightarrow 0$.

So the smoothed spectral function is defined by

$$A(\omega) \equiv \int d\omega' K(\omega, \omega') A_{\text{raw}}(\omega') \quad (3.49)$$

with

$$K(\omega, \omega') = \frac{\Theta(\omega, \omega')}{\sqrt{\pi} \sigma |\omega|} e^{-\left(\frac{\log|\omega'/\omega|}{\sigma} - \frac{\sigma}{4}\right)^2} \quad \text{for } |\omega'| \leq \omega_0 \quad (3.50)$$

and a broadening parameter σ . A detailed discussion of the broadening kernel is given in the appendix of [5].

For the DMFT application it is important to choose σ as small as possible to carve out the complete structure of the hybridization function during the DMFT self-consistency procedure. However very strong artificial oscillations should be avoided as well, because these are possibly not completely corrected by the “self-energy-trick” and can grow during the DMFT iterations. See Fig 3.6 for an example of broadened raw data for the spectral function of the one-band Hubbard model.

For the calculations within this work, we mainly apply the following strategy. First, we roughly reach convergence within the DMFT self-consistency procedure by applying no z -averaging and larger broadening. Then, we refine the structure of the hybridization function by performing some more iterations using z -averaging and an appropriate smaller value for σ until convergence is also reached for these parameters.

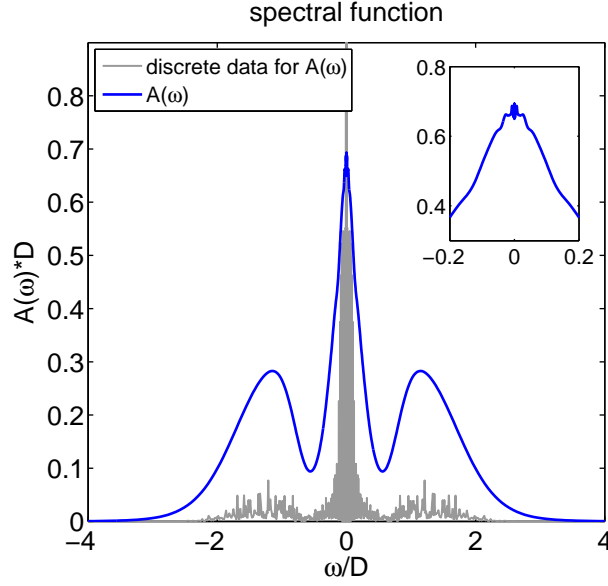


Figure 3.6: Smoothened spectral function (local density of states) for the particle-hole-symmetric one-band Hubbard model with $U/D = 2$, $\mu/D = U/2$, $T/D \approx 0$, $N_z = 4$ and $\Lambda = 2$. In grey the raw data is plotted as $\frac{A_{\text{raw}}(\omega) \cdot 8}{|\omega|}$. The blue curve represents the smoothened spectral function $A(\omega)$. With a broadening of $\sigma = 0.2$ the spectral function still shows artificial oscillations around $\omega = 0$, as can be observed in the inset. These artefacts can be reduced by applying the “self-energy-trick” (see Fig. 4.1).

3.2.5 Discarded weight in NRG

To the end of the chapter about the NRG method, we want to introduce the discarded weight mentioned during the description of the iterative diagonalization procedure, which can be regarded as a control parameter that indicates, if the whole NRG run was successful.

The numerical treatment of the iterative RG procedure is based on the truncation of high-energy states, rationalized by energy-scale separation along the Wilson chain. However, it is not clear a priori how many low-energy states one should keep for an appropriate description of the low-energy spectrum still to follow. Motivated by the density matrix renormalization group, where an a priori truncation of the state space can be defined through the discarded weight in its reduced density matrix, a similar criterion within NRG was introduced by A. Weichselbaum in 2011 [24]. It is based on the question how important states kept some iterations earlier have de facto been for the specification of the ground state at iteration N' . To analyze this influence quantitatively, we consider the fully mixed density matrix of the $g_{N'}$ -fold degenerate ground state space G at iteration N' :

$$\hat{\rho}_{0,N'} \equiv \frac{1}{g_{N'}} \sum_{s \in G} |s\rangle_{N'} \langle s| \quad (3.51)$$

with a Schmidt rank equal to $g_{N'}$ and trace out its N_0 smallest energy shells to arrive at the reduced density matrix $\hat{\rho}_0^{[N;N_0]}$ ($N = N' - N_0$), which can be expressed in terms of the kept states of iteration N (see Eq. (3.53)).

To trace out one site, a so called “backward update” is performed (see Fig. 3.7):

$$\hat{\rho}_{n-1}^{[K]} = \sum_{s_{n-1} s'_{n-1} \sigma_n} \left(A_{KX}^{[\sigma_n]} \rho_n^{[X]} A_{KX}^{[\sigma_n]\dagger} \right)_{s_{n-1} s'_{n-1}} |s\rangle_{n-1} \langle s'| \equiv \hat{\mathcal{P}} \hat{\rho}_n^{[X]} \quad (3.52)$$

with an arbitrary density matrix $\hat{\rho}_n^{[X]} \equiv \sum_{s_n s'_n \in X} \rho_{s_n s'_n}^{[X]} |s\rangle_n \langle s'|$ and $X = K, D$.

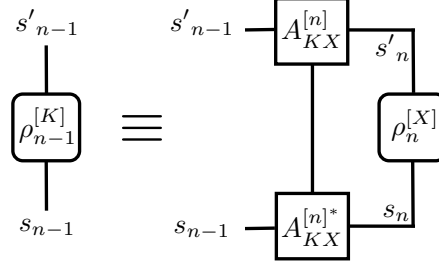


Figure 3.7: Graphical representation of a “backward update” as given in Eq. (3.52). Figure adapted from [24].

So the reduced density matrix is calculated as

$$\hat{\rho}_0^{[N;N_0]} \equiv \left(\prod_{n=N+1}^{N+N_0} \hat{\mathcal{P}}_n \right) \hat{\rho}_{0,N'} \equiv \sum_{ss'}^D \rho_{ss'}^{[N;N_0]} |s\rangle_N^K \langle s'| \quad (3.53)$$

with $N_0 \gtrsim \text{ceil}[\log(D)/\log(d)]$ and $N_0 \ll N_{\max}$ as the number of sites until the Schmidt rank has grown to the full dimension D of the kept space. In principle, N_0 is also the number of NRG iterations at the beginning of the iterative RG procedure where no states are truncated.

For further investigations the reduced density matrix is diagonalized:

$$\hat{\rho}_0^{[N;N_0]} |r_{N;N_0}\rangle = \rho_r^{[N;N_0]} |r_{N;N_0}\rangle. \quad (3.54)$$

The eigenvalues $\rho_r^{[N;N_0]}$ indicate the importance of a specific linear combination $|r_{N;N_0}\rangle$ of NRG eigenstates $|s\rangle_N^K$ for the low-energy physics of later iterations. The energies of the eigenbasis $|r_{N;N_0}\rangle$ are given by the expectation values

$$E_r^{[N;N_0]} \equiv \langle r_{N;N_0} | \hat{H}_N | r_{N;N_0} \rangle. \quad (3.55)$$

It can be shown that the resulting data (E_r, ρ_r) are clearly correlated and small weights ρ_r correspond to high energies E_r , as intuitively expected (see [24] for a detailed discussion). The largest discarded weight, which describes the weight missing due to the discarded states at iteration N , can then be well approximated by the smallest weights of the reduced density matrix $\hat{\rho}_0^{[N;N_0]}$ in the kept space. Therefore an a priori measure for the accuracy of the truncation criteria at iteration N is defined through the average weights $\rho_r^{[N;N_0]}$, that are obtained for the highest energies $E_r^{[N;N_0]}$ in the kept space [24]:

$$\varepsilon_N^{D_\chi} \equiv \begin{cases} \langle \rho_r^{[N;N_0]} \rangle_{E_r^{[N;N_0]} \geq (1-\chi) \max(E_r^{[N;N_0]})} & \text{with truncation at iteration } N \\ 0 & \text{without truncation at iteration } N \end{cases} \quad (3.56)$$

with typically $\chi \approx 0.05$. The overall discarded weight for the whole chain is given by the largest discarded weight of all iterations:

$$\varepsilon_\chi^D \equiv \max_N (\varepsilon_N^{D_\chi}). \quad (3.57)$$

In the DMFT calculations we will have to deal with numerically expensive models as well as with models where energy scale separation is not guaranteed due to non-constant hybridization functions or modified discretization schemes. Therefore the discarded weight is especially helpful to judge the accuracy of NRG data within DMFT. If it is small ($< 10^{-12}$), the NRG run is reliably converged.

To conclude, the NRG program, developed by Andreas Weichselbaum, is implemented in a highly systematic way. The MPS formulation is based on complete basis sets and correlation functions are calculated with the full density matrix, enhancing the accuracy of the NRG results. Furthermore, a quantitative convergence measure, the discarded weight, is on hand to estimate the quality of a NRG run. This is especially advantageous for DMFT applications where previous checks, like repeating a single run with different parameters, is quite bothersome. Besides, our NRG program is the first (and up to now only program) to use arbitrary non-abelian symmetries and thus can tackle physical problems that would not have been feasible before.

Chapter 4

Combining DMFT and NRG

In this chapter we want to discuss the peculiarities that emerge when NRG is used as an impurity solver within DMFT.

The quantity of interest that has to be generally calculated with the “impurity solver” is the one-particle self-energy. Instead of using the Dyson equation as in other approaches, it has proven to be considerably more accurate within NRG to write the self-energy as the ratio of a two-particle and a one-particle Green’s function as introduced by R. Bulla in 1998 [16]. This “self-energy trick” was already mentioned in the derivation of the self-consistency procedure. In the following section we want to give a detailed explanation.

Another important issue is the specific form of the discretization grid for the NRG run. For a constant hybridization function the conventional logarithmic discretization grid leads to exponentially decaying hopping matrix elements along the Wilson chain. The DMFT self-consistency procedure, however, yields a frequency-dependent input hybridization function $\Gamma(\omega)$ at each DMFT iteration, for which the standard discretization scheme leads to Wilson chain couplings that do not necessarily decay exponentially over a certain range of sites, calling the basic NRG assumption of energy separation into question. Therefore we want to debate some variations of the conventional logarithmic discretization scheme in Sec. 4.2.

4.1 Calculation of the self-energy

At a first glance a natural choice to calculate the self-energy of the effective quantum impurity model is to use the Dyson equation $\Sigma(\omega) = G_{\text{imp}}^0(\omega)^{-1} - G_{\text{imp}}(\omega)^{-1}$. While the non-interacting retarded Green’s function $G_{\text{imp}}^0(\omega) = \frac{1}{\omega - \varepsilon_d - \Delta(\omega)}$ is known exactly, the interacting retarded Green’s function of the impurity model $G_{\text{imp}}(\omega)$ can be calculated with the “impurity solver” NRG and will therefore display numerical errors, depending on the discretization grid and the broadening of the raw data. Yet, taking the difference of an exact and an error-prone quantity can be detrimental to the accuracy of the results, especially when the outcome is in the order of the numerical error. This can happen for a Fermi liquid, where the self-energy approaches zero for $T \rightarrow 0$ close to the Fermi level, since $\text{Im} \Sigma(\omega \rightarrow 0) \sim T^2$. So the numerical calculation is in this case less reliable for the most relevant frequency range. Within DMFT it is possible that these numerical errors even increase due to the iterative procedure.

Therefore we will use a different approach to calculate the self-energy with the NRG “impurity

solver”. In 1998 R. Bulla deduced an alternative expression for the self-energy of the SIAM from an equation of motion ansatz [16]. It can be written as the ratio of two correlation functions,

$$\Sigma(\omega) = \frac{F(\omega)}{G(\omega)}, \quad (4.1)$$

with the on-site correlation function

$$G(\omega) = \langle \hat{d} \| \hat{d}^\dagger \rangle_\omega \quad (4.2)$$

and the two-particle retarded Green’s function

$$F(\omega) = \langle [\hat{d}, \hat{H}_U] \| \hat{d}^\dagger \rangle_\omega. \quad (4.3)$$

Note that the spin index is omitted and $G(\omega) \equiv G_{\text{imp}}(\omega)$. \hat{H}_U is the interaction part of the local impurity Hamiltonian \hat{H}_{imp} . For the SIAM we have $\hat{H}_U = U \hat{d}_\uparrow^\dagger \hat{d}_\uparrow \hat{d}_\downarrow^\dagger \hat{d}_\downarrow$. In Appendix C we show a detailed derivation of the self-energy expression for a general multi-band Anderson model.

Using the FDM-NRG approach we can compute the imaginary parts of the retarded Green’s functions $G(\omega)$ and $F(\omega)$ and get the real parts of the corresponding smoothed spectral functions via a Kramers-Kronig transformation

$$\text{Re } G(\omega) = \frac{1}{\pi} \mathcal{P} \int_{-\infty}^{\infty} dx \frac{\text{Im } G(x)}{x - \omega}. \quad (4.4)$$

The self-energy is then expressed as the ratio of two quantities, that have been obtained numerically on equal footing. This results in a reduction of systematic to only relative errors, that enter the DMFT self consistency loop.

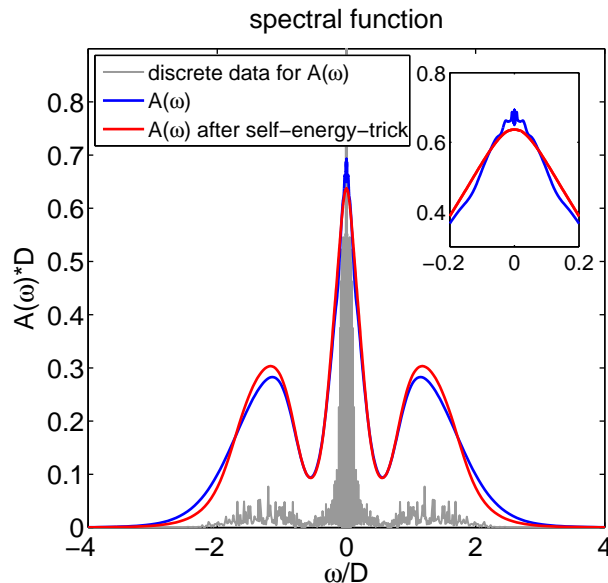


Figure 4.1: Spectral function for the particle-hole symmetric one-band Hubbard model with $U = 2$, $\mu = U/2$, $T = 0$, $N_z = 4$ and $\Lambda = 2$. In grey the raw data is plotted as $\frac{A_{\text{raw}}(\omega) \cdot 8}{|\omega|}$. The blue curve represents the smoothed spectral function $A(\omega)$ with a broadening of $\sigma = 0.2$. The red curve is calculated with the “self-energy-trick” as $A(\omega) = -\frac{1}{\pi} \text{Im } G(\omega)$, where $G(\omega) = \frac{1}{\omega - \varepsilon_d - \Delta(\omega) - \Sigma(\omega)}$ and $\Sigma(\omega) = \frac{F(\omega)}{G(\omega)}$. It can be clearly seen that the artificial oscillations around the Fermi level are removed and high-energy features come into sharper relief.

Artificial oscillations, which arise due to the logarithmic discretization grid, as well as broadening artefacts, like the suppression of high-energy peaks in the local density of states, widely cancel out using Bulla’s self-energy term. This can be viewed in Fig. 4.1.

With R. Bulla’s expression for the self-energy, we can now revise the self-consistency procedure introduced in Chapter 2 (see Fig. 2.5). The first step of a general DMFT iteration is to use the frequency-dependent hybridization function obtained from the preceding iteration as input for the NRG impurity solver. With the impurity Hamiltonian \hat{H}_{imp} known, the hybridization function completely determines the quantum impurity model, that can then be solved with the FDM-NRG approach, yielding the spectral functions for the calculation of the self-energy. The self-energy is the output function of the NRG “impurity solver” and can be employed in the calculation of the new on-site lattice Green’s function and afterwards in the derivation of the input hybridization function for the next iteration.

4.2 The logarithmic discretization grid within DMFT

Until convergence, the DMFT procedure leads, at each DMFT iteration, to a new shape of the frequency-dependent input hybridization function for the NRG impurity solver. So the energy support of the hybridization function changes for every NRG run and is not known a priori. This brings us to the problem how to define the discretization grid for DMFT applications.

As will be shown in the following, the efficiency of the NRG calculations is strongly affected by the specific choice of the discretization scheme. In general, it is difficult to find a suitable grid before the NRG calculation is performed. However, R. Zitko introduced an adaptive discretization method that takes the actual shape of the hybridization function into account [27].

4.2.1 Variation of the conventional logarithmic discretization grid

While for a standard NRG run, the bandwidth can be generally chosen as $[-1, 1]$ the only fixed quantity during the DMFT loop is the non-interacting density of states. Therefore its half bandwidth of D (with D set to 1) is used as energy reference in the following. Note that we assume the semi-elliptic Bethe lattice density of states, where the hybridization function features the same shape as the spectral function (up to a global constant factor).

Then however, the conventional discretization grid has to be expanded over a larger range of energies, as the support of the hybridization function will exceed the non-interacting bandwidth during the DMFT loop due to strong electron-electron interactions. A possible choice is

$$\epsilon_n = \pm \Lambda^{-n}, \quad (4.5)$$

starting with negative $n \leq n_0$. Since we don’t know the energy support of the hybridization function a priori, we have to choose n_0 small enough, to ensure that the whole hybridization function is sampled by the grid (e.g $n = -5, -4, -3, \dots$ with $n_0 = -5$).

This implies the presence of bath states with small couplings γ_n in the so called “star” Hamiltonian of Eq. (3.17) at high representative energies $|\xi_n|$. Further, small couplings γ_n arise for intervals within the charge gap of an isolator or in the metallic phase near the MIT (see Sec. 5). While for a flat band, the (physical) hopping matrix elements t_N fall off exponentially along the Wilson chain, different (even numerically detrimental) behavior may arise for a frequency-dependent hybridization function (with partially small weight).

In the following, we want to study the effect of small couplings in the “star” Hamiltonian on the hopping matrix elements of the Wilson chain. To this end, we have to understand in more detail the Lanczos tridiagonalization algorithm, that transforms the “star” Hamiltonian Eq. (3.17) into the Wilson chain Hamiltonian Eq. (3.21).

Following [33, pp. 185-187], we consider the bath Hamiltonian of Eq. (3.15) in the form

$$\hat{H}_{\text{bath}} = \sum_{n\sigma} \xi_n |n0\sigma\rangle \langle n0\sigma| \quad (4.6)$$

and the normalized state $|f_{0\sigma}\rangle = \hat{f}_{0\sigma}^\dagger | \rangle$ as starting vector for the recursion method. $\hat{f}_{0\sigma}$ is defined in Eq. (3.19) and $| \rangle$ denotes the vacuum state. To simplify notation, we skip the spin index in the following.

In a first step we construct a new state,

$$|\tilde{f}_1\rangle = (1 - P_0)\hat{H}_{\text{bath}}|f_0\rangle = \hat{H}_{\text{bath}}|f_0\rangle - \varepsilon_0|f_0\rangle, \quad (4.7)$$

with $\varepsilon_0 = \langle f_0|\hat{H}_{\text{bath}}|f_0\rangle$, that is orthogonal to $|f_0\rangle$, by applying the operator \hat{H}_{bath} to $|f_0\rangle$ and subtracting its projection on the initial state $P_0 = |f_0\rangle\langle f_0|$. Then we normalize it to

$$|f_1\rangle = \frac{1}{t_0}|\tilde{f}_1\rangle, \quad (4.8)$$

with $t_0^2 = \langle \tilde{f}_1|\tilde{f}_1\rangle$.

In a second step, we calculate the state $|\tilde{f}_2\rangle$ by applying a similar procedure (including the orthogonalization with respect to the preceding states $|f_0\rangle$ and $|f_1\rangle$):

$$|\tilde{f}_2\rangle = (1 - P_1)(1 - P_0)\hat{H}_{\text{bath}}|f_1\rangle = \hat{H}_{\text{bath}}|f_1\rangle - \varepsilon_1|f_1\rangle - t_0|f_0\rangle, \quad (4.9)$$

where $\varepsilon_1 = \langle f_1|\hat{H}_{\text{bath}}|f_1\rangle$ and $P_1 = |f_1\rangle\langle f_1|$. The normalized state reads

$$|f_2\rangle = \frac{1}{t_1}|\tilde{f}_2\rangle, \quad (4.10)$$

with $t_1^2 = \langle \tilde{f}_2|\tilde{f}_2\rangle$.

A general step from N to $N + 1$ then yields a three term relation,

$$|f_{N+1}\rangle = \frac{1}{t_N}(1 - P_N)(1 - P_{N-1})\dots(1 - P_0)\hat{H}_{\text{bath}}|f_N\rangle \quad (4.11a)$$

$$= \frac{1}{t_N}\left(\hat{H}_{\text{bath}}|f_N\rangle - \varepsilon_N|f_N\rangle - t_{N-1}|f_{N-1}\rangle\right), \quad (4.11b)$$

with $P_N = |f_N\rangle\langle f_N|$, $t_N^2 = \langle \tilde{f}_{N+1}|\tilde{f}_{N+1}\rangle$ and $\varepsilon_N = \langle f_N|\hat{H}_{\text{bath}}|f_N\rangle$, since $P_{N'}\hat{H}_{\text{bath}}|f_N\rangle \equiv 0$ for $N' < N - 1$. By solving the above relation for \hat{H}_{bath} , we obtain a one-dimensional chain representation for the bath Hamiltonian as in Eq. (3.21):

$$\hat{H}_{\text{bath}} = \sum_N [\varepsilon_N |f_N\rangle\langle f_N| + t_N(|f_N\rangle\langle f_{N+1}| + \text{h.c.})]. \quad (4.12)$$

The corresponding unitary transformation from the bath Hamiltonian Eq. (4.6) to Eq. (4.12) can be written in terms of the states $|f_N\rangle$ as $U = (|f_0\rangle, |f_1\rangle, \dots)$.

We now define a simplified setting to study the role of small couplings in the “star” Hamiltonian within the tridiagonalization procedure. We assume a constant hybridization $\Gamma = 1$ on the energy

support $[-1, 1]$ and the conventional NRG discretization procedure that was described in Sec. 3.1.2. To simulate small weights of the hybridization function, we replace the original couplings $\gamma_x \sim \Lambda^{-\frac{x}{2}}$ in the intervals I_x at (positive and negative) representative energies $\xi_x \sim \pm \Lambda^{-x} \ll 1$ by much smaller values $\gamma_x \ll \sqrt{\xi_x} \ll 1$. The normalized and symmetric initial state $|f_0\rangle$ then exhibits a component $u_x^{(0)} \sim \gamma_x$ (up to normalization) with respect to the introduced small coupled level (at positive and negative representative energy ξ_x , respectively), to which we refer as “x-component” from now on. To obtain $|f_1\rangle$ we multiply $|f_0\rangle$ with \hat{H}_{bath} , which is diagonal in matrix representation. By symmetry (with respect to positive and negative energies), $\hat{H}_{\text{bath}}|f_0\rangle$ is already orthogonal to $|f_0\rangle$. Thus the “x-component” of $|f_1\rangle$ reads

$$u_x^{(1)} \sim \frac{\xi_x}{t_0} u_x^{(0)} \ll u_x^{(0)}, \quad (4.13)$$

with the normalization constant t_0 as in Eq. (3.22). The “x-component” of the second state is essentially given by the “x-component” of the initial state $|f_0\rangle$, since it can be expressed as

$$u_x^{(2)} = \frac{1}{t_1} (\xi_x u_x^{(1)} - t_0 u_x^{(0)}) \sim \frac{t_0}{t_1} u_x^{(0)} \quad (4.14)$$

according to Eq. (4.11b) with $N = 2$. This implies that the “x-component” of the third state,

$$u_x^{(3)} = \frac{1}{t_2} (\xi_x u_x^{(2)} - t_1 u_x^{(1)}) \sim \left(\frac{t_0^2}{t_2 t_1} - \frac{t_1}{t_2} \right) u_x^{(1)}, \quad (4.15)$$

is comparable in magnitude to $u_x^{(1)}$. From Eq. (4.11b) we deduce a general relation for the “x-component” of state N :

$$u_x^{(N+1)} = \frac{1}{t_N} (\xi_x u_x^{(N)} - t_{N-1} u_x^{(N-1)}). \quad (4.16)$$

So we essentially obtain the following even-odd behavior as long as $\xi_x/t_N \ll 1$:

$$u_x^{(N+1)} \sim \begin{cases} \frac{t_{N-1}}{t_N} u_x^{(N-1)} & N \gg 1 \\ \frac{t_{N-2}}{t_N} \frac{t_{N-2}}{t_{N-1}} u_x^{(N-1)} & N \gg 1 \end{cases} \begin{cases} \sqrt{\Lambda} u_x^{(N-1)} & \text{for } N+1 \text{ even} \\ \Lambda^{\frac{3}{2}} u_x^{(N-1)} & \text{for } N+1 \text{ odd} \end{cases} \quad (4.17)$$

Iterating $u_x^{(N)}$ then leads to

$$u_x^{(N+1)} \stackrel{N \gg 1}{\sim} \begin{cases} \Lambda^{\frac{N}{4}} u_x^{(0)} & \text{for } N+1 \text{ even} \\ \Lambda^{\frac{3N}{4}} u_x^{(1)} & \text{for } N+1 \text{ odd} \end{cases} \quad (4.18)$$

While the “x-components” start at $u_x^{(0)}$ for even iterations, they begin at lower values $u_x^{(1)} \ll u_x^{(0)}$ for odd iterations. As soon as $u_x^{(N_{\text{even}})}$ and $u_x^{(N_{\text{odd}})}$ become comparable at iteration N_{ξ_x} , the even-odd behavior stops. N_{ξ_x} can be obtained from the ansatz

$$\Lambda^{\frac{N_{\xi_x}}{4}} u_x^{(0)} \approx \Lambda^{\frac{3N_{\xi_x}}{4}} u_x^{(1)}, \quad (4.19)$$

with Eq. (4.13), resulting in the condition $\xi_x \approx t_{N_{\xi_x}}$, where $t_N \stackrel{N \gg 1}{\approx} \Lambda^{-\frac{N+1}{2}}$, or equivalently

$$N_{\xi_x} \approx -2 \cdot \frac{\ln \xi_x}{\ln \Lambda} - 1. \quad (4.20)$$

N_{ξ_x} thus corresponds approximately to the Wilson chain site whose energy scale is equal to ξ_x . For $N > N_{\xi_x}$ (or analogously $\xi_x > t_N$) different behavior can be observed. Now the second term of Eq. (4.16), that scales like $t_{N-1}/t_N = \sqrt{\Lambda}$, can be ignored compared to the first part, which contains the factor

$$\frac{\xi_x}{t_N} \approx \frac{t_{N_{\xi_x}}}{t_N} \approx \Lambda^{\frac{N-N_{\xi_x}}{2}}. \quad (4.21)$$

So the “x-component” grows exponentially for $N > N_{\xi_x}$:

$$u_x^{(N+1)} \sim \Lambda^{\frac{N-N_{\xi_x}}{2}} u_x^{(N)}. \quad (4.22)$$

Starting from $\Lambda^{\frac{N-N_{\xi_x}}{2}}$ we arrive at the expression

$$u_x^{(N)} \sim u_x^{(N_{\xi_x})} \prod_{N'=N_{\xi_x}}^N \Lambda^{\frac{N'-N_{\xi_x}}{2}} \sim u_x^{(N_{\xi_x})} \Lambda^{\frac{1}{4}(N-N_{\xi_x})^2} \quad (4.23)$$

for even and odd Wilson chain sites N , since

$$\sum_{N'=N_{\xi_x}}^N \frac{N'-N_{\xi_x}}{2} = \frac{1}{2} \sum_{N'=0}^{N-N_{\xi_x}} N' = \frac{1}{4} (N-N_{\xi_x})(N-N_{\xi_x}-1) \approx \frac{1}{4} (N-N_{\xi_x})^2. \quad (4.24)$$

The behavior of $u_x^{(N)}$ is depicted in Fig. 4.2 (upper panel), where we have chosen two different small values γ_x in the intervals I_x with corresponding representative energies $\xi_x = \pm 1.46 \cdot 10^{-3}$.

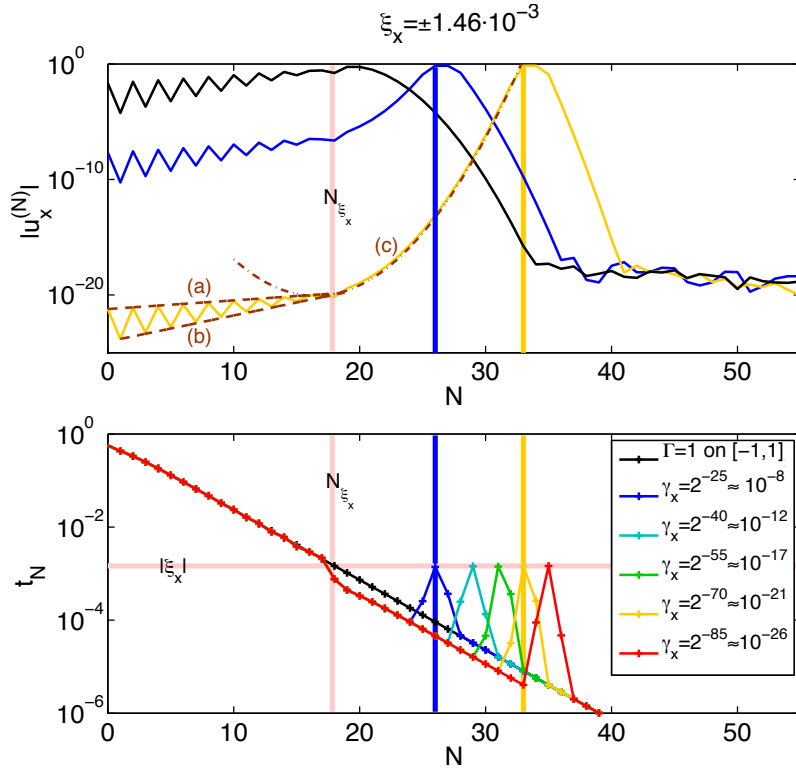


Figure 4.2: The black curves in the upper and lower panel show the “x-components” $u_x^{(N)}$ and the hopping matrix elements t_N for a constant hybridization function $\Gamma = 1$ on an energy support $[-1,1]$ ($D = 1$), respectively. We use the conventional discretization grid with $\Lambda = 2$ and $z = 0$. For the colored curves the hybridization was set to different low values in intervals with representative energies $\xi_x = \pm 1.46 \cdot 10^{-3}$. The brown fit curves, denoted by (a), (b) and (c), correspond to the relations Eq. (4.18) and Eq. (4.23).

For the yellow curve, we explicitly show that the scaling laws Eq. (4.18) (fit (a) for even and fit (b) for odd in Fig. 4.2 (upper panel)) and Eq. (4.23) (fit (c)) apply. For a flat band, a coupling $\gamma_x \sim \sqrt{\xi_x}$ essentially leads to a hopping matrix element of height ξ_x at site N_{ξ_x} , where $\xi_x \approx t_{N_{\xi_x}}$ (see black curve in Fig. 4.2 (lower panel)). Here the second domain of $u_x^{(N)}$, which is characterized by Eq. (4.23), does not emerge, as can be reviewed in Fig. 4.2 (upper panel) for the black curve. For small couplings $\gamma_x \ll \sqrt{\xi_x} \ll 1$ the hopping matrix element of height ξ_x is obtained at a later site N_P , which is determined by the condition $u_x^{(N_P)} \approx 1$ in Eq. (4.23), leading to

$$N_P \approx 2\sqrt{-\frac{\ln \gamma_x}{\ln \Lambda}} + \text{const.} \quad (4.25)$$

Thus a peak arises in the Wilson chain couplings at site N_P . This is depicted in Fig. 4.2 (lower panel), where we have plotted the hopping matrix elements for different small couplings γ_x in the intervals I_x with energies $\xi_x = \pm 1.46 \cdot 10^{-3}$. The onset N_{ξ_x} and the height of the peaks is determined by the absolute value of the representative energies ξ_x (red bars in Fig. 4.2). The additional shift of the peaks is proportional to the square root of the chain site, representing the energy scale of the corresponding coupling γ_x . Naively one might have expected a linear relation between N_P and γ_x . However the superexponential behavior for $u_x^{(N)}$ in Eq. (4.23) results in a square root relation $N_P \sim \sqrt{\gamma_x}$. In Fig. 4.3 we plot N_P versus $x_P \equiv \sqrt{-\ln \gamma_x / \ln \Lambda}$ and can explicitly confirm Eq. (4.25).

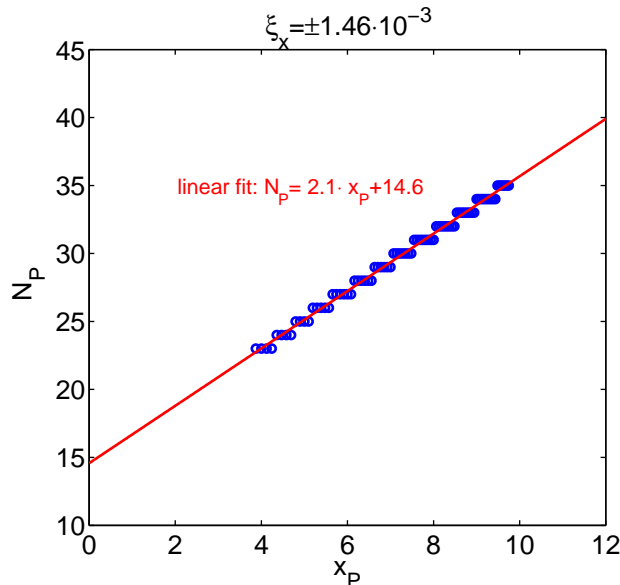


Figure 4.3: The hybridization $\Gamma = 1$ on an energy support $[-1,1]$ is set to different low values in the intervals with representative energies $\xi_x = \pm 1.46 \cdot 10^{-3}$. We plot the peak positions N_p for the corresponding small values of the coupling γ_x (blue circles) and find a linear dependence between N_p and $x_P \equiv \sqrt{-\ln \gamma_x / \ln \Lambda}$ (red fit) with a slope of roughly 2.

Within DMFT we might have to deal with small couplings γ_x in the outermost intervals. So we now set the weight of the hybridization Γ to small values for the intervals I_x with representative energies $\xi_x = \pm 0.75$. For this case the first domain of $u_x^{(N)}$, which is determined by Eq. (4.18), is missing, as immediately $N > N_{\xi_x}$ applies. Thus the peaks emerge already within the first

20 sites of the chain, even for the merest coupling $\gamma_x \approx 10^{-26}$ (see Fig. 4.4). Due to the little weight of the hybridization function in the outermost intervals $\pm[1, 1/2]$ (colored curves), the bandwidth effectively reduces to the energy support $[-1/2, 1/2]$. Therewith, it is advisable to stop the discretization already at $\pm 1/2$, which leads to hopping matrix elements (black curve), that does not feature any peak and fall off faster.

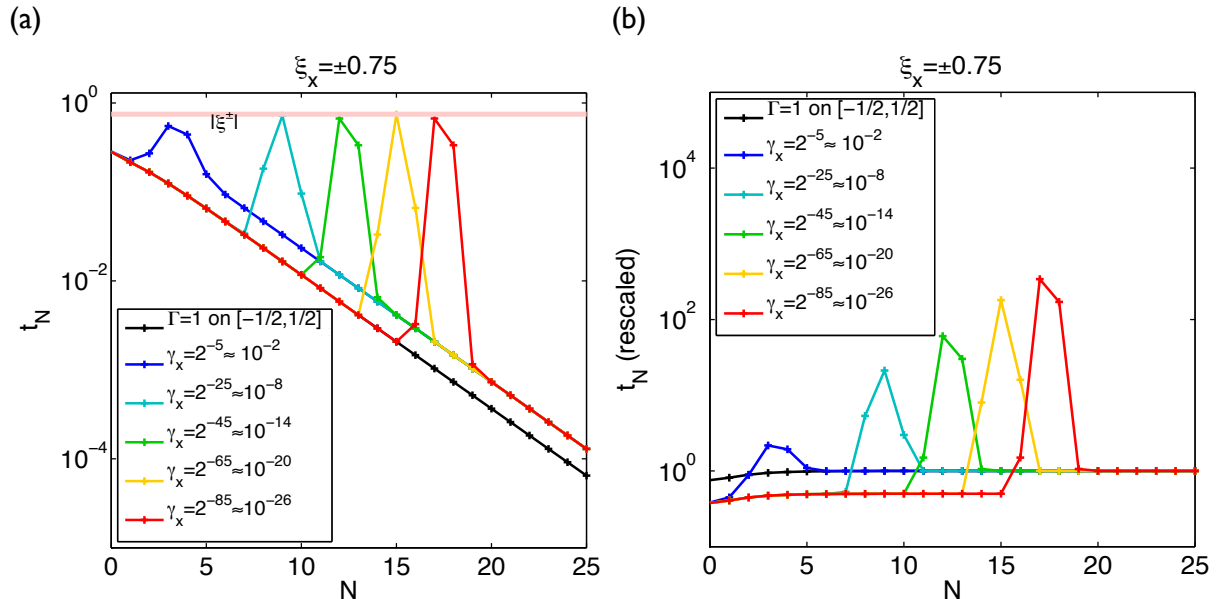


Figure 4.4: We consider a constant hybridization function $\Gamma = 1$ on an energy support $[-1, 1]$ using the conventional discretization grid (where D is set to 1) with $\Lambda = 2$ and $z = 0$. For the colored curves the hybridization was set to different low (partially effectively zero) values in the outermost intervals with representative energies $\xi_x = \pm 0.75$. The black curve illustrates the hopping matrix elements for a reduced energy support $[-1/2, 1/2]$. Panel (b) depicts the corresponding rescaled Wilson chain couplings.

The bottom line of this study is that the full numerical bandwidth should not be chosen arbitrarily large. Especially outer intervals with high absolute values for the representative energies ξ_x and relatively small couplings γ_x lead to peaks in the hopping matrix elements at the beginning of the Wilson chain, roughly around the site N_0 where truncation should set in. However the basic NRG assumption of energy scale separation is then not guaranteed in this region and truncation should be postponed until the hopping matrix elements fall off again. Thus much more states have to be kept to achieve accurate results. For more complex systems, like two-band models, calculations can become so expensive that they are hardly feasible. Note however that peaks at later Wilson chain sites are less problematic, since truncation can be performed before the peak arises. At sites where the Wilson chain couplings increase, we then may keep all states and truncate again afterwards.

To avoid small couplings in the “star” Hamiltonian, it is advisable to introduce a slightly altered discretization grid (which will be used throughout this thesis). This grid has a fixed outer interval border,

$$\epsilon_0 \approx 100, \quad (4.26a)$$

that is large enough to include all the high-energy weight of the hybridization function. The first interval border (determined by $n_1 \in \mathbb{Z}_0$) is then chosen such that the coupling strength

γ_0 in the outermost interval is maximally one order smaller than the square root of the overall hybridization:

$$\epsilon_1 = \Lambda^{-(n_1+z)}. \quad (4.26b)$$

The remaining intervals follow the conventional logarithmic discretization scheme

$$\epsilon_n = \Lambda^{-(n+z)} \quad n = n_1 + 1, n_1 + 2, \dots \quad (4.26c)$$

Note that $D = 1$ and n_1 can be negative. To motivate this altered discretization grid, we plot the Wilson chain couplings for the spectral function of a specific DMFT calculation (black curve in Fig. 4.6) for different choices of n_1 . The spectral function corresponds to the asymmetric one-band Hubbard model for $U/D = 4$, $\mu/D = 0.5068$ and $T/D = 0.0025$ (see Sec. 5.3). As the DMFT calculation is performed for an infinite-dimensional Bethe lattice the hybridization has (up to an overall constant factor) exactly the same form as the spectral function.

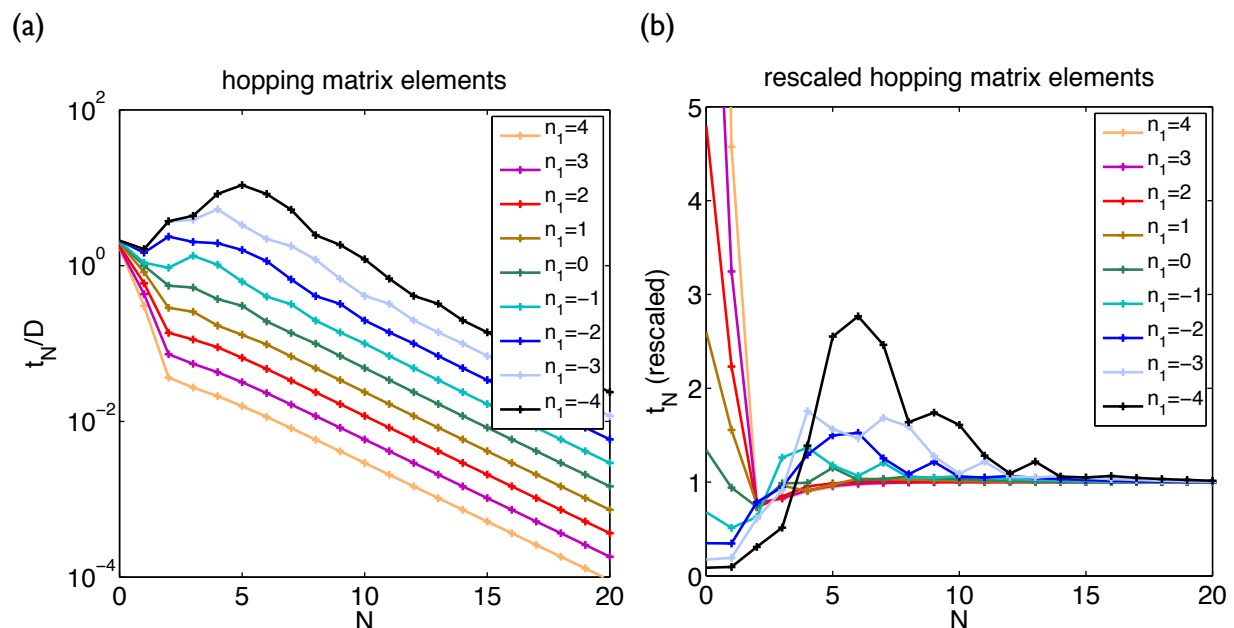


Figure 4.5: Panel (a) shows the hopping matrix elements for the spectral function of Fig. 4.6 for different widths of the two outermost intervals, which are determined by the interval borders $\pm\epsilon_1 = \pm\Lambda^{-(n_1)}$ with $z = 0$ and $\Lambda = 2$. Panel (b) depicts the corresponding rescaled Wilson chain couplings.

For the black curve the first interval border is chosen as $\epsilon_1 = 2^{-(-4)} = 16$, then $\epsilon_2 = 8$. So we get about five intervals with weak coupling γ (compared to the square root of the overall hybridization). In the case of $n_1 = -3$ this reduces to about only three intervals, while we have no outer interval with small couplings for $n_1 = 0$. As shown before, the weak coupled intervals lead to growing hopping matrix elements in the Wilson chain. This is quite extreme for the case of $n_1 = -4$ where the outermost intervals lead to an increase of the Wilson chain couplings for the first few sites and the inner weak coupled intervals ensure that this behavior is retained until site $N = 5$. So truncation is not justified for about 6 NRG iterations. For $n_1 = 0$ the couplings of the outer intervals contain more spectral weight and the hopping matrix elements show a smooth decay, as expected. Correspondingly, the convergence of the rescaled hopping matrix elements to 1 (shown in Fig. 4.5 (b)) is achieved for much earlier sites.

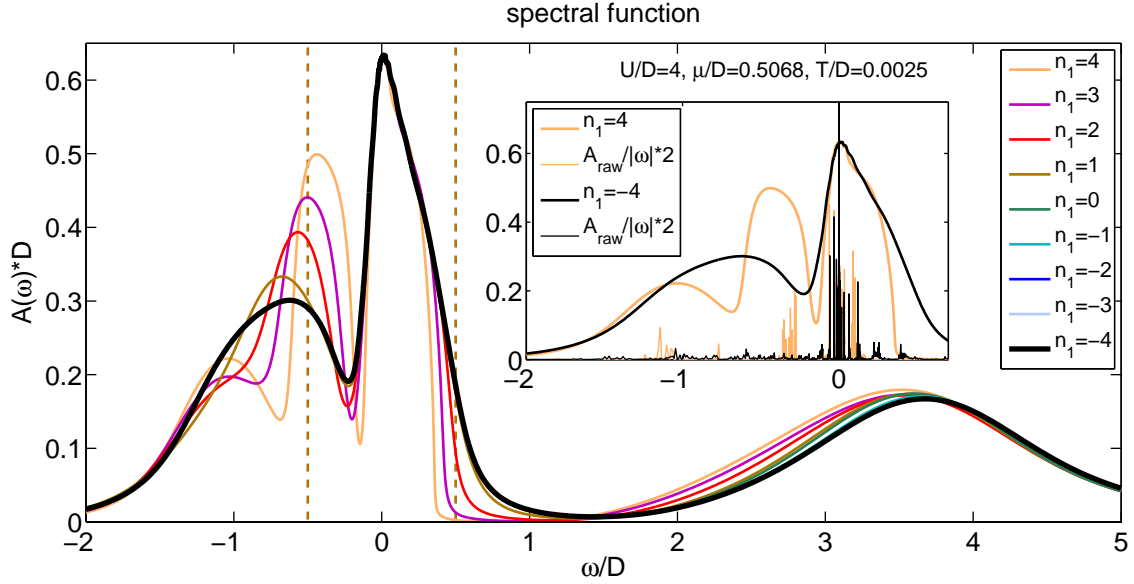


Figure 4.6: Spectral function for the asymmetric one-band Hubbard model for $U/D = 4$, $\mu/D = 0.5068$ and $T/D = 0.0025$, calculated with DMFT and NRG ($\Lambda = 2$, $N_{\text{max}} = 35$ and $N_z = 1$) using different discretization grids. To find a good choice for the width of the outermost two intervals, determined by the interval borders $\pm\epsilon_1 = \pm\Lambda^{-(n_1+z)}$, different values of n_1 are tested. While the grids $n_1 = -4$ to $n_1 = 0$ yield the same spectral function, grids with too broad outer intervals $n_1 = 1$ to $n_1 = 4$ result in less accurate functions. In the inset, the accurate spectral function (black curve) and the outcome for $n_1 = 4$ (orange curve) are plotted together with the corresponding raw data to demonstrate the origin of the wavy feature in the deviating spectral functions.

A natural question that arises at this stage is, how large can the outermost interval be chosen? As depicted in Fig. 4.5 an even broader interval ($n_1 > 0$) results in faster decaying Wilson chain couplings. However, the first interval borders then lie in the region of the quasiparticle peak (as shown for the case $n_1 = 1$ by the dashed brown vertical lines in Fig. 4.6) and the grid does no longer allow a proper resolution of the transition between the so called Hubbard bands and the quasiparticle peak at the Fermi level (read Chapter 5 for an explanation of the characteristic form of the local spectral function for the Hubbard model). This situation is presented in Fig. 4.6. While the grids for $n_1 = -4$ to $n_1 = 0$ essentially yield the same spectral function (even so the efficiencies of the calculations differ quite strongly), a too large outer interval, that cuts into the quasiparticle peak, leads to deviations from the expected spectral function. In principle, one could properly adapt the broadening procedure to an enlarged outer interval (in order to smooth the wavy features of the deviating spectral functions), however at some point too much information is lost by a too coarse grid and also the accuracy of the quasiparticle peak is affected. This can also be checked by plotting the filling factor $\langle N \rangle$ of the spectral function (see Eq. (5.2)) for the different grids, specified by n_1 (see Fig. 4.7). Clearly $\langle N \rangle$ starts to deviate from a stable value for about $n_1 \leq 1$.

Altogether the altered grid as suggested in Eq. (4.26) with properly chosen n_1 constitutes a reasonable compromise between computational effort and required accuracy. Nevertheless it is based on heuristic arguments. The resolution of the spectral function can be improved by averaging over different discretization meshes. Note that z -averaging is performed such that the outermost intervals increase with $z > 0$ which is different to the standard scheme presented in Eq. (3.18). Yet this procedure does not recover the true continuum limit.

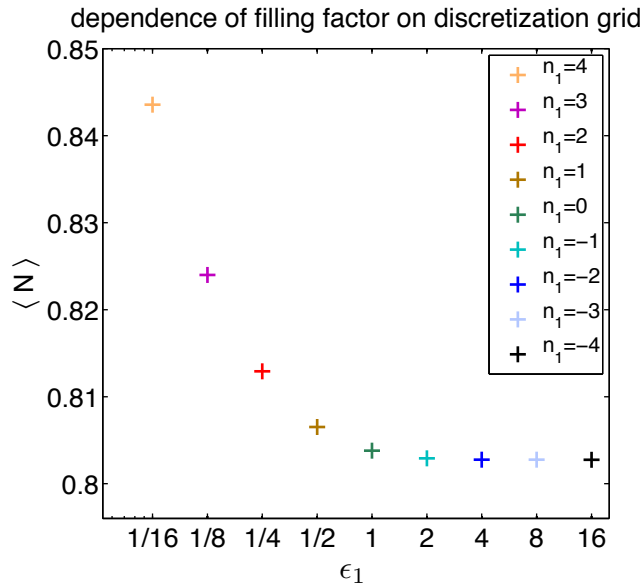


Figure 4.7: Filling factors $\langle N \rangle$ of the spectral functions shown in Fig. 4.6, which are calculated for different discretization grids determined by the interval borders $\pm\epsilon_1 = \pm\Lambda^{-n_1}$.

4.2.2 Zitko's adaptive logarithmic discretization grid

In 2009 R. Zitko proposed an adaptive discretization method that takes the shape of the hybridization function into account and is additionally based on the requirement to reproduce the input hybridization function after z -averaging [27].

The logarithmic discretization scheme incorporates the actual form of the hybridization function in a way that it is denser in regions with more weight and shows broader intervals, when the function is very low, thus avoiding intervals with weak coupling and consequently unsolicited peaks in the hopping matrix elements. Moreover, the couplings and representative energies of the star Hamiltonian are calculated by solving differential equations, that ensure that z -averaging generates the original hybridization function. In the following, we want to derive these differential equations to determine the adaptive grid and the corresponding representative energies and couplings (focusing on positive frequencies for convenience).

To this end, we define a general logarithmic discretization grid with mesh points as in [27]:

$$\epsilon_1^z = 1, \quad (4.27a)$$

$$\epsilon_n^z > \epsilon_{n+1}^z, \quad (4.27b)$$

$$\epsilon_n^z \sim \Lambda^{-(n+z)} \xrightarrow{n \rightarrow \infty} 0, \quad (4.27c)$$

$$z \in [0, 1], \quad (4.27d)$$

with the continuity constraint

$$\epsilon_n^1 = \epsilon_{n+1}^0 \quad (4.27e)$$

for all n . The representative energies of the intervals (now denoted by E_n) then follow the same asymptotic behavior

$$E_n \sim \Lambda^{-(n+z)}. \quad (4.28a)$$

Furthermore, the boundary condition

$$E_1^0 = 1 \quad (4.28b)$$

and the continuity constraint

$$E_n^1 = E_{n+1}^0 \quad (4.28c)$$

have to be fulfilled for a meaningful z-averaging procedure [27]. For every logarithmic discretization mesh, the continuous density of states of the conduction band as seen by the impurity,

$$A_0(\omega) = -\frac{1}{\pi} \text{Im} \langle \hat{f}_0 \| \hat{f}_0^\dagger \rangle_\omega = \frac{\Gamma(\omega)}{\pi} / \xi_0, \quad (4.29)$$

with the spin index omitted and the normalization as in Eq. (3.20)

$$\xi_0 = \int_{-1}^1 d\varepsilon \frac{\Gamma(\omega)}{\pi}, \quad (4.30)$$

is then given by a set of δ -peaks,

$$\tilde{A}_0(z, \omega) = \sum_n w_n^z \delta(\omega - E_n^z), \quad (4.31)$$

with normalized weights for all z :

$$\sum_{n=1}^{\infty} w_n^z = \frac{1}{2} = \int_0^{\infty} A_0(\omega) d\omega. \quad (4.32)$$

We now claim that the spectral density A_0 is reproduced by taking the average (integral) over z :

$$A_0(\omega) = \int_0^1 \tilde{A}_0(z, \omega) dz. \quad (4.33)$$

This can be rewritten in the following form

$$A_0(\omega) = \sum_n \int_0^1 w_n^z \delta(\omega - E_n^z) dz = \frac{w_n^z}{-\partial E_n^z / \partial z}, \quad (4.34)$$

where n and z are determined implicitly by $\omega = E_n^z$. As E_n^z is a strictly decreasing function of z , this choice is unique.

We now introduce a continuous “grid parameter”,

$$x = n + z, \quad x \in [1; +\infty) \quad (4.35)$$

and accordingly continuous functions $\epsilon(x)$, $E(x)$ and $w(x)$, that automatically fulfill the continuity constraints given above. $\epsilon(x)$ and $E(x)$ are monotonically decreasing functions that have to satisfy the boundary conditions

$$\epsilon(x) = 1 \quad \text{for } x \leq 2 \quad \text{and} \quad \lim_{x \rightarrow \infty} \epsilon(x) = 0, \quad (4.36)$$

$$E(1) = 1 \quad \text{and} \quad \lim_{x \rightarrow \infty} E(x) = 0. \quad (4.37)$$

Eq. (4.34) then reads

$$A_0(\omega) = \frac{w(x)}{-dE(x)/dx} \quad (4.38)$$

with $x = R(\omega)$ and the inverse function $R[E(x)] = x$. The normalization condition still holds for the continuous version

$$\sum_{n=1}^{\infty} w(n+z) = \frac{1}{2} = \int_0^1 A_0(\omega) d\omega = \int_{-\infty}^1 A_0(\omega) \frac{dE(x)}{dx} dx = \int_1^{\infty} w(x) dx \quad (4.39)$$

and can be used to reformulate $w(x)$:

$$\sum_{n=1}^{\infty} w(n+z) = \int_0^1 A_0(\omega) d\omega = \sum_{n=1}^{\infty} \int_{\epsilon(x+1)}^{\epsilon(x)} A_0(\omega) d\omega \quad (4.40)$$

$$\Rightarrow w(x) = \int_{\epsilon(x+1)}^{\epsilon(x)} A_0(\omega) d\omega. \quad (4.41)$$

So, we arrive at the following differential equation for the calculation of the representative energies $E(x)$

$$\frac{dE(x)}{dx} = -\frac{\int_{\epsilon(x+1)}^{\epsilon(x)} A_0(\omega) d\omega}{A_0[E(x)]} \quad (4.42)$$

with the initial condition $E(1) = 1$.

Up to this point, the logarithmic discretization grid has not been determined yet. Thereby, we are free to adapt the exact location of the mesh points as long as the asymptotic behavior $\epsilon(x) \sim \Lambda^{2-x}$ holds. (The additional factor Λ^2 is introduced for convenience.) This is equivalent to demand that

$$\frac{dE(x)}{dx} = -\Lambda^{2-x} \ln \Lambda C(x, \epsilon) \quad (4.43)$$

with the arbitrary, but strictly positive function $C(x, \epsilon)$ with non-zero limit

$$\lambda = \lim_{\substack{x \rightarrow \infty \\ \epsilon \rightarrow 0}} C(x, \epsilon). \quad (4.44)$$

For $C(x, \epsilon) = 1$ this yields the conventional discretization scheme as given in Eq. (3.18). However, motivated by previous considerations, the present goal is to define an adaptive grid that is less dense in regions of weak hybridization. To this purpose, we define

$$C(x, \epsilon) = \frac{F(x)}{A_0(\epsilon)} \quad (4.45)$$

and consider the special case of $F(x) \equiv F$ as in [27]. Then F must be chosen as $F = \int_0^1 A_0(\omega) d\omega = 1/2$, such that the conventional discretization grid is recovered for a flat band with $A_0(\omega) = 1/2$. Due to the $1/A_0(\epsilon)$ dependence, $C(x, \epsilon)$ diverges for $A_0(\epsilon) \rightarrow 0$ and the corresponding energy regions will not contain any discretization mesh points, as desired.

All in all, we can use Eq. (4.42) and Eq. (4.43) together with a convenient ansatz for an adaptive logarithmic grid and the corresponding representative energies,

$$\epsilon(x) = g(x) \Lambda^{2-x}, \quad (4.46)$$

$$E(x) = f(x) \Lambda^{2-x}, \quad (4.47)$$

and arrive at the following differential equations for the functions $g(x)$ and $f(x)$:

$$\frac{dg(x)}{dx} = \ln \Lambda \left[g(x) - C(x, g(x)\Lambda^{2-x}) \right], \quad (4.48)$$

$$\frac{df(x)}{dx} = \ln \Lambda - \frac{\int_{g(x+1)\Lambda^{1-x}}^{g(x)\Lambda^{2-x}} A_0(\omega) d\omega}{\Lambda^{2-x} A_0[f(x)\Lambda^{2-x}]}, \quad (4.49)$$

with initial conditions $g(2) = 1$ and $f(1) = \frac{1}{\Lambda}$. First Eq. (4.48) is solved and then used for Eq. (4.49).

In [27] R. Zitko gives a short introduction to the implementation of the discretization equation solver, that he provides on his webpage <http://nrgljubljana.ijs.si/adapt>. The couplings of the star Hamiltonian are then calculated as usual with Eq. (3.12) as the square root of the integrated weights in the different intervals.

To visualize the effect of Zitko's adaptive discretization scheme, we use his solver for the same spectral function as in Fig. 4.6.

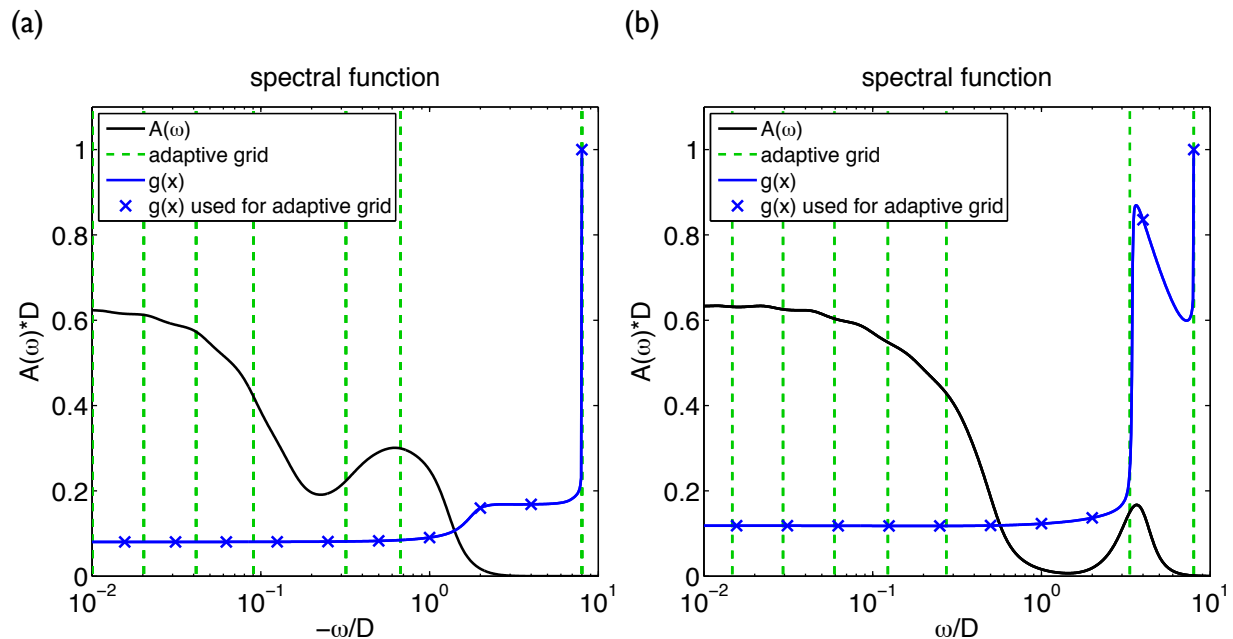


Figure 4.8: Panel (a) shows the negative frequency part of the spectral function (black curve) for the asymmetric one-band Hubbard model with parameters $U/D = 4$, $\mu/D = 0.5068$ and $T/D = 0.0025$, panel (b) the positive frequency range. In order to observe the effect of R. Zitko's adaptive discretization scheme, the frequency axis is plotted logarithmically. The adaptive interval borders are shown by the dashed green vertical lines. The blue crosses on the blue curve give the values of $g(x)$, which have been used to obtain the adaptive mesh points. Further, they indicate the positions of the conventional discretization intervals.

In Fig. 4.8 this spectral function for the asymmetric one-band Hubbard model with parameters $U/D = 4$, $\mu/D = 0.5068$ and $T/D = 0.0025$ (black curves) and the corresponding adaptive grid for $z = 0$ (dashed green lines) are plotted for positive and negative frequencies, respectively. It can be clearly seen that for smaller spectral weight the intervals are enlarged. This is particularly visible for the first interval in panel (a) and the second interval in panel (b) of Fig.

4.8. The corresponding function $g(x)$ is plotted in blue. It has to be noticed that the energy support, used in Zitko's derivation, has to be rescaled to energies larger than 1 in order to be consistent with the DMFT choice of $D = 1$ for the non-interacting lattice density of states of width $2D$. The blue crosses indicate the position of the original grid on the frequency axis and determine the values for $g(x)$ on the vertical axis.

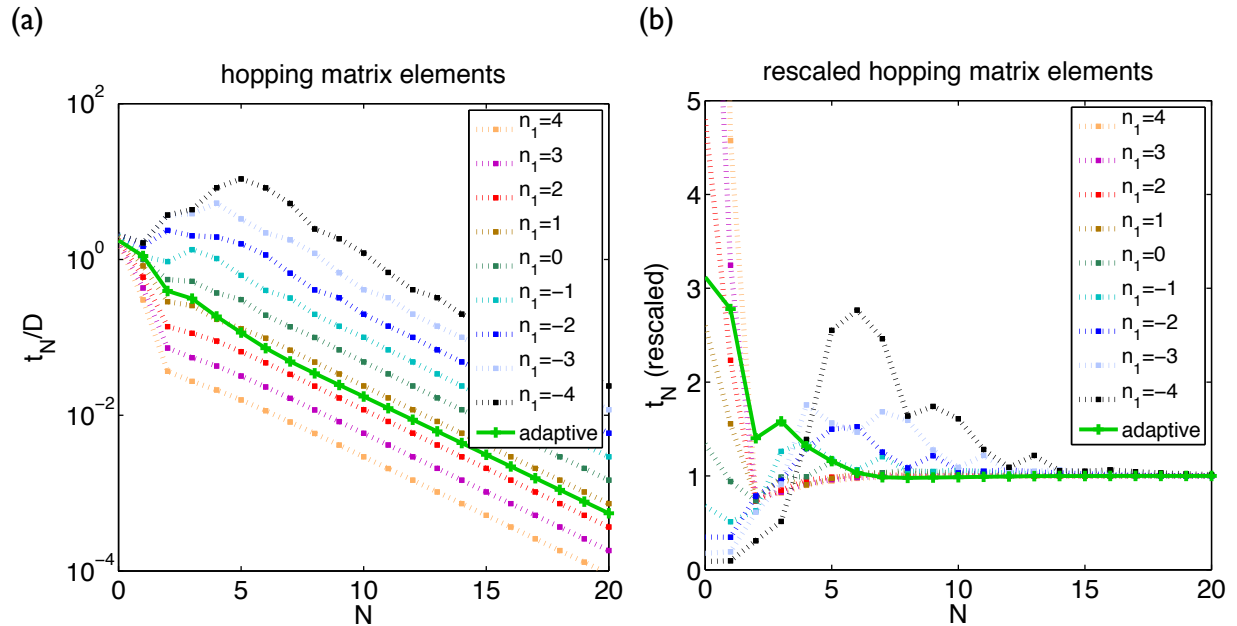


Figure 4.9: Hopping matrix elements calculated with R. Zitko's differential equation solver. In panel (a) the Wilson chain couplings of the adaptive grid are shown by the thick green curve, the rescaled version of the hopping matrix elements is found in panel (b) (thick green curve). The dotted colored curves show the couplings of Fig. 4.5 which are obtained via the discretization scheme presented in the previous section.

As requested, the corresponding hopping matrix elements fall off along the Wilson chain (green thick curve in Fig. 4.9 (a)). They decrease even faster than the couplings for the adequate choice $n_1 = 0$ of the discretization scheme, presented in the previous section. Analogously we find rescaled Wilson chain couplings (green thick curve in Fig. 4.9 (b)), where the peaks are shifted to much earlier sites compared to the cases $n_1 = -4$ to $n_1 = 0$ (dotted green, blue and black colored curves).

To obtain the smoothed spectral function in the case of an adaptive grid, the width of the broadening kernel should take the mesh density into consideration, since less discrete data is produced in energy regions with low spectral weight. In [27] the benefits of the adaptive grid are studied by direct comparison of a test input function A_0 with the NRG output of the same quantity. It is clearly shown that discretization artefacts can be drastically reduced (for this specific case). Nevertheless some open questions remain with regard to the adaptive grid. A major issue is that there exists no clear preference how to incorporate the mesh density in the width of the broadening kernel. As R. Zitko's discretization scheme has been considered towards the end of the master's term this problem remains to be studied in the future.

Chapter 5

One-band Hubbard model

For a first quality check of our DMFT program with the NRG “impurity solver”, we want to investigate the one-band Hubbard model which was already introduced in Sec. 2.2.1. It is the most basic model, that is able to describe the fundamental physics of strongly correlated materials:

$$\hat{H} = -\mu \sum_{i\sigma} \hat{n}_{i\sigma} + \sum_{\langle ij \rangle \sigma} t \hat{c}_{i\sigma}^\dagger \hat{c}_{j\sigma} + U \sum_i \hat{n}_{i\uparrow} \hat{n}_{i\downarrow}. \quad (5.1)$$

The kinetic energy is characterized by the hopping amplitude t and the interaction is given by the local Coulomb repulsion U . μ is the chemical potential of the lattice.

A general illustration of the one-band Hubbard model is given in Fig. 5.1.

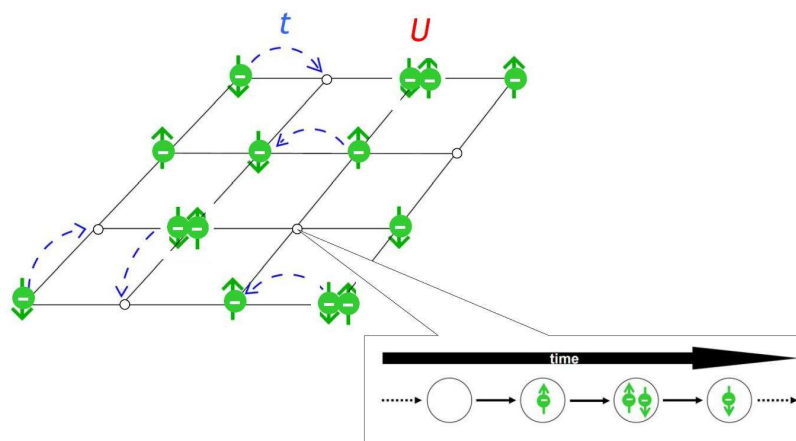


Figure 5.1: Sketch of the one-band Hubbard model. The strongly-correlated material is depicted as a cubic, two-dimensional lattice. Conduction electrons with spin up or down can hop between localized states (orbitals) at lattice sites i and j with an amplitude t . When two electrons meet on one site, they interact via the Coulomb repulsion U . The time sequence indicates quantum mechanical fluctuations in the occupation for one lattice site: either it is unoccupied, singly occupied (with an electron of spin up or down) or doubly occupied. The interplay of hopping and repulsion can lead to interesting many-body phenomena like the “Mott-Hubbard metal-insulator transition”. Figure taken from [10, Chapter 1].

The conduction electrons with spin $\sigma = \uparrow, \downarrow$ can hop between localized states (orbitals) at lattice sites i and j with an amplitude t . Thus, fluctuations in the occupation of the lattice sites arise as depicted by the time sequence in Fig. 5.1. In principle, a site can be unoccupied, singly occupied with electrons of spin up or down, respectively, or doubly occupied with electrons of spin up and down (due to Pauli's exclusion principle). When two electrons sit on the same site, they experience a repulsion of strength U . So a competition between kinetic and local interaction part of the Hamiltonian emerges. While the kinetic energy favors the electrons to move, leading to doubly occupied sites, the Coulomb interaction penalizes double occupation by an energy cost of U . Therefore the overall electron movement is highly correlated and determined by the ratio U/t . But also the filling factor $\langle N \rangle$ of the lattice plays a major role. It is given by the number of electrons N_e divided by the number of lattice sites N_l :

$$\langle N \rangle = \frac{N_e}{N_l}. \quad (5.2)$$

Two simple cases are $\langle N \rangle = 0$, where no itinerant electrons exist, and $\langle N \rangle = 2$, where all the sites are completely filled and hopping is not possible, as well. So, these two filling factors denote insulators, as expected from conventional band theory (for a band that is either not or completely filled). However, this common picture does not work in general for strongly correlated materials.

Let's consider the integer filling $\langle N \rangle = 1$ (half-filled or particle-hole symmetric case), where we have one electron per site, on average. If the ratio U/t is small, the electrons move between different lattice sites and we find a metal. However, if U/t is big enough, the energetic cost for doubly occupied sites can grow so large, that the electrons get localized. In real materials this effect is triggered by the absence of sufficient screening of the Coulomb interaction in the integer filling scenario [10, Chapter 3]. This heuristic explanation shows how an insulating state (called Mott insulator) can arise for a half-filled band due to strong correlations. Yet, it has to be mentioned that an insulating state does not appear for any non-integer filling factor (and finite t). For those filling regimes singly, doubly or non-occupied sites always coincide with the result that the total energy can be lowered via hopping processes [10, Chapter 3].

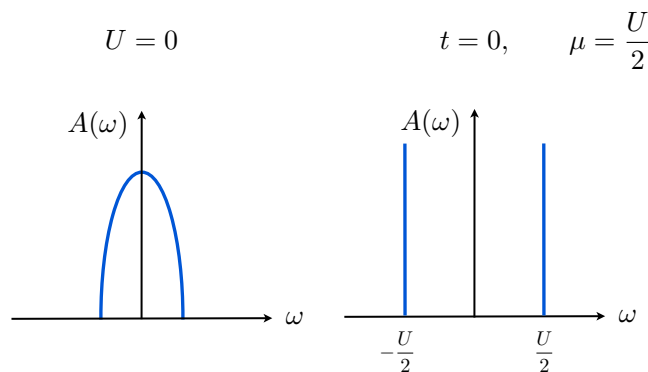


Figure 5.2: Sketch of the local spectral function for the half-filled one-band Hubbard model. In the left panel the Fermi gas limit $U = 0$ is shown, in the right panel the atomic limit $t = 0$ is depicted. While electrons are delocalized for the left case, they are completely localized for the right figure. Adapted from [10, Chapter 3].

The final state for the half-filled Hubbard model is governed by the ratio U/t (or to be more precise, by U/D with the half bandwidth D of the non-interacting lattice density of states). For the Fermi gas limit $U = 0$ the spectral function of the system is equal to the non-interacting lattice density of states $A(\omega) = \frac{1}{N_B} \sum_{\mathbf{k}} \delta(\omega - \varepsilon_{\mathbf{k}})$. In the case of a Bethe lattice (with infinite coordination) we find a semi-elliptical spectral function as sketched in Fig. 5.2. In the atomic limit $t = 0$ the lattice problem separates into a sum of isolated atomic systems. It can be easily shown that only δ -peak excitations at $-\mu$ and $-\mu + U$ arise in this case [10, Chapter 3]. But what happens for intermediate values of U/D ? As indicated above, one expects a transition between the delocalized and localized limits shown in Fig. 5.2.

5.1 The Mott-Hubbard metal-insulator transition (MIT)

In 1998 the correlation induced transition between a paramagnetic metal and a paramagnetic insulator, referred to as “Mott-Hubbard metal-insulator transition” (MIT), was studied by R. Bulla, A.C. Hewson and Th. Pruschke, which was one of the first investigations using the NRG method as “impurity solver” within DMFT [16]. (Magnetic order is assumed to be suppressed in this model, hence it is “frustrated”. For systems with dimension larger than two, an insulating antiferromagnetic phase generally hides the MIT of the unstable paramagnetic phase [10, Chapter 3].) The Mott transition has been one of the early successes of the DMFT approach [3]. As a first quality test we want to reproduce the MIT as performed in [16].

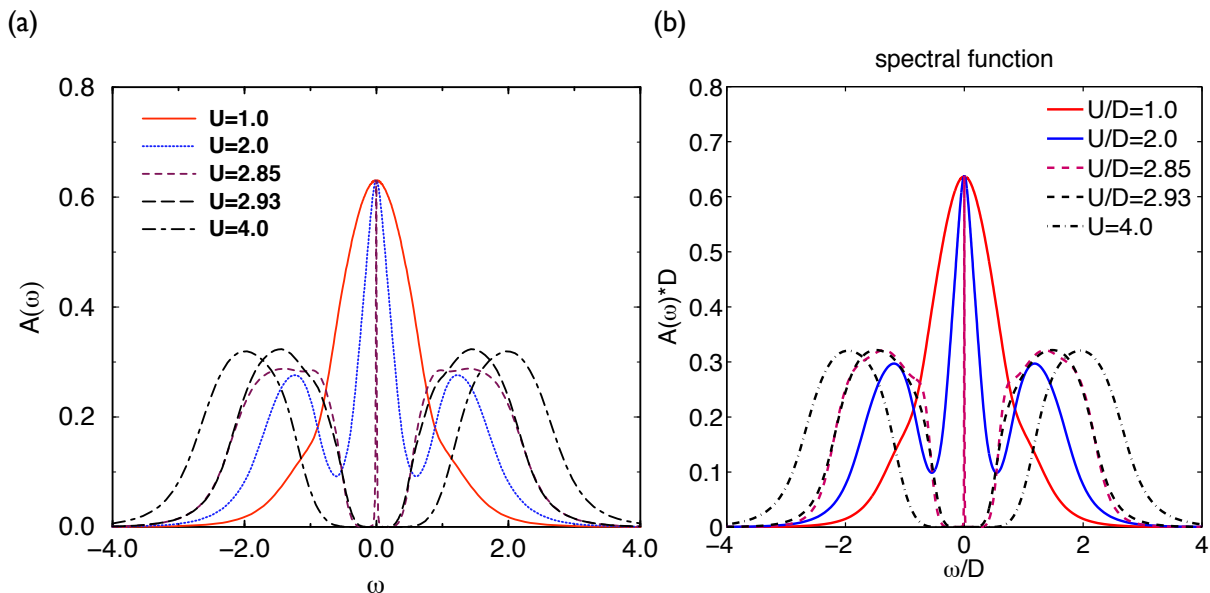


Figure 5.3: MIT illustrated by spectral functions for different values of U , $\mu = U/2$ and $T \approx 0$ for the half-filled one-band Hubbard model. Panel (a) is taken from [16]. In panel (b) our results (obtained with $\Lambda = 2$, $N_z = 4$ and $\sigma = 0.3$ and $N_z = 8$, $\sigma = 0.1$ for $U/D = 2.85$) are plotted.

The MIT is displayed by the shape of the spectral function (or local density of states) $A(\omega) = -\frac{1}{\pi} \text{Im} G_{\text{latt}}(\omega)$, which is calculated with our DMFT+NRG program (see panel (b))

of Fig. 5.3, the results obtained in [16] are presented in panel (a)). Here we concentrate on the half-filled (particle-hole symmetric) one-band Hubbard model at $T = 0$. To demonstrate the MIT, the Coulomb interaction is increased from $U/D = 1$ to $U/D = 4$. For the DMFT self-consistency procedure we use the semi-elliptical Bethe lattice density of states with half bandwidth D . The self-consistency loop starts with a flat band as input function. Its strength is chosen such that the spectral function after the first DMFT iteration shows a (quasiparticle) peak at the Fermi level and thus metallic behavior. We call this a metallic input hybridization in contrast to the insulating input, where a spectral function with gap around the Fermi level is obtained after the first DMFT iteration. Convergence is reached after about 8 iterations (except for $U/D = 2.85$).

For small U ($U/D = 1$) we obtain a spectral function that is similar to the non-interacting case (Fermi gas limit in Fig 5.2 (left panel)). It clearly features a coherent quasiparticle peak around the Fermi level. This is associated with a metallic phase. For intermediate U ($U/D = 2$) a typical three-peak structure develops in the spectrum with a lower and an upper Hubbard band, which are centered at $\pm U/2$, and a quasiparticle peak at $\omega = 0$. While the central peak corresponds to coherent quasiparticle excitations, the Hubbard bands emerge from incoherent atomic-like excitations (as in Fig. 5.2 (right panel), but broadened by the finite hopping amplitude).

This three-peak structure is a characteristic feature of strongly correlated materials, that also occurs for non-integer filling (for sufficiently small temperatures). It reminds of the three-peak spectrum of the conventional SIAM (with the Kondo peak at $\omega = 0$). Yet, it has to be emphasized that the three-peak structure for strongly correlated materials arises from a lattice model, that is mapped self-consistently onto an impurity Anderson model. The Kondo peak in the strong coupling regime of the SIAM originates from local impurity spins, that are completely screened by the bath electrons. In the case of a lattice model the local moments and the screening are both associated with the lattice electrons [10, Chapter 3].

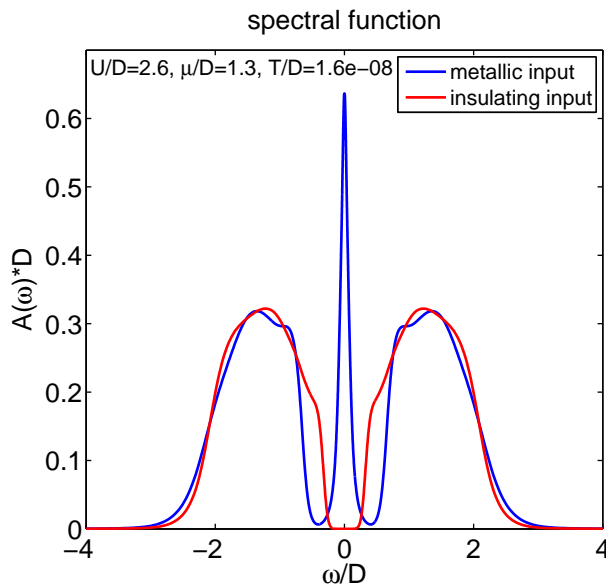


Figure 5.4: Spectral functions for the half-filled one-band Hubbard model in the coexistence region $U_{c,1} < (U/D = 2.6) < U_{c,2}$ with $\mu = U/2$, $T \approx 0$, $N_z = 8$, $\sigma = 0.1/0.3$ (blue curve / red curve) and $\Lambda = 2$. The blue curve was obtained with a metallic input hybridization, the red curve with an insulating one.

When we further increase U the width of the quasiparticle peak decreases and vanishes above a critical value $U_{c,2}/D \approx 2.93$. Up to $U_{c,2}$ the height of the quasiparticle peak is pinned at a fixed value (“Luttinger pinning”) [34]. For $U > U_{c,2}$ a gap develops between the two Hubbard bands, centered at $\pm U/2$, which becomes broader when U grows to larger values. So for $U > U_{c,2}$ we find an insulating phase.

If we start with a metallic input for the DMFT loop the width of the peak around $\omega = 0$ vanishes exponentially slowly with the DMFT iterations (close to the transition point). While the metal to insulator transition occurs at a critical value $U_{c,2}$, the transition from an insulating to a metallic phase is characterized by a lower critical value $U_{c,1} < U_{c,2}$ ($U_{c,1} \approx 2.5$) [17]. In Fig. 5.4 we show the spectral function for $U/D = 2.6$. While we find a quasiparticle peak, starting from the metallic side (blue curve), we get an insulator (red curve) for the same value of U , starting with an insulating input. The physical solution in the coexistence (or hysteresis) region $U_{c,1} < U < U_{c,2}$ is the metallic one, as it exhibits the lower ground state energy (see the discussion in [17]).

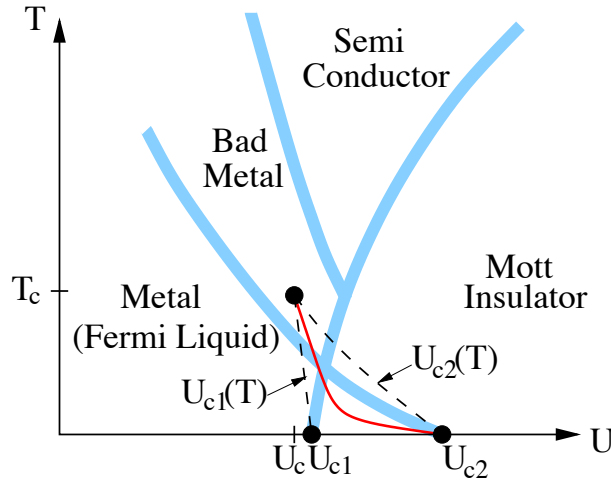


Figure 5.5: Paramagnetic phase diagram for the frustrated one-band Hubbard model within DMFT. Figure taken from [1].

In Fig. 5.5 we show a schematic (paramagnetic) phase diagram for the one-band (frustrated) Hubbard model, plotted for general temperatures and interaction strengths U . Below the critical endpoint (T_c, U_c) the model displays two possible solutions (metal or Mott insulator) in the hysteresis region $U_{c,1}(T) < U(T) < U_{c,2}(T)$, which is confined by the dashed spinodal lines $U_{c,1}(T)$ (where the insulating phase vanishes) and $U_{c,2}(T)$ (where the Fermi liquid properties disappear). The red line gives the first-order phase transition boundary where the free energy of both solutions becomes equal [9]. For temperatures above T_c different transport regimes can occur. The blue shaded crossover line separating the Fermi liquid and the “bad metal” regions (see Sec. 5.3 for details) continues the border $U_{c,2}(T)$ above T_c . Analogously, the blue shaded crossover line of the insulating state is an extension of $U_{c,1}(T)$ for $T > T_c$ [1].

To summarize the results of Fig. 5.3, the MIT is monitored by the existence of a quasiparticle peak in the spectral function. As can be seen, the curves obtained in [16] (panel (a)) coincide with our DMFT+NRG results (panel (b)). Even the bump at around $\omega/D = 0.8$ arises for $U/D = 2.93$, the origin of which is not clarified yet.

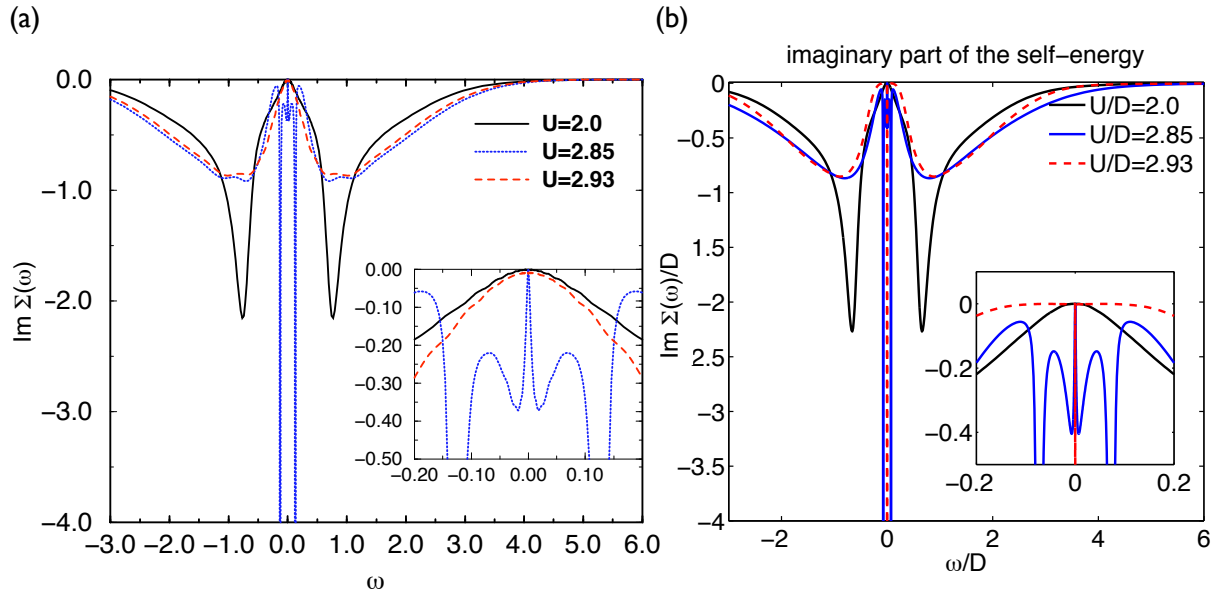


Figure 5.6: MIT illustrated by the imaginary part of the self-energy for different values of U , $\mu = U/2$ and $T \approx 0$ for the half-filled one-band Hubbard model. Panel (a) is taken from [16]. In panel (b) our results (obtained with $\Lambda = 2$, $N_z = 4$ and $\sigma = 0.3$ and $N_z = 8$, $\sigma = 0.1$ for $U/D=2.85$) are plotted. The inset shows the region around the Fermi level $\omega = 0$ in more detail. For the metallic phase Fermi liquid behavior ($\text{Im } \Sigma(\omega = 0) = 0$) can be observed.

Also the structure of the self-energy is found to be qualitatively equal as can be observed in Fig 5.6 and Fig. 5.7. In the panels (a) we show again the results of [16], while the panels (b) display our solutions. The self-energy exhibits peaks in its imaginary and real part at frequencies, that correspond to small weights in the imaginary and real part of the lattice Green's function, respectively, which is revisable for $\text{Im } \Sigma(\omega)$ and $A(\omega)$ in Fig. 5.6 and Fig. 5.3. Therefore a three-peak structure in $A(\omega)$ results in a two-peak structure in $\text{Im } \Sigma(\omega)$. When the quasiparticle peak vanishes with $U \rightarrow U_{c,2}$, the two peaks in $\text{Im } \Sigma(\omega)$ approach and merge to a single δ -peak for the insulating phase (plotted in red in Fig. 5.6 (b), but not shown in Fig. 5.6 (a)). The zoom in the region around $\omega = 0$ (see insets of Fig. 5.6) shows slight differences between the curves of panel (a) and our results. While the black curves for $U/D = 2$ are in good agreement, the blue curve exhibits sharper features in our case, leading to a thinner quasiparticle peak near the transition point. For the red curve the shape near $\omega = 0$ is more flat in panel (b). Near $\omega = 0$ we had to reduce the imaginary part of the self-energy artificially down to zero for the metallic phase. The NRG calculations exhibit a (systematic) small error of about 0.01%, which may slightly grow during the DMFT procedure. This potentially leads to a positive self-energy, that has to be reduced again to ensure causality for the DMFT loop. In Sec. 5.3 we will focus on exact quantitative results near $\omega = 0$ and introduce a strategy to deal with this problem in a controlled way. In general, it is possible to further reduce the error of the DMFT+NRG calculations by increasing numerical effort (such as performing more z-shifts or keeping more states, especially at the first sites of the Wilson chain). These options have not been exhausted for the MIT. Nevertheless we can state that $\text{Im } \Sigma(\omega = 0) = 0$ (within a certain error margin) for the metallic phase, which is connected to Fermi-liquid behavior (see the next section for an

introduction to Fermi liquid theory). The real part of the self-energy (in Fig 5.7) displays a negative slope at $\omega = 0$ for $U < U_{c,2}$ (black and blue curves). In the insulating phase the slope diverges (red dashed curves).

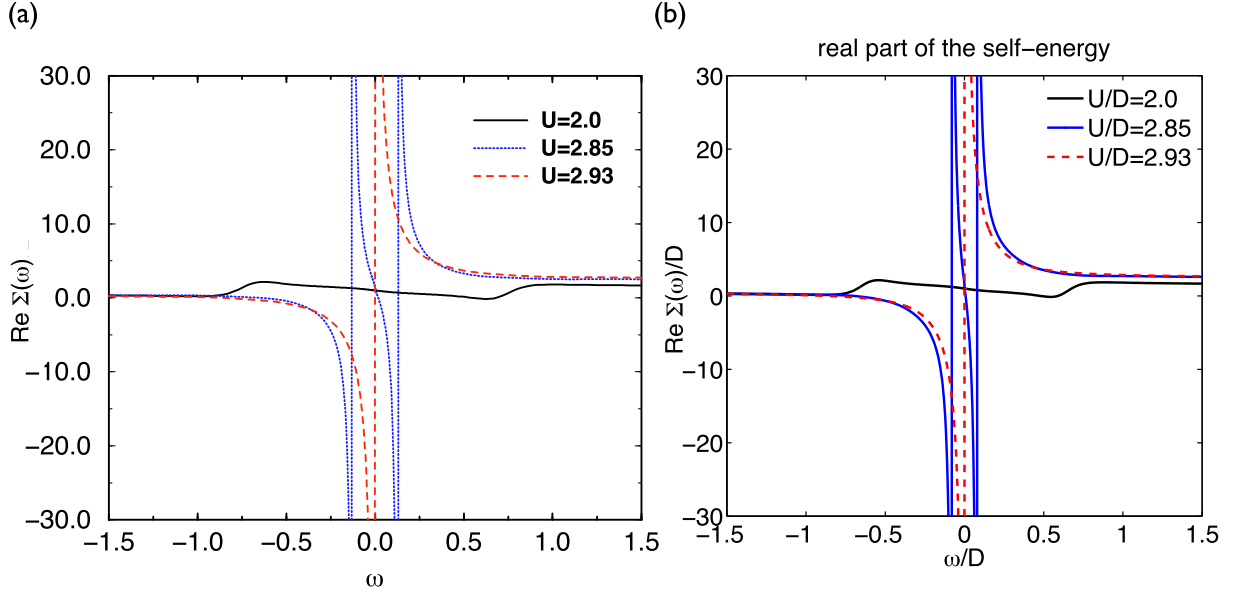


Figure 5.7: MIT illustrated by the real part of the self-energy for different values of U , $\mu = U/2$ and $T \approx 0$ for the half-filled one-band Hubbard model. Panel (a) is taken from [16]. In panel (b) our results (obtained with $\Lambda = 2$, $N_z = 4$ and $\sigma = 0.3$ and $N_z = 8$, $\sigma = 0.1$ for $U/D=2.85$) are plotted.

The Fermi liquid character of the metallic phase is confirmed by the fixed point regime of the corresponding energy flow diagrams. In Fig. 5.8 (a) the RG-flow for $U/D = 2$, $\mu/D = 1$, $T/D \approx 0$, $z = 0$ and $\Lambda = 2$ is shown. Clearly the system flows to the strong coupling or Fermi-liquid fixed point, as also observed in [16].

For $U > U_{c,2}$ we have an insulating phase which is associated with localized electrons and correspondingly unscreened local moments. In this sense, the expression “local moment fixed point” seems appropriate for insulators of the fully frustrated Hubbard model [16]. (Note that for models which are not fully frustrated, the local moments order to an antiferromagnetic phase below the Néel temperature [1]). However, the corresponding RG-flow converges to a finite size spectrum, despite the gap in the spectral function (see Fig. 5.8). This suggests that the fixed point regime at the end of the Wilson chain is not based on a physical but rather on a numerical effect: In the insulating phase the couplings of the star Hamiltonian almost vanish for the inner intervals in the gap, leading to a region with pronounced peaks in the hopping matrix elements (indicated by the red bar in Fig. 5.9). Presumably the Wilson chain effectively decouples in that region. The second part of the chain may then be viewed as a basically independent subsystem that barely influences the NRG results at the impurity. Thus, the Wilson chain could be chosen significantly shorter. To confirm this assumption we repeated the calculation for $U/D = 4$ with a chain length of $N_{\text{max}} = 13$ and obtained the same result, as shown in the inset of Fig. 5.9.

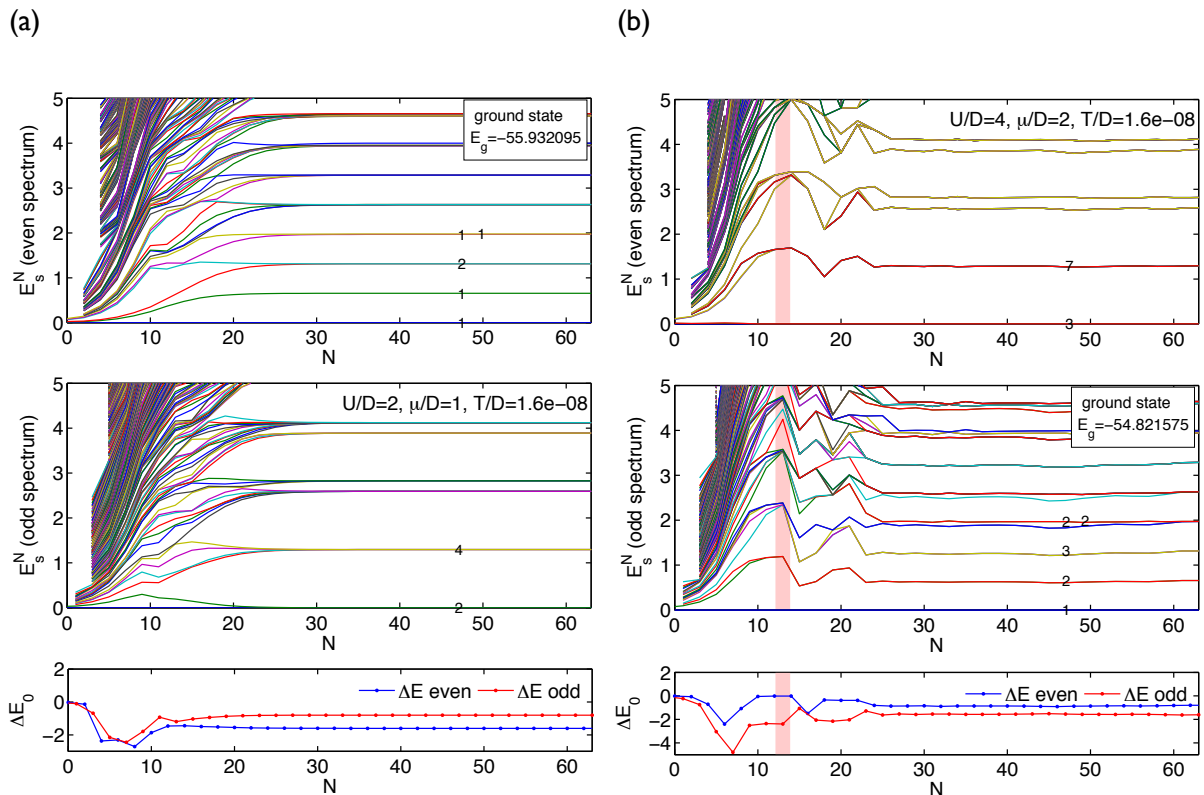


Figure 5.8: Energy flow diagrams for the half-filled one-band Hubbard model for (a) the metallic phase represented by $U/D = 2$ and (b) the insulating phase with $U/D = 4$. Further $\mu = U/2$, $T \approx 0$, $\Lambda = 2$ and $z = 0$ are used. In panel (a) the energies flow to the Fermi liquid fixed point. The red bar in panel (b) indicates the region where the Wilson chain for the insulating phase seems to effectively decouple due to the infinitesimal couplings in the star Hamiltonian. The fixed point regime after the red bar may then be uncontrolled as based on numerical noise. ΔE_0 denotes the energy shift of the ground state energy to zero.

Although the one-band Hubbard model does not contain any material specific details (such as several orbitals and Hund's coupling terms) and the DMFT method is based on the approximation of a local (or momentum-independent) self-energy, the combination of both already yields a profound understanding of the MIT for the whole parameter range U/D (as shown in this section) and also for all values of the temperature T . In the MIT spectral weight is transferred from the quasiparticle peak to the Hubbard bands. For strongly correlated materials this transfer can be induced by temperature, pressure or doping. The MIT is found in materials with quite different crystal structures, such as vanadium oxide (V_2O_3), nickel selenium sulfide ($NiS_{2-x}Se_x$) or (layered) organic compounds [2]. In many transition metal oxides (such as NiO) the Mott mechanism explains their unconventional transport properties. Although the d-band is only partially filled for these materials, they are not good metals as expected by conventional band theory. Due to strong correlations even insulators arise for partially filled bands. Another highly interesting example of transition metal oxides are superconducting cuprates.

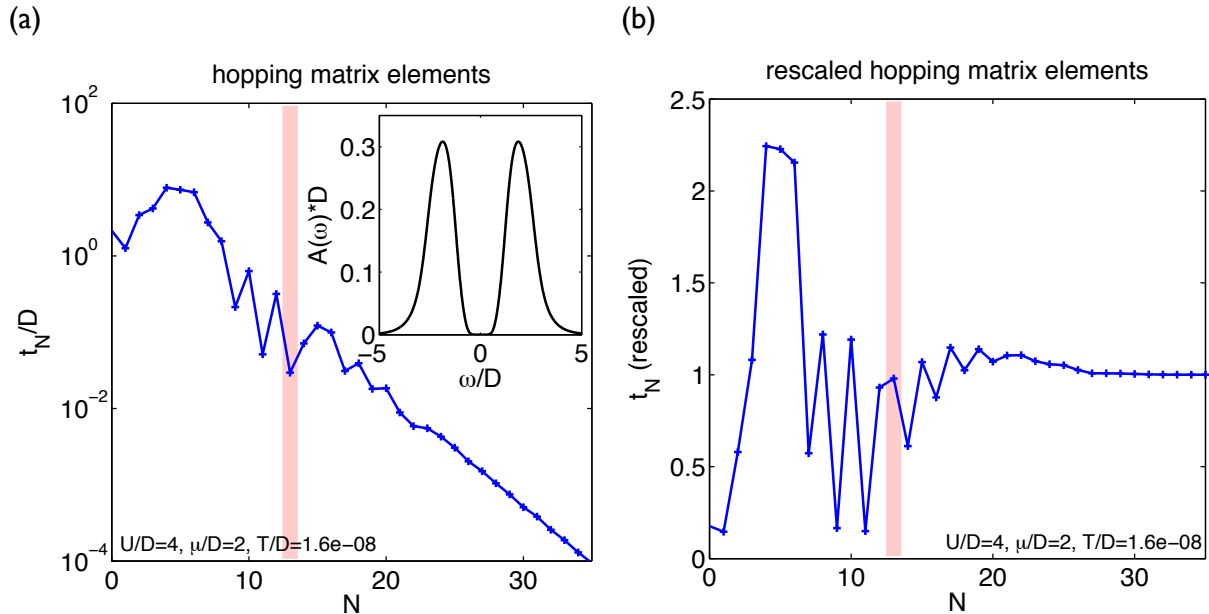


Figure 5.9: Hopping matrix elements for the insulating phase of the half-filled one-band Hubbard model with $U/D = 4$. As for the energy flow diagram $\mu = U/2$, $T \approx 0$, $\Lambda = 2$ and $z = 0$ are used. Panel (a) shows the non-rescaled Wilson chain couplings and the corresponding spectral function in the inset, panel (b) depicts the rescaled Wilson chain couplings. The red bar indicates the region where pronounced peaks arise due to infinitesimal couplings in the “star” Hamiltonian.

5.2 Fermi-liquid theory

In order to understand the nature of the quasiparticle excitations and to classify the metallic and insulating phase of an MIT quantitatively, we examine the structure of the retarded lattice Green’s function and the corresponding self-energy in more detail (following the derivations given in [35, Chapter 15]).

The one-particle retarded Green’s function in DMFT is given as

$$G_{\mathbf{k}}(\omega) = \frac{1}{\omega + \mu - \varepsilon_{\mathbf{k}} - \Sigma(\omega)} \quad (5.3)$$

with the chemical potential μ , the dispersion relation $\varepsilon_{\mathbf{k}}$ and the momentum-independent self-energy $\Sigma(\omega)$ taking local interactions into account. Quantum labels as for the spin are neglected for now. The Fermi wave number \mathbf{k}_F is determined as $\varepsilon_{\mathbf{k}_F} - \mu = 0$. The influence of the interaction part of the Green’s function can be investigated by separating real and imaginary part of the self-energy explicitly,

$$G_{\mathbf{k}}(\omega) = \frac{1}{\omega + \mu - \varepsilon_{\mathbf{k}} - \text{Re} \Sigma(\omega) - i \text{Im} \Sigma(\omega)}, \quad (5.4)$$

which leads to a renormalized Fermi wave number $\tilde{\mathbf{k}}_F$, defined by $\varepsilon_{\tilde{\mathbf{k}}_F} - \mu + \text{Re} \Sigma(\omega) = 0$. For small energies and \mathbf{k} close to $\tilde{\mathbf{k}}_F$ the inverse of the retarded Green’s function can be expanded around $\mathbf{k} = \tilde{\mathbf{k}}_F$ and $\omega = 0$:

$$\tilde{G}_{\mathbf{k}}(\omega) \approx \left[\omega - \omega \partial_{\omega} \text{Re} \Sigma(\omega)|_{\omega=0} - (\mathbf{k} - \tilde{\mathbf{k}}_F) \partial_{\mathbf{k}} \varepsilon_{\mathbf{k}}|_{\mathbf{k}=\tilde{\mathbf{k}}_F} - \text{Im} \Sigma(\omega) \right]^{-1}. \quad (5.5)$$

The result is then brought into a form similar to the non-interacting Green's function

$$G_{\mathbf{k}}^0(\omega) = \frac{1}{\omega + \mu - \varepsilon_{\mathbf{k}} + i\delta}, \quad (5.6)$$

which leads to

$$\tilde{G}_{\mathbf{k}}(\omega) = \frac{Z}{\omega - \tilde{\varepsilon}_{\mathbf{k}} + i\frac{1}{\tau(\omega)}} \quad (5.7)$$

with the quasiparticle weight

$$Z = \frac{1}{1 - \partial_{\omega} \operatorname{Re} \Sigma(\omega)|_{\omega=0}}, \quad (5.8)$$

the inverse quasiparticle lifetime

$$\tau^{-1}(\omega) = -Z \operatorname{Im} \Sigma(\omega) \quad (5.9)$$

for small ω and the effective energy

$$\tilde{\varepsilon}_{\mathbf{k}} = Z(\mathbf{k} - \tilde{\mathbf{k}}_F) \partial_{\mathbf{k}} \varepsilon_{\mathbf{k}}|_{\mathbf{k}=\tilde{\mathbf{k}}_F}. \quad (5.10)$$

Furthermore we introduce the renormalized chemical potential

$$\mu_{\text{eff}} = \mu - \operatorname{Re} \Sigma(\omega = 0), \quad (5.11)$$

which cancels in the above expression due to the definition of the renormalized Fermi wave number $\tilde{\mathbf{k}}_F$. The imaginary part of the self-energy was not expanded explicitly.

The quasiparticle weight is determined by the slope of the real part of the self-energy at $\omega = 0$. As shown in the previous section, the slope is a direct indicator of the MIT. For the metallic phase we get a negative slope at $\omega = 0$ and thus a quasiparticle weight $Z \in (0, 1]$, for the insulating phase the slope diverges, leading to $Z = 0$. Hence, Z reflects the weight of the quasiparticle peak in the spectral function. The weight of the Hubbard bands is then given as $1 - Z$.

This interpretation can be further motivated by evaluating the k -dependent spectral function

$$A_{\mathbf{k}}(\omega) = -\frac{1}{\pi} \operatorname{Im} G_{\mathbf{k}}(\omega) \quad (5.12)$$

which is given as a δ -peak at energy $\varepsilon_{\mathbf{k}} - \mu$,

$$A_{\mathbf{k}}(\omega) = \delta(\omega - (\varepsilon_{\mathbf{k}} - \mu)), \quad (5.13)$$

in the non-interacting case. In the interacting case it is a function with a Lorentzian shaped coherent quasiparticle peak of weight Z at position $\tilde{\varepsilon}_{\mathbf{k}}$ and of width $\tau^{-1}(\omega)$ (for \mathbf{k} close to $\tilde{\mathbf{k}}_F$ and very small ω) and an additional incoherent part of weight $1 - Z$:

$$A_{\mathbf{k}}(\omega) = \frac{1}{\pi} \frac{Z \frac{1}{\tau(\omega)}}{(\omega - \tilde{\varepsilon}_{\mathbf{k}})^2 + \left(\frac{1}{\tau(\omega)}\right)^2} + A'_{\mathbf{k}}(\omega). \quad (5.14)$$

While the first term is given as $-\frac{1}{\pi} \operatorname{Im} \tilde{G}_{\mathbf{k}}(\omega)$, the second term includes the spectral weight that was neglected by performing a first order expansion around $\mathbf{k} = \tilde{\mathbf{k}}_F$ and $\omega = 0$.

Within local DMFT Z is equal to the mass renormalization. In analogy to free electrons with dispersion relation $\varepsilon_{\mathbf{k}} = \mathbf{k}^2/2m$ the effective energy $\tilde{\varepsilon}_{\mathbf{k}}$ in Eq. (5.10) is usually written as

$$\tilde{\varepsilon}_{\mathbf{k}} = \frac{(\mathbf{k} - \tilde{\mathbf{k}}_F) \tilde{\mathbf{k}}_F}{m^*}, \quad (5.15)$$

which leads to

$$\frac{m}{m^*} = Z. \quad (5.16)$$

The inverse lifetime of the quasiparticles for small ω , given by Eq. (5.9), determines the height and width of the Lorentzian quasiparticle peak. Due to interactions, excitations exhibit finite lifetimes as electrons exchange momenta in scattering processes and thus change their quantum state [36, Chapter 4]. $\text{Im} \Sigma(\omega)$ can therefore be associated with the transport scattering rate. For very long lifetimes (and weak excitations) it is possible to represent the excitations of an interacting system as well-defined non-interacting quasiparticles with properly identified excitation energies. This concept, called Fermi liquid theory, was developed by L.D. Landau in the late 1950's and has been further refined, since. It is the basic theoretical background behind the widely used free-electron model (that gives surprisingly good results especially for the description of metals).

It is based on a one-to-one correspondence between long-lived excitations (quasiparticles) of an interacting Fermi liquid and the low-energy excitations of a free Fermi gas [35]. The physical picture of a Landau quasiparticle can be associated with an electron that is surrounded by a screening cloud of particle-hole excitations or analogously density fluctuations, retaining quantum labels of the electrons (like the spin quantum number) but changing its effective parameters (such as the mass) [36, Chapter 4]. This leads to the fact that the quasiparticles can be labeled by the same quantum numbers as the original fermions (if the corresponding operators still commute with the full Hamiltonian). Furthermore they follow Fermi statistics. The influence of the interactions is considered by a renormalization of physical parameters, such as the electron mass which is replaced by an effective mass m^* .

It can be derived that the inverse lifetime of a Landau particle and thus the imaginary part of the self-energy near $\omega = 0$ is given as

$$\text{Im} \Sigma(\omega, T) \sim [\omega^2 + (\pi T)^2] \quad (5.17)$$

for a Fermi liquid [6]. T denotes the temperature. So for small temperatures and near the Fermi surface the lifetime of the excitations becomes large and the interacting single particle Green's function approaches that of free particles, which explains the success of the Fermi liquid theory in the description of interacting systems [35].

In the previous section about the MIT the imaginary part of the self-energy was found to go to zero for $\omega = 0$ and $T = 0$ in the complete metallic phase, which can thus be described by a Fermi liquid.

5.3 Fermi liquid physics and resilient quasiparticles

While we studied the MIT in a primarily qualitative way, we now want to examine the accuracy of our calculations quantitatively. This is done for the asymmetric (hole-doped with $\langle N \rangle = 0.8$ or doping $\delta = 20\%$) one-band Hubbard model that was only recently investigated by X. Deng, J. Mravlje, R. Zitko, M. Ferrero, G. Kotliar and A. Georges, using DMFT (with the semi-elliptical Bethe lattice density of states of half bandwidth D) in combination with continuous time Quantum Monte Carlo simulations (CT-QMC) and NRG [6]. They used this rather simple setting to study the unconventional transport properties of metals with strong electron correlations, which are still poorly understood theoretically.

For conventional metals the resistivity increases with the temperature due to phonon scattering

(above a certain, small temperature below which electron-electron scattering is dominant). In a quasiparticle picture this can be explained by a growing number of thermally-induced scattering events reducing the mean-free-path l . A resistivity maximum is then reached when l becomes shorter than the lattice spacing a , since at this point the quasiparticle description of transport breaks down. This limit, where $l \approx a$ (or similarly $k_{Fl} \sim 1$), is known as the Mott-Ioffe-Regel limit and associated with a temperature T_{MIR} .

For many strongly correlated materials, the resistivity at high temperatures exceeds this limit, which is often called “bad-metallic” behavior. For very small temperatures ($T < T_{\text{FL}}$) they follow Fermi-liquid behavior. In general T_{FL} is much lower than T_{MIR} : in Sr_2RuO_4 for example, $T_{\text{FL}} \approx 20\text{K}$ and $T_{\text{MIR}} \approx 800\text{K}$ [6]. While transport can be described by Landau’s quasiparticles for $T < T_{\text{FL}}$, it has to be clarified how to think of transport for $T > T_{\text{FL}}$. In [6] especially the intermediate regime $T_{\text{FL}} < T < T_{\text{MIR}}$ is investigated. A main result is that well-defined, so called “resilient” quasiparticle (RQP) excitations, can be found clearly above the temperature range in which Fermi liquid theory is valid. These excitations gradually disappear in the crossover to the bad metal regime ($T > T_{\text{MIR}}$). See Fig. 5.10 for an overview of the different transport regimes.

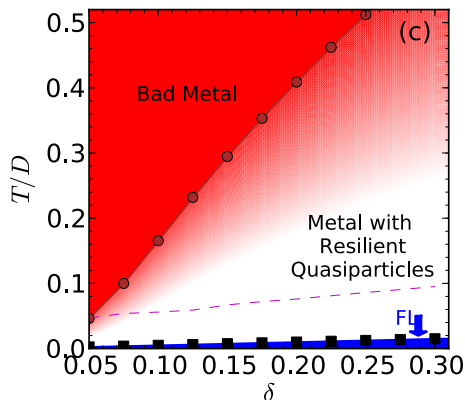


Figure 5.10: The different transport regimes as a function of doping δ : Fermi liquid behavior is found for $T < T_{\text{FL}}$ (blue region), the bad metal regime is indicated in red with the red points as MIR limit, the intermediate white region is the RQP regime. The crossover to the bad metal is gradual. Figure taken from [6], more details are given there.

Furthermore they focus on the precise temperature-dependence of the self-energy including the determination of T_{FL} . Contrary to previous assumptions, it was recently shown (see e.g. [37]) that Fermi liquid physics is highly relevant in cuprate high- T_c superconductors, which underlines the importance of an exact understanding of Fermi-liquid properties of strongly correlated materials.

Here our main goal is to confirm the low-temperature results of [6]. We focus on the validity of Fermi-liquid behavior for small temperatures but also reveal the existence of resilient quasiparticles above T_{FL} . We compare our results with the plots in [6] and have additionally a direct collaboration with Michel Ferrero from the Centre de Physique Théorique, Ecole Polytechnique, France, who provided continuous time Monte Carlo data for some temperatures (labeled with MF when used in our plots). All calculations are performed with the semi-elliptical Bethe lattice density of states of half bandwidth D , $\Lambda = 2$, $N_z = 8$ and $\sigma = 0.1$ for the last DMFT iterations. Our NRG results show excellent convergence with a discarded weight of the order 10^{-15} .

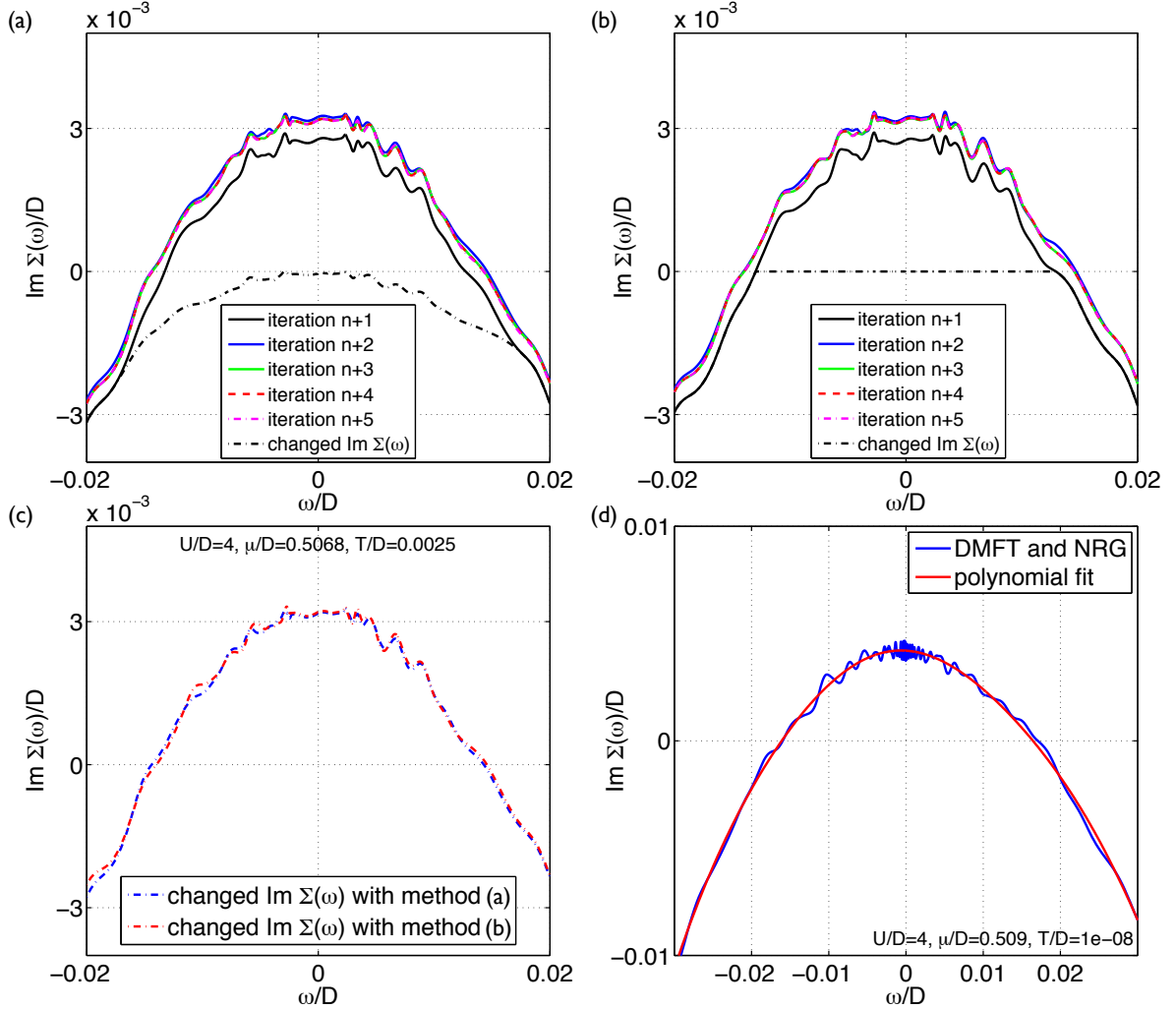


Figure 5.11: Reduction of the imaginary part of the self-energy for $\text{Im } \Sigma(\omega) > 0$ in the case of the asymmetric ($\langle N \rangle = 0.8$) one-band Hubbard model with $U/D = 4, \mu/D = 0.5068, T/D = 0.0025$. Near $\omega = 0$ and for low T the imaginary part of the self-energy can become slightly positive due to small numerical errors and has to be lowered to zero. In panel (a) and (b) the black dash-dot curves show two different possibilities to reduce $\text{Im } \Sigma(\omega) > 0$ for the solid black curve. The reduction is repeated in every DMFT iteration until convergence is reached for sure in iteration $n + 5$ (n is the number of preceding iterations, depending on the input hybridization). In panel (c) we plot the converged results for both strategies, which turn out to be essentially equal. These observations legitimize to define the maximum value $\text{Im } \Sigma(\omega = 0, T = 0)$ as new zero energy point and to shift the curves for all other temperatures $T > 0$ accordingly. Panel (d) illustrates, how we determine $\text{Im } \Sigma(\omega = 0, T = 0)$ using a polynomial fit.

The temperature region for Fermi liquid physics can be determined by examining the onset of T^2 -resistivity (as performed in [6], Fig. 1), but also by the scaling behavior of the imaginary part of the self-energy as given in Eq. (5.17),

$$-\frac{\text{Im } \Sigma(\omega, T)D}{T^2} = A[(\pi)^2 + (\omega/T)^2] \quad (5.18)$$

for small frequencies ω and the scaling of the quasiparticle weight

$$Z(T=0)/Z(T) \approx 1. \quad (5.19)$$

For $T=0$ we should find that $\text{Im}\Sigma(\omega=0, T=0) = 0$. However, as already mentioned before, $\text{Im}\Sigma(\omega)$ can exceed this value in our calculations and become slightly positive. As a positive imaginary part of the self-energy is detrimental during the DMFT iterations, we lower $\text{Im}\Sigma(\omega) > 0$ artificially. In Fig. 5.11 two different possible ways of reducing $\text{Im}\Sigma(\omega)$ are presented. In panel (a) $\text{Im}\Sigma(\omega)$ is rescaled to lower values in a certain frequency region around $\text{Im}\Sigma(\omega) > 0$ after each DMFT iteration. In panel (b) we use a rugged method and just set the whole frequency range $\text{Im}\Sigma(\omega) > 0$ to $\text{Im}\Sigma(\omega) = 0$. Interestingly, the final outcome is not affected by the precise way of changing $\text{Im}\Sigma(\omega) > 0$, as can be seen in panel (c). In addition, the numerical error is systematic and converges within DMFT to a stable final shape (see panel (a) and (b) in Fig. 5.11). So despite changing $\text{Im}\Sigma(\omega) > 0$ artificially down to zero, the DMFT outcome of the next iteration is exactly the same as in the previous iteration when convergence is reached. So we redefine the maximum value $\text{Im}\Sigma(\omega=0, T=0)$ (which is determined using a polynomial fit in panel (d) of Fig. 5.11) as new zero energy point and shift the curves for all other temperatures accordingly. Note that the calculation for $T > 0$ should be performed with the same NRG parameters (Λ , E_{keep} , N_z) as for the $T=0$ run to ensure a similar systematic error.

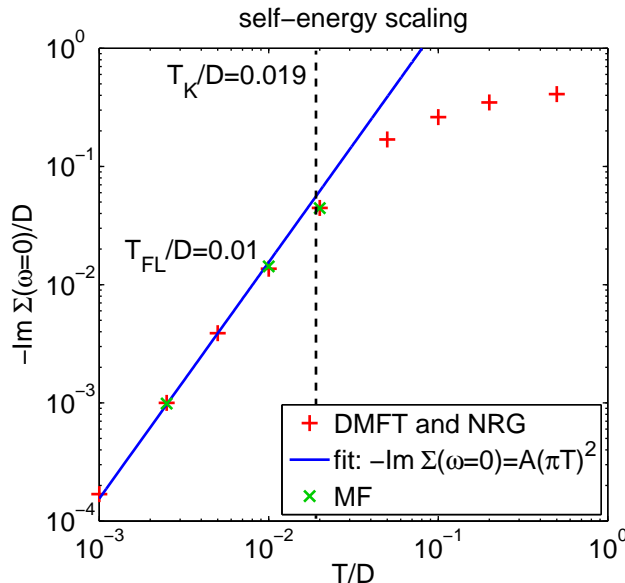


Figure 5.12: $\text{Im}\Sigma(\omega=0, T)$ versus T for the doped one-band Hubbard model with $\langle N \rangle = 0.8$ and $U/D = 4$. For $T < T_{\text{FL}} \approx 0.01D$ Fermi liquid behavior is valid (blue fit) with $A \approx 16$. The green crosses are Monte Carlo data from our collaboration with Michel Ferrero. Further the Kondo temperature T_K is shown, which was deduced from the $T=0$ result.

Now we can identify the constant A in Eq. (5.18) by plotting $\text{Im}\Sigma(\omega=0, T)$ versus T and simultaneously assess the temperature T_{FL} , below which Fermi liquid behavior is valid, using a logarithmic scale for both axes. As long as a linear relation is obtained in Fig. 5.12, Eq. (5.18) holds and A can be read off from the blue fit as $A \approx 16$ (the value $\text{Im}\Sigma(\omega=0) = 0$, which is not shown in the log-log plot, was also used to determine A). In [6] a value close to δ^{-2} is

reported, where δ denotes doping. So our result for A seems to be appropriate. T_{FL} is then estimated as $T_{\text{FL}} \approx 0.01D$.

However, since most of the values $|\text{Im}\Sigma(\omega = 0, T)|$, for which Fermi liquid behavior applies, reside within the energy range of the manual shift $\text{Im}\Sigma(\omega = 0, T = 0)$, the fit has to be taken with caution. Nevertheless, the fact that a systematic Fermi liquid relation can still be observed, justifies our procedure. Further, we reproduced the results shown in Fig. 5.12 for $T < T_{\text{FL}}$ with different NRG settings (higher truncation cutoff).

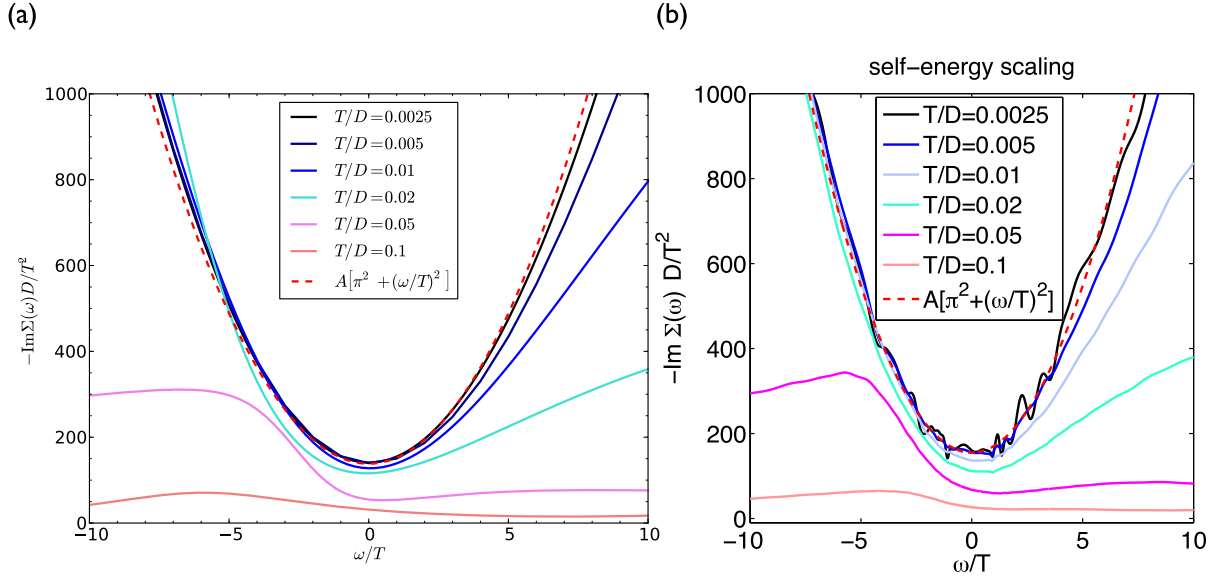


Figure 5.13: Scaling of the imaginary part of the self-energy $-\text{Im}\Sigma(\omega, T)D/T^2$ versus ω/T for the doped one-band Hubbard model with $\langle N \rangle = 0.8$ and $U/D = 4$. Panel (a) is taken from [6] with A close to Z^{-2} . Panel (b) shows our results, which are in good agreement with the left plot. The Fermi liquid relation Eq. (5.18) with $A \approx 16$ is valid for $T < T_{\text{FL}} \approx 0.01D$

In Fig. 5.13 (b) we study the Fermi liquid scaling relation Eq. (5.18) for a frequency range around $\omega = 0$ for different temperatures. Below $T_{\text{FL}} \approx 0.01D$ the Fermi liquid scaling law applies as all the curves follow the shape of the parabola given by the red dashed fit. The data is compared to Fig. 5.13 (a), which shows the results obtained in [6]. Evidently we can reproduce the scaling law of panel (a) to high accuracy, despite the manual shift, that had to be performed to ensure causality. As can be observed in both panels of Fig. 5.13, the imaginary part of the self-energy starts to differ distinctly from the scaling relation for $T_{\text{FL}} \approx 0.01D$ and stronger deviations are generally found for the positive frequency axis, revealing the particle-hole asymmetry of the system.

The scaling of the quasiparticle weight $Z(T = 0)/Z(T)$ is shown in [6] for several dopings (see Fig. 5.14(a)). We concentrate on a doping $\delta = 0.2$ in Fig. 5.14 (b). $T_{\text{FL}} \approx 0.05\delta D = 0.01D$ coincides with the temperature scale, where $Z(T)$ starts to deviate from $Z(T = 0) = 0.21$. Mass renormalization is given by $Z(T = 0) = \frac{m}{m^*} = 0.21 \approx \delta$.

In Fig. 5.15 (b) (and additionally in (a)) we plot the renormalized chemical potential $\mu_{\text{eff}}(T) = \mu(T) - \text{Re}(\omega = 0, T)$. Note that the chemical potential is temperature dependent and has to be determined numerically to ensure a filling of $\langle N \rangle = 0.8$ (see Sec. 6.3.2 for details).

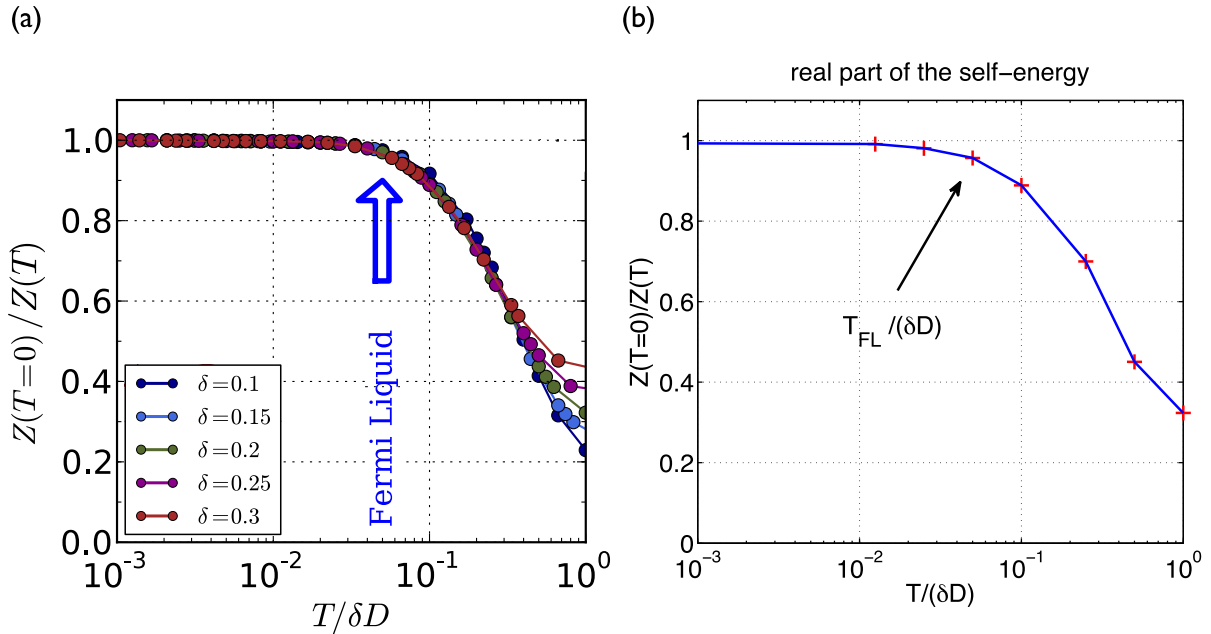


Figure 5.14: Scaling plot of the quasiparticle weight $Z(T=0)/Z(T)$ with $T_{FL} \approx 0.05\delta D$ for the doped one-band Hubbard model ($U/D = 4$) for different dopings δ in panel (a) and $\delta = 0.2$ in panel (b). Panel (a) is adapted from [6], panel (b) depicts our results.

For the Fermi liquid region the renormalized chemical potential $\mu_{\text{eff}}(T)$ is essentially fixed at the effective chemical potential $\mu_{\text{eff}}(T=0)$ (dashed blue line in Fig. 5.15 (a) and (b)). For higher temperatures (in the RQP regime) the effective chemical potential increases rapidly.

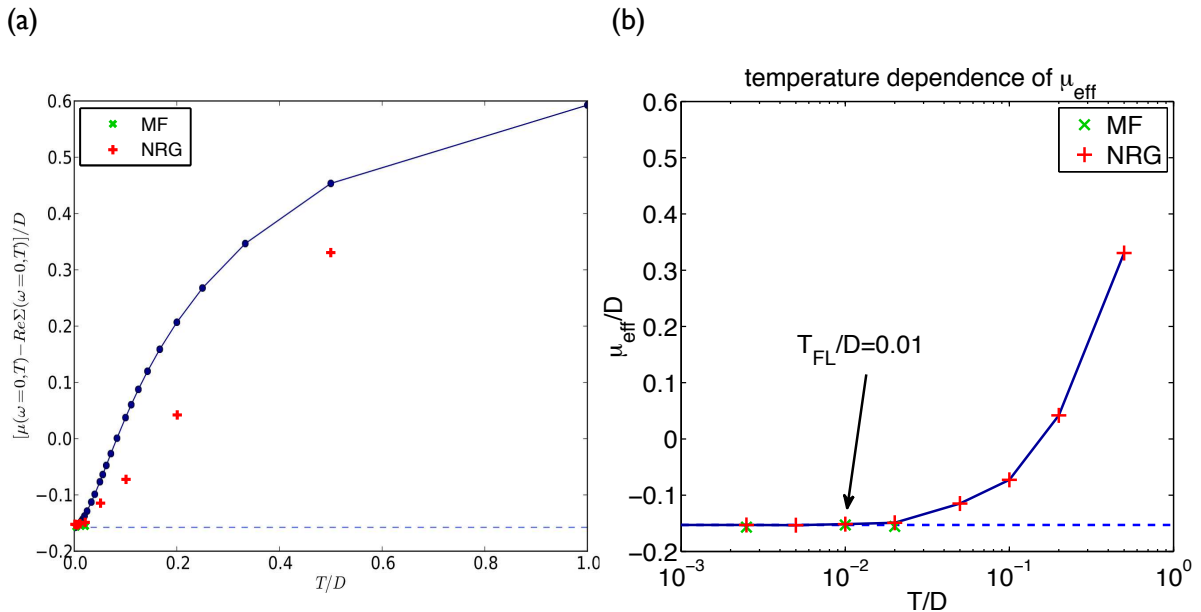


Figure 5.15: Temperature dependence of the renormalized effective chemical potential $\mu_{\text{eff}}(T) = \mu(T) - \text{Re}(\omega = 0, T)$ for the doped one-band Hubbard model with $\langle N \rangle = 0.8$ and $U/D = 4$. While panel (a) (adapted from [6]) shows the behavior mainly for larger temperatures, we concentrate on lower temperatures in panel (b). For $T < T_{FL}$, μ_{eff} is fixed at the effective chemical potential $\mu_{\text{eff}}(T=0)$.

This can be observed for the results of [6] in Fig. 5.15 (a) (dark blue data points) and also for our results (red crosses in panel (a) and (b)). While our NRG results are in good agreement with the QMC data of Michel Ferrero (green crosses in panel (a) and (b)) for low temperatures, there are stronger deviations from the dark blue curve in panel (a) for high temperatures. Nevertheless, we observe the same qualitative behavior.

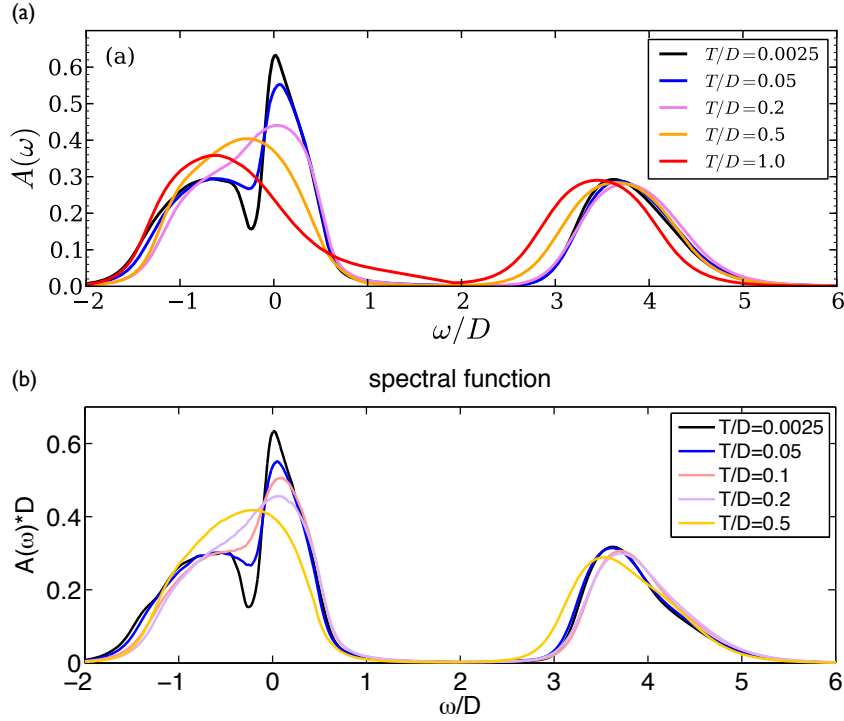


Figure 5.16: Spectral functions for different temperatures for the doped one-band Hubbard model with $\langle N \rangle = 0.8$ and $U/D = 4$. Panel (a) is taken from [6], panel (b) depicts our results. Note that we did not plot a curve for $T/D = 1$, but instead for $T/D = 0.1$, as we want to focus on the RQP regime in this figure. Well-resolved quasiparticle peaks between an upper and a lower Hubbard band exist clearly above the Fermi liquid temperature $T_{\text{FL}} \approx 0.01D$ and gradually disappear when entering the bad metal regime.

In [6] T_{MIR} is found to be approximately on the order of doping δD . As already shown, Fermi liquid physics does not apply in this intermediate regime $T_{\text{FL}} < T < T_{\text{MIR}}$. Nevertheless, well-resolved quasiparticle peaks between an upper and a lower Hubbard band exist clearly above the Fermi liquid temperature T_{FL} and gradually disappear when entering the bad metal regime. The resilient quasiparticles are visible in Fig. 5.16 (a) and (b) for $T/D < 0.2$. Above T_{MIR} only Hubbard satellites remain (yellow curves in panel (a) or (b) and red curve in panel (a)). Panels (a) and (b) of Fig. 5.17 show the corresponding imaginary parts of the self-energy. While the panels (a) are taken from [6], the panels (b) show our results. Please note that we did not plot a curve for $T/D = 1$, but instead for $T/D = 0.1$, as we want to focus on the RQP regime. For $T < T_{\text{FL}}$ we find very long-lived Landau quasiparticles near $\omega = 0$. At finite frequencies and for $T < T_{\text{MIR}}$ the electron-hole asymmetry leads to higher absolute values of the imaginary part of the self-energy and therefore to higher scattering rates for hole-like excitations ($\omega < 0$).

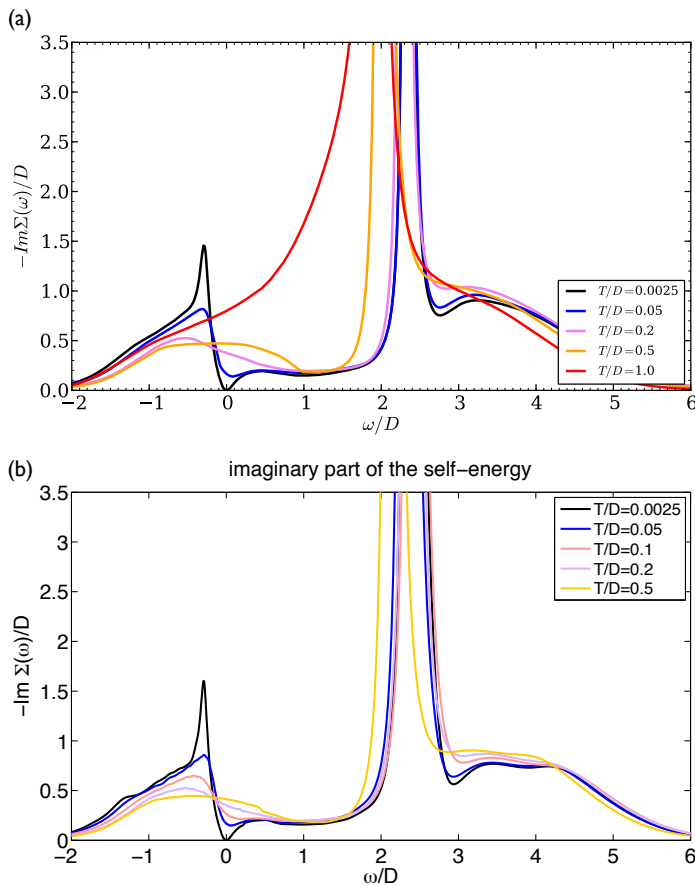


Figure 5.17: Imaginary part of the self-energy for different temperatures for the doped one-band Hubbard model with $\langle N \rangle = 0.8$ and $U/D = 4$. Panel (a) is taken from [6], in panel (b) our results are shown.

For $T < T_{\text{FL}}$ transport is dominated by the excitations at $\omega = 0$. In the RQP regime there exists a certain temperature (denoted by $T^* \approx 0.08D$ in [6]), above which low-energy electron-like excitations with finite $\omega > 0$ dominate transport, as these excitations exhibit larger lifetimes (smaller values for $\text{Im}\Sigma(\omega)$) than those at $\omega = 0$. This can be tracked in Fig. 5.17 (a) for $T/D = 0.2$ and in our results in (b) for $T/D = 0.1$ and $T/D = 0.2$. The plateau for $\omega > 0$ leads to inverse lifetimes that only depend weakly on temperature for $T > T^*$ [6].

To summarize, we have demonstrated the accuracy of our DMFT+NRG calculations by investigating the Fermi liquid physics of the hole-doped one-band Hubbard model with $\langle N \rangle = 0.8$ and $U/D = 4$. We have also found resilient quasiparticles for $T > T_{\text{FL}}$ and revealed the same properties as in [6]. This clearly shows the potential of our program.

Chapter 6

Two-band Hubbard-Kanamori model

Although the one-band Hubbard model can explain general phenomena of strongly correlated materials, like the Mott physics described in the previous Chapter, it is clear that one has to extend the Hubbard Hamiltonian to account for more complex material specific aspects. Typically several orbitals (bands) need to be included with properly chosen hopping integrals, Coulomb repulsion and Hund's coupling between the orbitals.

6.1 Realistic modeling of strongly correlated materials

A recently developed approach to investigate realistic materials is the LDA+DMFT framework, which was shortly introduced in Sec. 2.2.2. While the LDA method provides ab initio many-body model Hamiltonians based on density-functional theory (DFT), DMFT calculations include strong electronic correlation effects, which are not yet incorporated within LDA.

Let's consider an example to understand the basic concept of the (realistic) modeling of strongly correlated materials, following [10, Chapter 6] and [38]. A prevalent lattice structure of transition-metal compounds is the cubic perovskite with KCuF_3 as a common representative (see Fig 6.1 (a)). The transition metal atom (Cu) is situated at the center of a F-octahedron and surrounded by cubically arranged K-atoms. In principle, the nominal valence electrons of KCuF_3 are distributed among the atomic orbitals of the given atoms as $\text{K}^+(4s^0)$, $\text{F}^-(2p^6)$ and $\text{Cu}^{2+}(3d^94s^0)$. However, a cubic crystal symmetry at the Cu sites leads to a splitting of the 5-fold degenerate 3d-orbitals into the lower energy (3-fold degenerate) t_{2g} and the partially filled (2-fold degenerate) e_g -manifold with higher energy. The former consists of the d_{xy} , d_{xz} and d_{yz} orbitals and the latter of the $d_{x^2-y^2}$ and $d_{3z^2-r^2}$ orbitals, which are depicted in Fig. 6.1 (b). So we get $(t_{2g}^6 e_g^3)$ instead of $(3d^9 4s^0)$ for Cu. The experimental structure of KCuF_3 (R in Fig. 6.1 (a)) reveals that a perfect cubic crystal field ($I_{\delta=0}$ in Fig. 6.1 (a), where δ now denotes the cubic crystal field distortion) is an idealization. A more realistic description has to account for the Jahn-Teller distortion of the F-octahedron (due to coupling between electrons and lattice), resulting in CuF bonds of different length (short (s) and long (l) bonds) in the xy-plane, that additionally alternate along the x- and y-direction of the pseudocubic axes (shown at the corner of Fig. 6.1 (a)) [38]. Besides, the conventional tetragonal cell is compressed. These deviations from a perfect cubic crystal symmetry further split the e_g doublet into the lower energy orbital $d_{3l^2-r^2}$ and the higher energy orbital $d_{s^2-y^2}$. The latter leads to the orbital pattern of Fig. 6.1 (a).

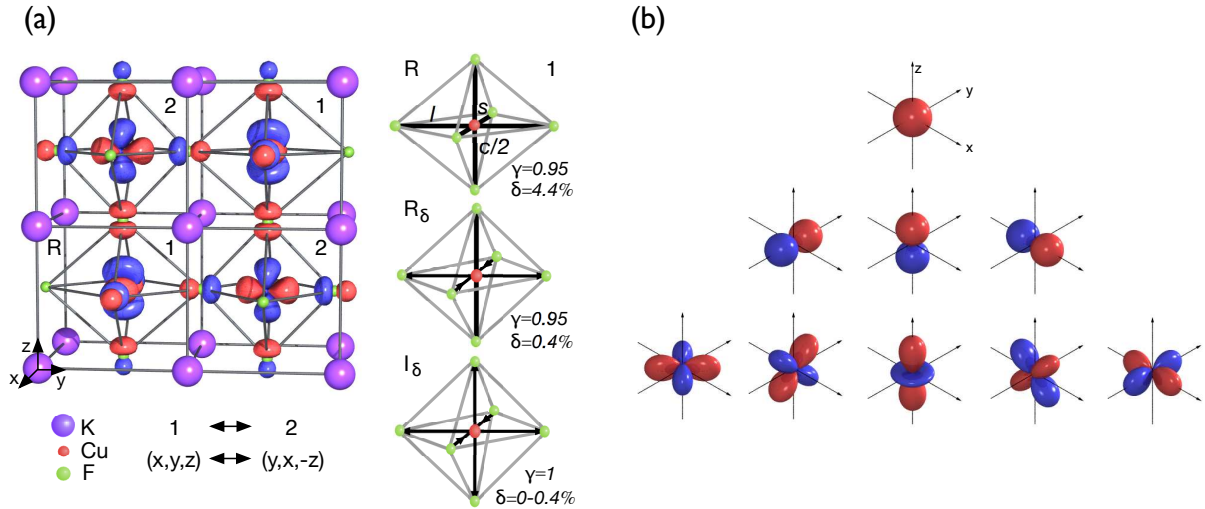


Figure 6.1: Panel (a) (taken from [38]) illustrates the crystal structure and orbital-order in a -type KCuF_3 . The transition metal atom (Cu) is situated at the center of a F-octahedron and surrounded by cubically arranged K-atoms. The tetragonal conventional cell is described by the axes \mathbf{a} , \mathbf{b} and \mathbf{c} , while the pseudocubic axes, shown at the left corner, are given as $\mathbf{x} = (\mathbf{a} + \mathbf{b})/2$, $\mathbf{y} = (-\mathbf{a} + \mathbf{b})/2$ and $\mathbf{z} = \mathbf{c}/2$. The experimental structure is labeled with R. Due to Jahn-Teller distortion (measured by $\delta = (l - s)/(l + s)/2$), the F-octahedron features long (l) and short (s) bonds in the xy-plane. Further, it is compressed, which is indicated by $\gamma = c/a\sqrt{2} < 1$. The structure R at the right side of panel (a) corresponds to site 1 in the left illustration, while the F-octahedron at site 2 is rotated in the xy-plane by an angle of 90 degrees. I_δ with $\delta = 0$ (no distortions) denotes an idealized structure with a perfect cubic crystal field at the Cu-atoms, leading to a splitting of the 5-fold degenerate 3d-orbitals into the (3-fold degenerate) t_{2g} and the partially filled (2-fold degenerate) e_g -manifold. Panel (b) (taken from [10, Chapter 6]) depicts atomic orbitals (real harmonics). The first row shows the s-orbital, the second row illustrates the p-orbitals (p_x , p_y and p_z), the third row figures the five d-orbitals (d_{xy} , d_{yz} , $d_{3z^2-r^2}$, d_{xz} and $d_{x^2-y^2}$).

Using the LDA approach one can calculate the band structure for KCuF_3 , which is shown in Fig. 6.2 (a). The black curves denote the empty s-like bands of Cu and K, as well as the filled p-like bands of F. The t_{2g} -like bands of Cu are depicted in red. As they are completely filled, they do not hybridize with the e_g -like bands, which are located around the Fermi level, suggesting the system to be metallic. However KCuF_3 is actually insulating.

At this point the importance of combining LDA predictions with DMFT calculations becomes clear. As electron-electron interactions are only considered in the sense of a static mean-field within LDA, this method fails to describe strongly correlated materials.

For DMFT calculations it is essential to work with a minimal model Hamiltonian, that can still be solved numerically. Nevertheless, the crucial material specific degrees of freedom have to be maintained. Based on the idea of Wilson’s renormalization group, it is possible to construct low energy models with renormalized physical parameters, by integrating out the high-energy degrees of freedom. In the context of LDA this procedure is known as “massive downfolding” and results in few-band model Hamiltonians, that can then be solved with DMFT.

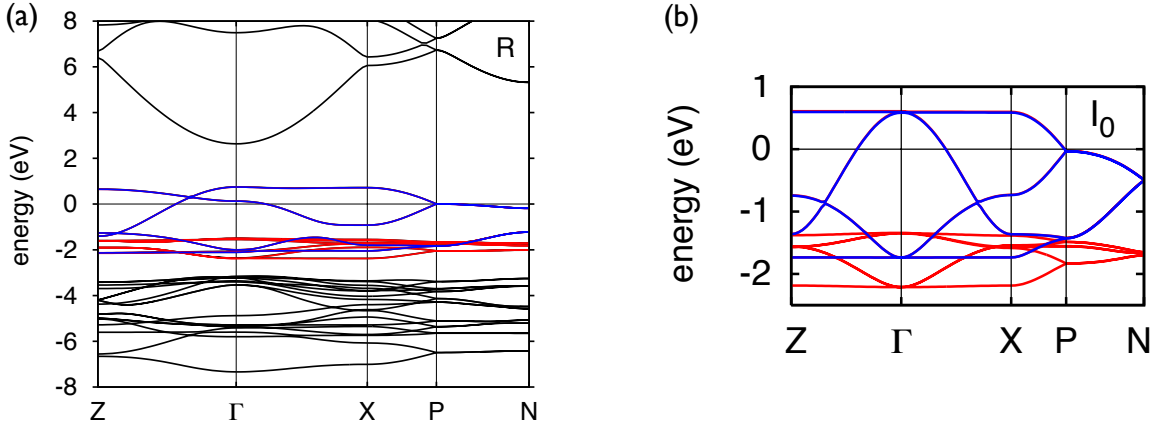


Figure 6.2: LDA band structure of KCuF_3 with the e_g -like bands in blue, the t_{2g} -like bands in red and other bands in black. Panel (a) (adapted from [10, Chapter 6]) is calculated for the experimental structure R, panel (b) (adapted from [38]) for the idealized structure I_0 with partially filled (2-fold degenerate) e_g -orbitals.

For KCuF_3 one could for simplicity assume perfect cubic crystal symmetry at the Cu atoms, leading to the band structure in Fig. 6.2 (b) with degenerate e_g bands. It was calculated with the N^{th} -order muffin-tin orbital method (NMTO), a DFT method, based on atomic-like orbitals [38]. In the downfolding procedure a new localized basis of Wannier functions is constructed, including all relevant degrees of freedom, resulting again in orbitals with $3z^2 - r^2$ and $x^2 - y^2$ symmetry. However, they are of longer range compared to the original atomic orbitals, since they contain p-tails on the downfolded neighbouring F-atoms [10, Chapter 6]. From this Wannier basis one can derive a basic Hubbard Hamiltonian

$$\hat{H} = \hat{H}_{\text{LDA}} + \sum_i (\hat{H}_U)_i - \hat{H}_{\text{DC}}, \quad (6.1)$$

$$\hat{H}_{\text{LDA}} = \sum_{ij} \sum_{mm'\sigma} t_{ij}^{mm'} \hat{c}_{im\sigma}^\dagger \hat{c}_{jm'\sigma}, \quad (6.1a)$$

$$\begin{aligned} \hat{H}_U = & U \sum_m \hat{n}_{m\uparrow} \hat{n}_{m\downarrow} + U' \sum_{m \neq m'} \hat{n}_{m\uparrow} \hat{n}_{m'\downarrow} + (U' - J) \sum_{m < m'} \hat{n}_{m\sigma} \hat{n}_{m'\sigma} \\ & - J \sum_{m \neq m'} \hat{d}_{m\uparrow}^\dagger \hat{d}_{m\downarrow} \hat{d}_{m'\downarrow}^\dagger \hat{d}_{m'\uparrow} + J \sum_{m \neq m'} \hat{d}_{m\uparrow}^\dagger \hat{d}_{m\downarrow}^\dagger \hat{d}_{m'\downarrow} \hat{d}_{m'\uparrow}, \end{aligned} \quad (6.1b)$$

for a cubic crystal environment with e_g -manifold ($m, m' = 3z^2 - r^2, x^2 - y^2$), where $U' = U - 2J$. i and j label the lattice sites. $\hat{c}_{im\sigma}^{(\dagger)}$ destroys (creates) an electron of spin σ in orbital m at site i . $\hat{n}_{im\sigma}$ is the corresponding particle number operator. Note that the Hamiltonian is not only valid for the special case of KCuF_3 , but can be generally used as a model for transition metal compounds with perovskite lattice structure, including three-band systems with partially filled t_{2g} -orbitals [10, Chapter 6]. Then U' is in principle not confined to $U - 2J$, but still a common choice. While three-band models with partially filled t_{2g} -orbitals describe “early” transition metal compounds like Ti, V or Cr, two-band models are appropriate for “late” transition metal compounds, such as Ni or Cu, where the t_{2g} -orbitals are completely filled and the Fermi level is

situated within the e_g -orbitals from an LDA point of view [1]. As the interaction term takes the Kanamori form [39], it is often referred to as Hubbard-Kanamori Hamiltonian. A generalization of the Hubbard-Kanamori Hamiltonian to an arbitrary number of orbitals is given in [3].

The kinetic part (often calculated via LDA) is described by the amplitude $t_{ij}^{mm'}$, which is determined via the localized Wannier functions. The $i \neq j$ terms are the hopping integrals. Due to the hybridization of the transition metal d-shells with the p-orbitals of the neighboring atoms (F in the case of KCuF_3), hopping processes are possible between the correlated d-states of different sites. The on-site term ($i = j$) provides the crystal field matrix with the local energy levels of the orbitals for $m = m'$ [10, Chapter 6].

The interaction term considers on-site interactions between electrons on the localized Wannier orbitals to account for strong correlation effects (which are not considered in the LDA part of the Hamiltonian). The first three terms in \hat{H}_U are density-density interactions and written as a product of particle number operators. U gives the intra-orbital ($m = m'$) Coulomb interaction, the second term includes the inter-orbital ($m \neq m'$) Coulomb interaction between electrons of different spin (U') and the third term between electrons with parallel spin ($U' - J$). The exchange integral J describes the effect of Hund's coupling. The former of the last two terms accounts for spin-flip processes, the latter for two-particle (pair) hopping between different orbitals.

The last term \hat{H}_{DC} in the multi-band Hamiltonian Eq. (6.1) is the double-counting correction, that cancels the electron-electron interaction contained in the hopping term in the case of an LDA-based kinetic-energy part of the Hamiltonian. For the downfolded model this is just an energy shift and can be absorbed in the chemical potential [10, Chapter 6].

For further discussions of KCuF_3 , including DMFT calculations, we refer the reader to [38].

6.2 The DMFT equations for multi-band models

To solve a multi-band (multi-orbital) Hubbard-Kanamori model with an arbitrary number M of orbitals ($m, m'=1, 2, \dots, M$) within DMFT, we have to generalize the DMFT equations, which have been introduced in Chapter 2 for the one-band Hubbard model.

A multi-band Hubbard-Kanamori Hamiltonian can be written as

$$\hat{H} = \sum_{im\sigma} (-\mu_m) \hat{n}_{im\sigma} + \sum_{\langle ij \rangle mm'\sigma} t_{mm'} \hat{c}_{im\sigma}^\dagger \hat{c}_{jm'\sigma} + \sum_i (\hat{H}_U)_i \quad (6.2a)$$

$$= \sum_{km\sigma} (-\mu_m) \hat{n}_{km\sigma} + \sum_{\mathbf{k}mm'\sigma} \varepsilon_{\mathbf{k}}^{mm'} \hat{c}_{\mathbf{k}m\sigma}^\dagger \hat{c}_{\mathbf{k}m'\sigma} + \sum_i (\hat{H}_U)_i \quad (6.2b)$$

for translationally invariant systems, where the chemical potential μ_m and the hopping amplitude $t_{mm'}$ between two neighboring sites ($\langle ij \rangle$) are site independent. The last term is kept in its local spatial representation.

From an equation of motion ansatz one can simply derive (see Appendix B for details) a generalized matrix expression for the lattice Green's function in momentum space:

$$G_{\text{latt}, \mathbf{k}}^{m\sigma, m'\sigma'}(\omega)^{-1} = \langle \hat{c}_{\mathbf{k}m\sigma} | \hat{c}_{\mathbf{k}m'\sigma'}^\dagger | \omega \rangle^{-1} = \delta_{\sigma\sigma'} [(\omega + \mu_m) \delta_{mm'} - \varepsilon_{\mathbf{k}}^{mm'} - \Sigma_{mm'}(\omega)]. \quad (6.3)$$

Note that we concentrate on systems, where the total spin is conserved, resulting in matrix terms, which are diagonal with respect to the spin index. The on-site lattice Green's function is then expressed as

$$G_{\text{latt}}^{m\sigma, m'\sigma'}(\omega) = \frac{\delta_{\sigma\sigma'}}{N_B} \sum_{\mathbf{k}} [(\omega + \mu_m) \delta_{mm'} - \varepsilon_{\mathbf{k}}^{mm'} - \Sigma_{mm'}(\omega)]^{-1}, \quad (6.4)$$

or equivalently in matrix notation:

$$\mathbf{G}_{\text{latt}}(\omega) = \frac{1}{N_B} \sum_{\mathbf{k}} [(\omega + \mu_m)\mathbf{1} - \boldsymbol{\varepsilon}_{\mathbf{k}} - \boldsymbol{\Sigma}(\omega)]^{-1}. \quad (6.5)$$

As in the case of the one-band Hubbard model, also the multi-band Hubbard-Kanamori Hamiltonian is mapped onto an effective quantum impurity model - the multi-band impurity Anderson model, consisting of an impurity site with M local levels coupled to M reservoirs:

$$\hat{H}_{\text{MA}} = \hat{H}_{\text{imp}} + \hat{H}_{\text{bath}} + \hat{H}_{\text{cpl}}, \quad (6.6)$$

$$\hat{H}_{\text{imp}} = \sum_{m\sigma} (-\mu_m) \hat{d}_{m\sigma}^\dagger \hat{d}_{m\sigma} + \hat{H}_U, \quad (6.6a)$$

$$\hat{H}_{\text{bath}} = \sum_{km\sigma} \varepsilon_k^m \hat{c}_{km\sigma}^\dagger \hat{c}_{km\sigma}, \quad (6.6b)$$

$$\hat{H}_{\text{cpl}} = \sum_{kmm'\sigma} V_k^{mm'} (\hat{d}_{m\sigma}^\dagger \hat{c}_{km'\sigma} + \text{h.c.}). \quad (6.6c)$$

$\hat{d}_{m\sigma}^{(\dagger)}$ is the annihilation (creation) operator for an electron of spin σ in orbital m at the impurity site. The bath operators are given as $\hat{c}_{km\sigma}^{(\dagger)}$ and act on electrons of spin σ in reservoir m . The impurity Green's function reads

$$G_{\text{imp}}^{m\sigma, m'\sigma'}(\omega)^{-1} = \langle \hat{d}_{m\sigma} | \hat{d}_{m'\sigma'}^\dagger | \omega \rangle^{-1} = \delta_{\sigma\sigma'} [(\omega + \mu_m)\delta_{mm'} - \Delta_{mm'}(\omega) - \Sigma_{mm'}(\omega)], \quad (6.7)$$

with the hybridization matrix $\Delta_{mm'}(\omega) = \sum_{k\tilde{m}} \frac{V_k^{m\tilde{m}} V_{k\tilde{m}}^{m'}}$ and the self-energy matrix $\Sigma_{mm'}(\omega)$, and can be written compactly in matrix form as well (see Appendix C for a derivation):

$$\mathbf{G}_{\text{imp}}(\omega)^{-1} = (\omega + \mu_m)\mathbf{1} - \boldsymbol{\Delta}(\omega) - \boldsymbol{\Sigma}(\omega). \quad (6.8)$$

The mapping of the multi-orbital lattice problem onto the multi-band Anderson model is again defined by equating the on-site lattice Green's function and the impurity Green's function,

$$\mathbf{G}_{\text{latt}}(\omega) \stackrel{!}{=} \mathbf{G}_{\text{imp}}(\omega), \quad (6.9)$$

now given in matrix representation, which results in

$$\mathbf{G}_{\text{latt}}(\omega)^{-1} + \boldsymbol{\Sigma}(\omega) = (\omega + \mu_m)\mathbf{1} - \boldsymbol{\Delta}(\omega). \quad (6.10)$$

Then the self-consistency condition takes the general matrix form

$$\boldsymbol{\Gamma}(\omega) = \text{Im} \left(\mathbf{G}_{\text{latt}}(\omega)^{-1} + \boldsymbol{\Sigma}(\omega) \right) \quad (6.11)$$

with $\boldsymbol{\Sigma}(\omega) = \mathbf{F}(\omega)\mathbf{G}(\omega)^{-1}$ defined as in Appendix C:

$$F_{m\sigma, m'\sigma'}(\omega) = \langle [\hat{d}_{m\sigma}, \hat{H}_U] | \hat{d}_{m'\sigma'}^\dagger | \omega \rangle, \quad (6.12)$$

$$G_{m\sigma, m'\sigma'}(\omega) = G_{\text{imp}}^{m\sigma, m'\sigma'}(\omega). \quad (6.13)$$

Thus the self-consistency procedure is essentially the same as in Fig. 2.5, one just has to use the generalized matrix expressions in the DMFT equations.

6.3 Hund's coupling in the two-band Hubbard-Kanamori model

We now want to test our DMFT+NRG program for a more complex lattice problem - the two-band Hubbard-Kanamori model with cubic crystal symmetry and therefore 2-fold degenerate e_g -orbitals ($M = 2$):

$$\hat{H} = -\mu \sum_{im\sigma} \hat{n}_{im\sigma} + \sum_{(ij)} \sum_{mm'\sigma} (t\delta_{mm'}) \hat{c}_{im\sigma}^\dagger \hat{c}_{jm'\sigma} + \sum_i (\hat{H}_U)_i, \quad (6.14)$$

with the on-site interaction term Eq. (6.1b),

$$\begin{aligned} \hat{H}_U = & U \sum_m \hat{n}_{m\uparrow} \hat{n}_{m\downarrow} + (U - 2J) \sum_{m \neq m'} \hat{n}_{m\uparrow} \hat{n}_{m'\downarrow} + (U - 3J) \sum_{m < m'} \hat{n}_{m\sigma} \hat{n}_{m'\sigma} \\ & - J \sum_{m \neq m'} \hat{d}_{m\uparrow}^\dagger \hat{d}_{m\downarrow} \hat{d}_{m'\downarrow}^\dagger \hat{d}_{m'\uparrow} + J \sum_{m \neq m'} \hat{d}_{m\uparrow}^\dagger \hat{d}_{m\downarrow} \hat{d}_{m'\downarrow} \hat{d}_{m'\uparrow}. \end{aligned}$$

i and j label the lattice sites and $m, m' = 1, 2$ the two e_g -orbitals. $\sigma = \uparrow, \downarrow$ is the spin index and μ the chemical potential as before. Surely, this reduced model with orbital degeneration and intra-orbital hopping only ($t\delta_{mm'}$) may not include all relevant degrees of freedom to describe specific real materials, but it may give important indications of the kind of microscopic detail, that does lead to certain physical effects in the group of transition metal compounds with perovskite structure.

The two-band Hubbard-Kanamori model has been intensively investigated over the last years, revealing for example the influence of Hund's coupling on the metal-insulator transition (MIT). Also DMFT in combination with NRG was used (among others) by Th. Pruschke and R. Bulla 2005 [19], R. Peters and Th. Pruschke 2010 [21] and R. Peters, N. Kawakami and Th. Pruschke 2011 [21], the first studying the MIT, the last two discussing orbital order and ferromagnetism (at quarter filling).

6.3.1 The two-band Hubbard-Kanamori Hamiltonian in the context of DMFT and NRG

In the DMFT procedure the two-band lattice model is mapped onto a two-band Anderson model (see Eq. (6.6) with $M = 2$). As we neglect orbitally off-diagonal hopping, the hybridization matrix becomes completely diagonal and so do the self-energy and the Green's function matrices, leading to a system of two completely decoupled DMFT self-consistency loops. Thereby, we can use again the expressions of the one-band Hubbard model, but now for each orbital, respectively. Further, we assume the same band structure for both bands, given by the semi-elliptical Bethe lattice DOS with half-bandwidth D .

In the NRG approach we map the two-band impurity Anderson model onto a semi-infinite Wilson chain. The site dimension is significantly larger compared to the conventional SIAM. Instead of 4 for a one-band setup, one Wilson chain site now exhibits 16 possible quantum states. This implies a dramatic increase of the Hilbert space with each site added to the chain. Therefore it is absolutely crucial to exploit the symmetries of the system to reduce the effective number of kept states (multiplets, see Sec. 3.2.2). In addition, we choose large values of the discretization parameter Λ , which allows a further significant reduction of states that have to be kept, due to an increased energy scale separation along the Wilson chain. In our calculations we will apply $\Lambda = 4$ and perform z -averaging, using $N_z = 4$ shifts of the discretization grid.

In order to work out the symmetries of our model, we investigate the local interaction part \hat{H}_U of the two-band Hubbard-Kanamori Hamiltonian. A compact form in terms of symmetry operators is given in the Appendix of [3]. With the orbital isospin generators,

$$\hat{\mathbf{T}} = \frac{1}{2} \sum_{mm'\sigma} \hat{d}_{m\sigma}^\dagger \boldsymbol{\tau}_{mm'} \hat{d}_{m'\sigma}, \quad (6.15)$$

the spin operators,

$$\hat{\mathbf{S}} = \sum_m \hat{\mathbf{S}}_m = \frac{1}{2} \sum_{m\sigma\sigma'} \hat{d}_{m\sigma}^\dagger \boldsymbol{\tau}_{\sigma\sigma'} \hat{d}_{m\sigma'}, \quad (6.16)$$

(which are both given in terms of the Pauli matrices τ_i , $i = x, y, z$) and the total number operator,

$$\hat{N} = \sum_m \hat{N}_m = \sum_{m\sigma} \hat{n}_{m\sigma}, \quad (6.17)$$

we rewrite the contributions in Hamiltonian Eq. (6.14):

$$\sum_m \hat{n}_{m\uparrow} \hat{n}_{m\downarrow} = \frac{\hat{N}^2}{4} + \hat{T}_z^2 - \frac{\hat{N}}{2}, \quad (6.18a)$$

$$\sum_{m \neq m'} \hat{n}_{m\uparrow} \hat{n}_{m'\downarrow} = -\hat{S}_z^2 - \hat{T}_z^2 + \frac{\hat{N}}{2}, \quad (6.18b)$$

$$\sum_{m < m'} \hat{n}_{m\sigma} \hat{n}_{m'\sigma} = \frac{\hat{N}^2}{4} + \hat{S}_z^2 - \frac{\hat{N}}{2}, \quad (6.18c)$$

$$\sum_{m \neq m'} \hat{d}_{m\uparrow}^\dagger \hat{d}_{m\downarrow} \hat{d}_{m'\downarrow}^\dagger \hat{d}_{m'\uparrow} = \frac{\hat{\mathbf{S}}^2 - \hat{\mathbf{T}}^2}{2} + \hat{T}_z^2 - \hat{S}_z^2, \quad (6.18d)$$

$$\sum_{m \neq m'} \hat{d}_{m\uparrow}^\dagger \hat{d}_{m\downarrow} \hat{d}_{m'\downarrow}^\dagger \hat{d}_{m'\uparrow} = \hat{T}_x^2 - \hat{T}_y^2. \quad (6.18e)$$

This leads together with the relation $(\hat{N} - 2)^2 + 2\hat{\mathbf{S}}^2 + 2\hat{\mathbf{T}}^2 = 4$ to the interaction part of the e_g Hamiltonian in the form

$$\hat{H}_U = (U - J) \frac{\hat{N}(\hat{N} - 1)}{2} + 2J(\hat{T}_x^2 + \hat{T}_z^2) - J\hat{N}, \quad (6.19)$$

revealing an abelian charge symmetry $U(1)_C$ (due to particle number conservation), a non-abelian spin symmetry $SU(2)_S$ (as the total spin is conserved) and only an $O(2)_O$ orbital symmetry. It is convenient to perform a rotation in the isospin space to exchange y and z . This transformation keeps the hopping to the conduction bands diagonal. We then obtain

$$\hat{H}_U = (U - J) \frac{\hat{N}(\hat{N} - 1)}{2} + 2J(\hat{T}_x^2 - \hat{T}_y^2) - J\hat{N}, \quad (6.20)$$

which results in an interaction Hamiltonian, that does not exhibit any pair hopping between different orbitals (Eq. (6.18e)):

$$\begin{aligned} \hat{H}_U = & (U - J) \sum_m \hat{n}_{m\uparrow} \hat{n}_{m\downarrow} + (U - J) \sum_{m \neq m'} \hat{n}_{m\uparrow} \hat{n}_{m'\downarrow} + (U - 3J) \sum_{m < m'} \hat{n}_{m\sigma} \hat{n}_{m'\sigma} \\ & - 2J \sum_{m \neq m'} \hat{d}_{m\uparrow}^\dagger \hat{d}_{m\downarrow} \hat{d}_{m'\downarrow}^\dagger \hat{d}_{m'\uparrow}. \end{aligned} \quad (6.21)$$

In the following, we want to investigate the two-band Hubbard-Kanamori Hamiltonian with the “rotated” interaction term, to check some of our NRG results explicitly against CT-QMC data, which are again provided by Michel Ferrero. For the NRG implementation, where we can use arbitrary abelian and non-abelian symmetries, it is suggestive to write this version of \hat{H}_U as

$$\hat{H}_U = (U - J) \frac{\hat{N}(\hat{N} - 1)}{2} + 2J\hat{N}_1\hat{N}_2 + \frac{3}{2}J\hat{N} - 2J\hat{S}^2, \quad (6.22)$$

with $\hat{N}_m = \sum_{\sigma} \hat{n}_{m\sigma}$. So we can exploit two abelian charge symmetries $U(1)_C \times U(1)_C$ for the particle number conservation in both bands, respectively, and total spin conservation given by the non-abelian symmetry $SU(2)_S$. However, there is no continuous orbital symmetry, since the orbital angular momentum is quenched for the e_g -bands. We only find a point symmetry between band 1 and 2. In the particle-hole symmetric case, the system does not show a $SU(2)$ particle-hole symmetry, as well. Here, the chemical potential was derived analytically as $\mu = -3/2U + 5/2J$ from the ansatz, that \hat{H}_{imp} in Eq. (6.6a) with $M = 2$ has to be invariant under the transformation $\hat{d}_{m\sigma}^{\dagger} \leftrightarrow \hat{d}_{m\sigma}$, or equivalently $\hat{n}_{m\sigma} \leftrightarrow (1 - \hat{n}_{m\sigma})$. Since point symmetries have not yet been implemented explicitly in the NRG solver, we use $U(1)_C \times U(1)_C \times SU(2)_S$ for our calculations. Further we can reduce numerical effort by performing the DMFT procedure for only one band, as the DMFT loops are decoupled and the point symmetry between orbital 1 and 2 leads to equal spectral functions for both bands.

6.3.2 The effect of Hund’s coupling on the metal-insulator transition (MIT)

Compared with the one-band Hubbard model, more realistic models (like the two-band Hubbard-Kanamori Hamiltonian) account for the fact that beside Coulomb repulsion, more complex intra-atomic exchange processes, mediated by Hund’s rule coupling, influence the physics of strongly correlated materials.

Hund’s rules were already formulated by Friedrich Hund in 1925 to explain the spectra of transition metal atoms [40]. They are based on the minimization of the effective Coulomb repulsion between electrons in the ground state configuration of a single multi-electron atom and regulate the occupancy for N electrons in a shell of orbital degeneracy $M = 2l + 1$, where l denotes the orbital angular momentum quantum number.

The first rule states that the lowest energy electron-configuration is obtained by maximizing the total spin S . As a second rule, the highest value of the total orbital angular momentum L has to be chosen for a given quantum number S . The third rule incorporates spin-orbit coupling. For $N < M$ the total angular momentum quantum number $J = |L - S|$ should be minimal, while for $N > M$, J has to be largest.

In the two-band Hubbard-Kanamori model Hund’s first rule is correctly incorporated by the coupling $U' - J$ (with $U' = U - 2J$ for degenerate orbitals). As depicted in Fig. 6.3 for two electrons per site, Hund’s rule coupling lowers the repulsive Coulomb interaction between electrons placed in different orbitals from $U' = U - 2J$ to $U' - J = U - 3J$, if they show parallel spins. Besides, the Coulomb repulsion U between two electrons, located on one orbital, is naturally larger than the Coulomb repulsion $U' = U - 2J$ for two electrons with spin up and down on different orbitals.

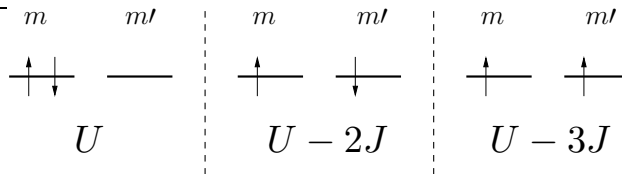


Figure 6.3: Illustration of Hund's first rule for two electrons that are placed on one lattice site with two degenerate orbitals. U denotes the Coulomb repulsion between electrons on one orbital. J is the exchange coupling. Electrons with parallel spins on different sites exhibit the lowest energy due to Hund's first rule. Figure adapted from [10, Chapter 3].

The Hund's rule coupling has a major influence on the physics of strongly correlated materials. An interesting effect is found for the Mott metal-insulator transition (MIT), that occurs in the multi-band case (with preserved orbital degeneracy) for any integer filling of the lattice (zero and complete filling excluded). The critical Coulomb repulsion U_c is strongly reduced with increasing exchange coupling J for a half-filled system ($\langle N \rangle = 2$ for the two-band model). In contrast, in the integer and non-half-filled case ($\langle N \rangle = 1$, $\langle N \rangle = 3$ for the two-band model) U_c increases (linearly) with J . This suggests to regard the filling $\langle N \rangle$ as a control parameter for the critical Coulomb repulsion U_c of the MIT in the presence of Hund's coupling [3].

Similar behavior was discussed for isolated atoms already in the late 1980's. In [41] D. Van der Marel and G.A. Sawatzky revealed that Hund's coupling leads to an increased effective Coulomb repulsion for half-filled shells. For all other average occupancies the effective Coulomb repulsion is lowered. Remarkably, these effects also show up in the solid state context, where the bandwidth is much larger than the Hund's coupling [3].

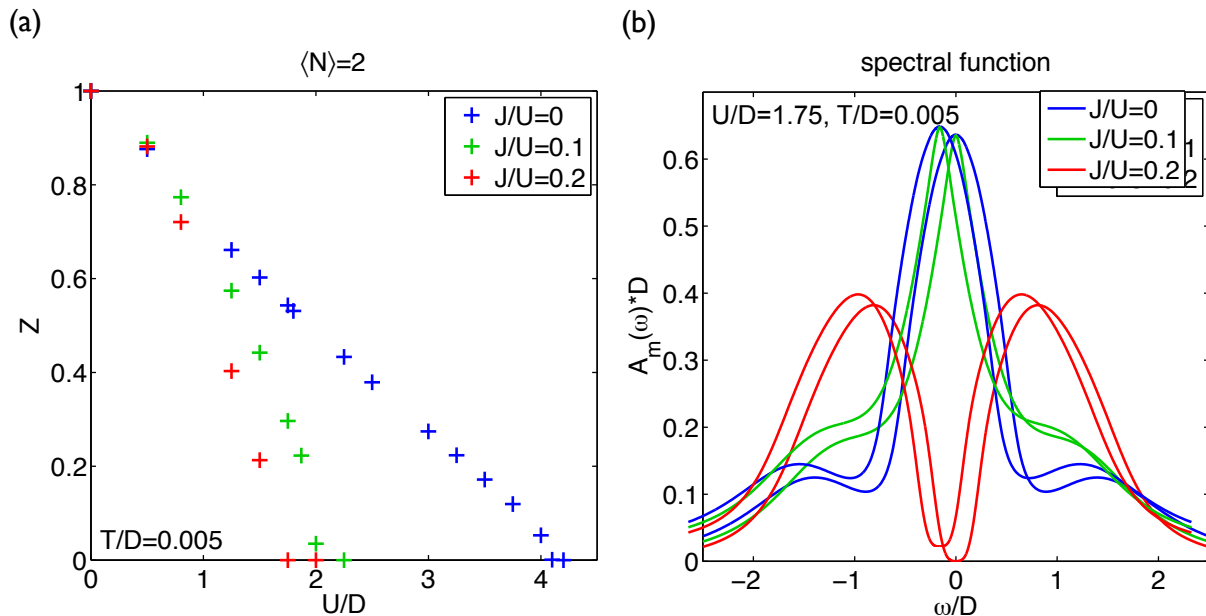


Figure 6.4: Panel (a) shows the quasiparticle weight for different values of J/U as a function of the Coulomb repulsion U at half filling. U_c decreases for increasing relative exchange coupling J/U . In panel (b) we plotted the spectral functions for a fixed Coulomb repulsion $U/D = 1.75$ and different values of J . With increasing J we observe a transition from the metallic to the insulating phase for $\langle N \rangle = 2$.

In the following, we demonstrate the effect of Hund's coupling on the (paramagnetic) MIT for the half-filled ($\langle N \rangle = 2$) and the quarter-filled ($\langle N \rangle = 1$) case, using the two-band Hubbard-Kanamori model of Eq. (6.14). As discussed before, we apply $\Lambda = 4$ and z-averaging with $N_z = 4$. Further, the broadening parameter is $\sigma = 0.5$ and $N_{\max} \approx 25$ in most calculations. To reduce the state space within NRG, we implement $U(1)_C \times U(1)_C \times SU(2)_S$ symmetries. Nevertheless, we have to keep up to 12000 multiplets (≈ 34000 states) in early NRG iterations to reach a discarded weight of about 10^{-12} . At later iterations this number drastically decreases to about 600 kept multiplets. Here the implementation of the orbital point symmetry would help to halve numerical effort.

In [19] Th. Pruschke and R. Bulla report to keep $\mathcal{O}(7000)$ states in each NRG iteration, in [21] R. Peters, N. Kawakami and Th. Pruschke use 4000-5000 states per NRG iteration with a discretization parameter $\Lambda = 2$. Note however that the pair hopping term (which is the last term in Eq. (6.1b)) was explicitly omitted in these studies to exploit that the orbital occupation is conserved [19].

In Fig. 6.4 (a) we plot the quasiparticle weight as a measure of the ‘‘degree of correlations’’ for different values of J/U as a function of the Coulomb repulsion U for the half-filled case. As pointed out in [3] (for the three-band Hubbard-Kanamori model), it is convenient to concentrate on fixed values of J/U . Further this choice is set in accordance with the QMC data of Michel Ferrero (see Sec. 6.3.3). It can be clearly observed that U_c (minimum of $U(Z = 0)$) decreases for increasing relative exchange coupling J/U . While for $J/U = 0$, U_c is slightly larger than 4, U_c lies slightly above 2 for $J/U = 0.1$ and below 1.75 for $J/U = 0.2$.

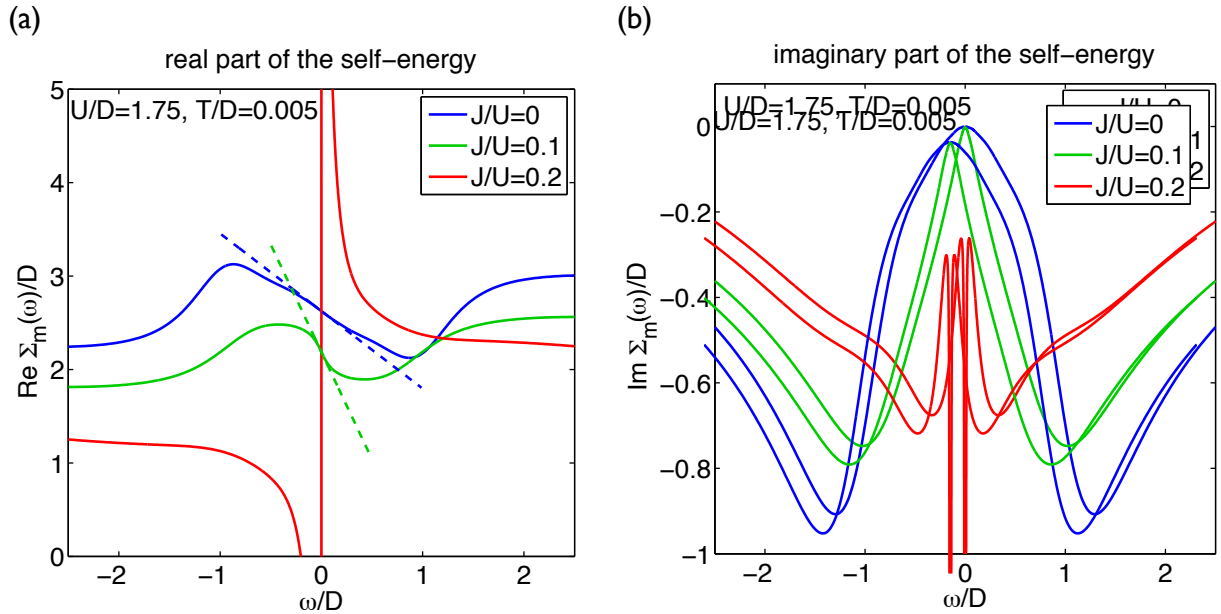


Figure 6.5: In panel (a) we depict the real part of the self-energy for each spectral function of Fig. 6.4 (b). Further, the slope at the Fermi level is shown for $J/U = 0$ and $J/U = 0.1$ (dashed lines). Panel (b) contains the imaginary parts. Note that the δ -peak of the red curve is expected to start at around $\text{Im } \Sigma(\omega) = 0$. Obviously, some sharp structures near the MIT are badly resolved (see also Fig. 6.6 (b)). This might be attributed to a small N_z with a large value of Λ and relatively large broadening parameter. For the first iterations we used $N_z = 1$ and $\sigma = 0.8$.

In Fig. 6.4 (b) we show the spectral function for a fixed Coulomb repulsion $U/D = 1.75$ and different values of J . Again the influence of an increasing exchange coupling J is demonstrated. In the half filled case the system is driven into the Mott insulating state. While a quasiparticle peak exists between the two Hubbard bands for $J/U = 0$, indicating a metallic phase, we find an insulator for $J/U = 0.2$. This can be confirmed by investigating the real part of the self-energy in Fig. 6.5 (a), where we show the slope at the Fermi level (dashed lines) for $J/U = 0$ and $J/U = 0.1$, which is directly connected to the quasiparticle weight via Eq. (5.8). A larger slope denotes a smaller quasiparticle weight. For $J/U = 0.2$ (red curve) the slope diverges, leading to $Z = 0$ and thus to an insulating phase. As already discussed for the MIT of the one-band Hubbard model, the metallic phase is further associated with two peaks in the imaginary part of the self-energy (see blue curve in Fig.6.5 (b)), that approach for increasing J (green curve in Fig.6.5 (b)) and finally merge to a single δ -peak in the insulating phase (red curve in Fig.6.5 (b)).

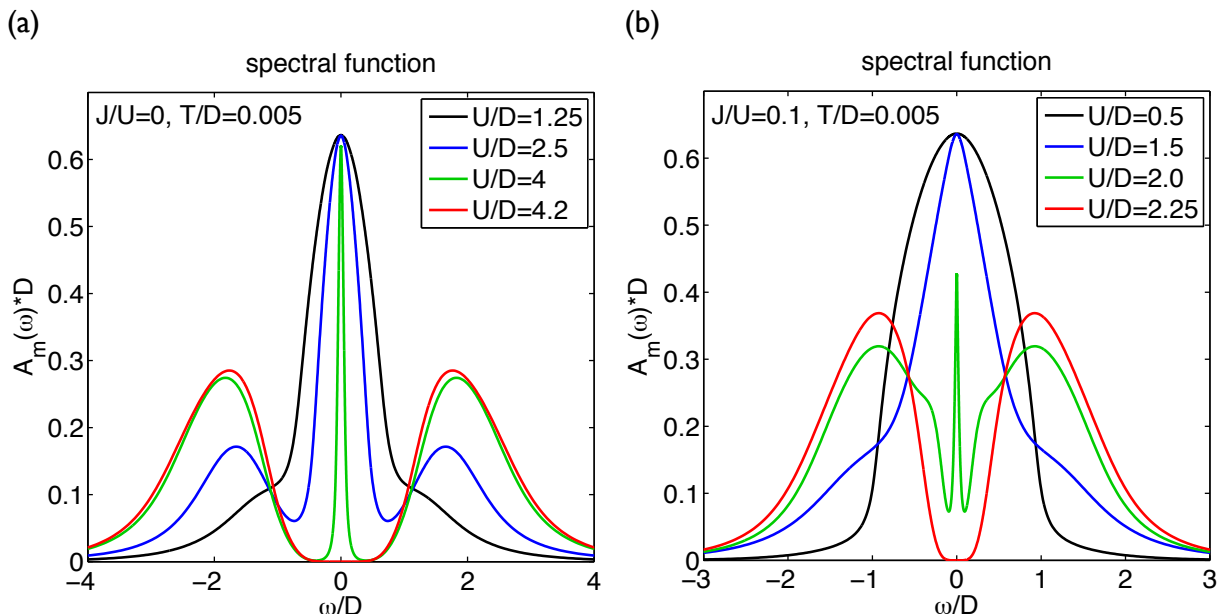


Figure 6.6: Panel (a) displays the MIT for $J/U = 0$, panel (b) for $J/U = 0.1$ (at half-filling). Clearly, the quasiparticle peak vanishes in both cases with increasing U . The sharp structure in the green curve in panel (b) is badly resolved. Presumably due to numerical DMFT+NRG related issues, the peak height is reduced and the expected gaps next to the central peak cannot be observed (see discussion in the caption of Fig. 6.5).

Beside the J -dependence of the MIT, we also show the transition for fixed J/U . In Fig. 6.6 (a) spectral functions for three different values of U are depicted for $J/U = 0$. In the metallic phase we can clearly observe the continuously vanishing quasiparticle weight for the central peak in the spectral function, finally resulting in a gap around the Fermi level for the insulating phase - a behavior that is similarly observed in the one-band Hubbard model. However the energy scale U_c of the MIT is strongly increased compared to the one-band case. While $U_c/D = 2.93$ for the one-band Hubbard Hamiltonian, we obtain a critical Coulomb repulsion of about $U_c/D = 4.2$ in the two-band case, which is in good agreement with the values reported in the literature (e.g $U_c/D \lesssim 4$ in [42] and $U_c/D \approx 5$ in [43], while U_c appears to be overestimated by the NRG studies of Th. Pruschke and R. Bulla with $U_c/D \approx 6$ in [19]).

For $J = 0$ the critical Coulomb repulsion is a function of orbital degeneracy (M) and approximately given by $U_c(J = 0) \sim M$ for a transition from the metallic to the insulating phase [44]. This relation can be associated with enhanced orbital fluctuations, that occur for an increased number of bands, and promote hopping processes, thus contributing to a larger kinetic energy [3]. As the MIT arises for an effective Coulomb repulsion that is in the order of the kinetic energy, U_c effectively grows with M .

The MIT for finite exchange coupling $J/U = 0.1$ is shown in Fig. 6.6 (b). The transition now emerges for a critical value $U_c/D \approx 2.1$, that is even smaller than in the one-band Hubbard model. For finite J the orbital fluctuations are quenched. Therefore, many hopping processes are blocked, which results in a smaller effective kinetic energy and accordingly lower U_c [3].

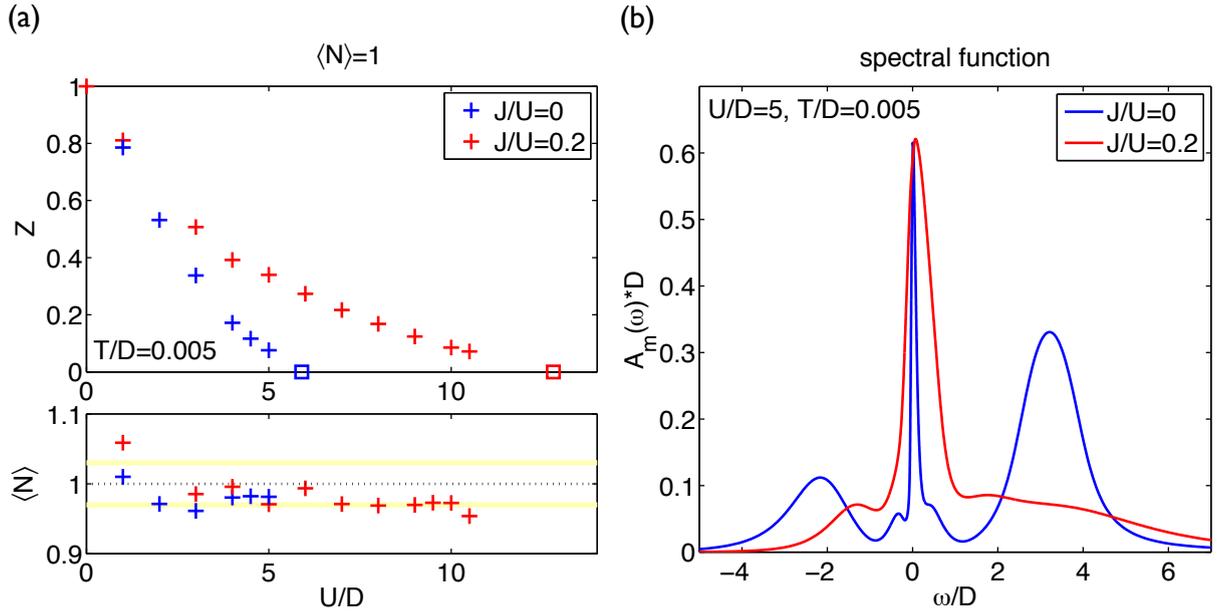


Figure 6.7: In the upper panel (a) we plotted the quasiparticle weight for different values of J/U in dependence of the Coulomb repulsion U for quarter-filling $\langle N \rangle = 1$. In contrast to the half-filled case in Fig. 6.4, U_c increases for increasing relative exchange coupling J/U . Note that the squares are received by interpolation and not by direct calculations (see main text for details). While the chemical potential can be determined analytically for a particle-hole symmetric system, it has to be specified numerically for each value of U , if $\langle N \rangle \neq 2$. The lower panel (a) shows the filling $\langle N \rangle$ in dependence of U as obtained within the DMFT+NRG calculations. All values of μ within the area, bordered by the two horizontal yellow bars, deviate less than 3% from quarter filling $\langle N \rangle = 1$. In panel (b) we depict the spectral functions for a fixed Coulomb repulsion $U/D = 5$ and different values of J . We clearly observe a reduction of the quasiparticle width with decreasing J for $\langle N \rangle = 1$. The bump at around $\omega/D = 0.3$ at finite $J/U = 0.2$ (blue curve) is also found at quarter filling and for finite J in the DMFT+NRG calculations of [21] and is likely NRG related.

The strong reduction of U_c with increasing Hund's coupling J at half filling has been investigated already since the late 1990's, including the NRG studies by Th. Pruschke and R. Bulla 2005 [19]. The non-half filled two-band Hubbard-Kanamori model features an opposite trend for the critical U_c . In Fig. 6.7 (a) we plotted the quasiparticle weight versus U for different fixed values

of J/U to demonstrate that U_c increases with growing Hund's coupling J for the quarter filled case $\langle N \rangle = 1$. While $U_c/D \approx 6$ for $J/U = 0$, we obtain a larger value $U_c/D \approx 13$ for $J/U = 0.2$. For the integer filling $\langle N \rangle = 1$ (and analogously $\langle N \rangle = 3$), the dominant effect on U_c is the reduction of the effective Coulomb energy with increasing J , leading to higher values of U_c . Orbital blocking does not apply in this case [3].

Note that the last value of Z plotted in the upper panel of Fig. 6.7 (a) is obtained via interpolation. While the chemical potential is given analytically ($\mu = -3/2U + 5/2J$) for the half-filled case, we have to determine μ numerically for each value of U in the asymmetric case. This is done in the following way. We start with an "educated" guess for μ and obtain, via DMFT+NRG calculations, the corresponding filling, which may deviate from $\langle N \rangle = 1$. Then a new chemical potential is defined by interpolation, using all known values of μ and $\langle N \rangle$ (including $\mu = -3/2U + 5/2J$ for $\langle N \rangle = 2$). The next DMFT+NRG run results in a new data point $(\mu, \langle N \rangle)$, which can be included to improve the interpolation procedure. After several steps, we may arrive at quarter filling. The lower panel of Fig. 6.7 (a) shows to what accuracy we have reached $\langle N \rangle = 1$. Whereas this method turned out to work quite reliably in the metallic phase, we run into difficulties near the MIT and in the isolating phase. Here, the spectral function differs strongly between consecutive DMFT iterations and we can observe oscillations in the occupation number of the NRG impurity site. As reported in [20] and [21], the insulating phase is accompanied by antiferro-orbital order for small Hund's coupling J and large repulsive interorbital density-density interaction U' at small temperatures. Then, the lattice yields a Néel type bipartite AB structure, breaking translational symmetry. In all probability, we are not able to stabilize the insulating phase within our DMFT+NRG calculations, as this phase is not commensurate to the lattice structure in our DMFT setting.

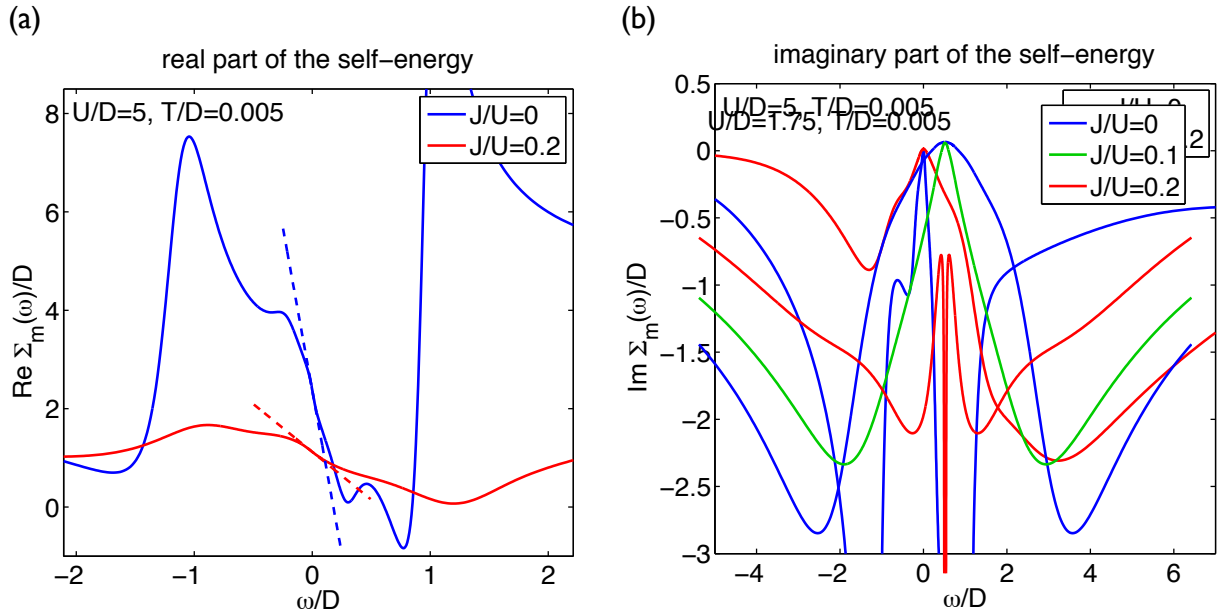


Figure 6.8: In panel (a) we depict the real parts of the self-energy, corresponding to the spectral functions in Fig. 6.7 (b). Further, the slope at the Fermi level is shown (dashed lines). Panel (b) contains the imaginary parts.

Nevertheless, we can observe the influence of Hund's coupling in the metallic phase, which is also revealed by the spectral functions in Fig. 6.7 (b) for a fixed Coulomb repulsion $U/D = 5$ and different values of J/U . The corresponding real and imaginary parts of the self-energies are shown in Fig. 6.8 (a) and (b).

To summarize, we have investigated the effect of Hund's rule coupling on the MIT of the two-band Hubbard-Kanamori model. We reproduced that for half filling ($\langle N \rangle = 2$) the Mott critical coupling U_c strongly decreases with increasing Hund's coupling J , resulting in a more correlated system. Note that another important aspect for the half-filled case has not been studied in this work. Hund's coupling also suppresses the coherence scale below which Fermi-liquid physics applies [3]. In contrast, for quarter filling ($\langle N \rangle = 1$), U_c increases with larger exchange coupling J , leading to a less correlated system. As reported in [20] and [21], a rich phase diagram exists at quarter filling with different types of ordered phases at low temperatures and a paramagnetic MIT at high temperatures.

An even more complex behavior was revealed in 2011 [45] for the three-band Hubbard-Kanamori model in the case of three degenerate partially filled t_{2g} -bands. The three-band model currently attracts much attention due to its relevance for recently discovered iron-based superconductors. Here the Hamiltonian exhibits a $U(1)_C \times SU(2)_S \times SU(2)_O$ symmetry:

$$\hat{H}_U = (U - 3J) \frac{\hat{N}(\hat{N} - 1)}{2} - 2J\hat{S}^2 - \frac{1}{2}J\hat{L}^2 + \frac{5}{2}J\hat{N}, \quad (6.23)$$

with the total spin and charge operators as in Eq. (6.16) and Eq. (6.17) (now with $m = 1, 2, 3$), respectively, and the orbital isospin generators

$$\hat{L}_m = i \sum_{m'm''\sigma} \epsilon_{mm'm''} \hat{d}_{m'\sigma}^\dagger \hat{d}_{m''\sigma}. \quad (6.24)$$

Note that $U' = U - 2J$ was used to derive Eq. (6.23) [3]. While similar effects to the two-band case are observed for half filling and single occupancy ($\langle N \rangle = 1$ and $\langle N \rangle = 5$), a ‘‘Janus-faced’’ influence of Hund's coupling is discussed for $\langle N \rangle = 2$ and $\langle N \rangle = 4$. On the one-hand, U_c is enhanced by Hund's coupling, driving the system away from the Mott insulating phase. On the other hand, the quasiparticle coherence scale is reduced at the same time, leading to a more correlated system. Above the Fermi liquid temperature T_{FL} , a non Fermi liquid state, associated with frozen local moments and a power-law behavior for the self-energy, is reported, for which a precise theoretical understanding is still missing [3]. Among others, further open questions (for the t_{2g} -system) concern the importance of Hund's coupling for stabilizing ferromagnetism, Hund's coupling in the presence of spin-orbit coupling (as in 4d and 5d transition metal oxides) and its role in superconductivity (see the review of A. Georges, L. de' Medici and J. Mravlje [3] for detailed discussions).

6.3.3 Comparison of NRG and Quantum Monte Carlo results

Beside the discussion of the MIT in the presence of Hund's coupling, we now want to check our DMFT+NRG results directly against DMFT+CT-QMC data provided by Michel Ferrero (and denoted by MF in the plots).

In the following, we concentrate on a fixed value $J/U = 1/6$ at three different temperatures $T/D = 0.0025$, $T/D = 0.01$ and $T/D = 0.02$. $U/D = 1.6$ is chosen for the particle-hole symmetric case ($\langle N \rangle = 2$) and $U/D = 3.8$ for quarter filling ($\langle N \rangle = 1$). The spectral functions

for $\langle N \rangle = 2$ are plotted in Fig. 6.9 (a). The solid lines denote our NRG results. The dashed lines are QMC results, which are analytically continued from the imaginary (Matsubara) frequencies to the real frequency axis via the maximum entropy approach (maxEnt). Note that we did not receive any QMC data on the real frequency axis for the smallest of the three given temperatures $T/D = 0.0025$.

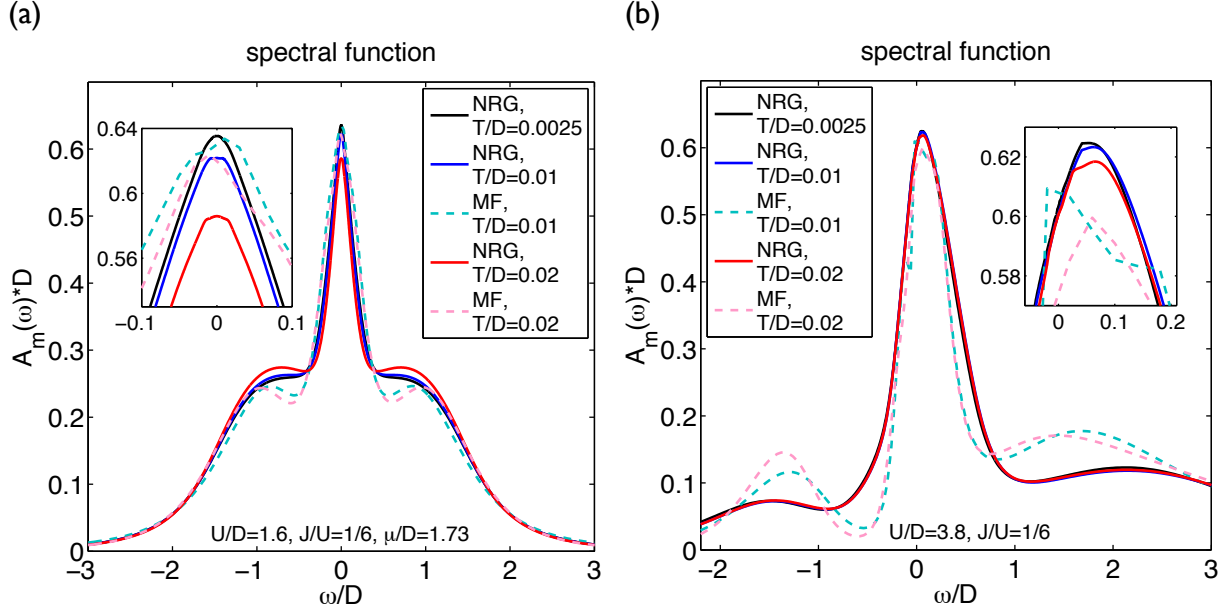


Figure 6.9: Spectral functions for a fixed value $J/U = 1/6$ at three different temperatures $T/D = 0.0025$, $T/D = 0.01$ and $T/D = 0.02$. Solid curves are NRG results, dashed curves denote CT-QMC results by Michel Ferrero (MF), that are analytically continued to the real axis via the maximum entropy approach (maxEnt). In panel (a) we show curves for the particle-hole symmetric case $\langle N \rangle = 2$ with $U/D = 1.6$, in panel (b) for the asymmetric case $\langle N \rangle = 1$, where we have used $U/D = 3.8$.

As can be observed in the inset of Fig. 6.9 (a) and especially for the asymmetric spectral functions in the inset of Fig. 6.9 (b), the maxEnt-results should be treated with some caution and serve as qualitative check. In both the symmetric and asymmetric case, we obtain essentially equal spectral functions, which show Hubbard bands at similar positions and quasiparticle peaks with widths, that are in the order of the maxEnt quasiparticle peak widths. Note that the exact shape of the Hubbard bands should not be taken too seriously in either case, since the maxEnt method as well as NRG is not very exact for high frequencies. For the NRG results, the curves are smeared out due to a large broadening parameter ($\sigma = 0.5$ for $N_z = 4$). At frequencies around the Fermi level (insets of Fig. 6.9), the NRG data appear to be more reliable than the QMC data, in principle.

For a quantitative comparison, we use the CT-QMC data on the original imaginary (Matsubara) axis. At the Fermi level $\omega = 0$, the NRG self-energy $\Sigma_m(\omega = 0, T)$ should be equal to the QMC self-energy $\Sigma_m(i\omega_n = 0, T)$, with the Matsubara frequencies $\omega_n = \frac{(2n+1)\pi}{\beta}$ and the integer n . So, we plot the real and imaginary parts of the self-energy for the NRG and the QMC data, respectively (see Fig. 6.10 for the real and Fig. 6.11 for the imaginary part of the self-energy). In Fig. 6.10 (a), where we show the real part of the self-energy for $\langle N \rangle = 2$ (solid curves for NRG on the real frequency axis and circles for QMC on the imaginary Matsubara frequency axis), we

can observe that $\text{Re} \Sigma_m(\omega = 0, T) = \mu = -3/2U + 5/2J = 1.73D = \text{Re} \Sigma_m(i\omega_n = 0, T)$, which is fulfilled by construction for the particle-hole symmetric case. Fig. 6.10 (b) depicts the real parts of the self-energies for quarter filling. Here, the chemical potential is not given analytically. In contrast to the results in the previous section, where the chemical potentials have been calculated numerically within the DMFT+NRG procedure, we applied the same chemical potentials, as used for the CT-QMC results by Michel Ferrero, for the figures shown in this section. However, the expected filling of $\langle N \rangle = 1$ is only reached up to 10%. This discrepancy may be a reason for the deviations observed in Fig. 6.10 (b). The values of $\text{Re} \Sigma_m(\omega = 0, T)$ seem to be shifted downwards compared to $\text{Re} \Sigma_m(i\omega_n = 0, T)$. The curves for $T/D = 0.01$ and $T/D = 0.02$ lie nearly on top of each other, while the value for $T/D = 0.0025$ is slightly larger for either the NRG and QMC case.

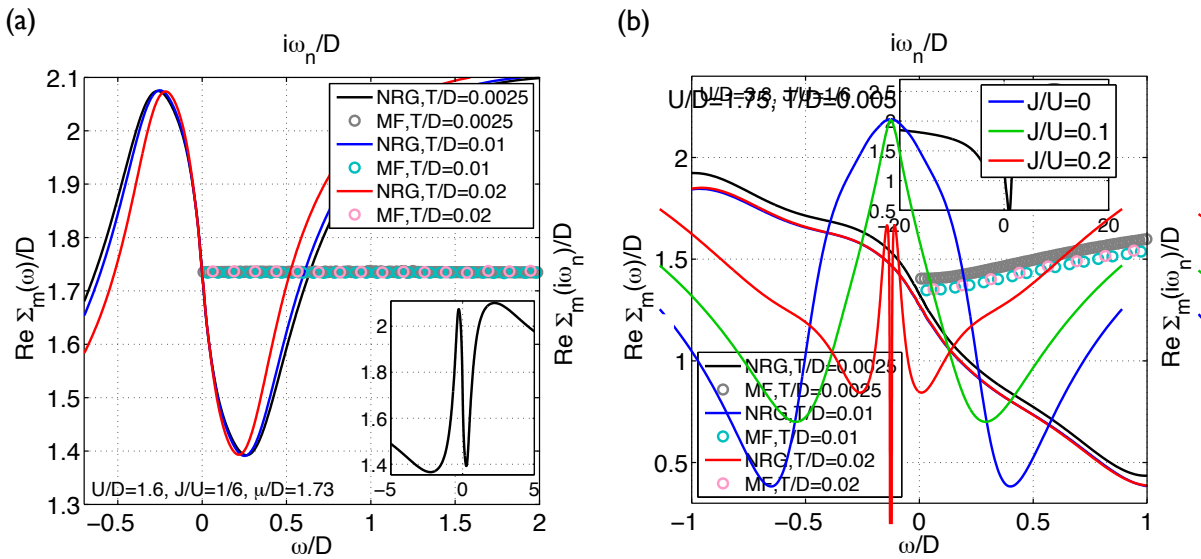


Figure 6.10: Real part of the self-energy for the spectral functions, shown in Fig. 6.9. In panel (a) we plotted the NRG (real-frequency axis) and CT-QMC (imaginary, i.e. Matsubara frequency axis) results from Michel Ferrero (labeled by MF) for the particle-hole symmetric case $\langle N \rangle = 2$ with $U/D = 1.6$, in panel (b) for the asymmetric case $\langle N \rangle = 1$, where we have used $U/D = 3.8$. Note that the axes labeling is on top and to the right for the QMC-data (circles). The insets illustrate a larger section of the real part of the NRG self-energy for $T/D = 0.0025$.

We can also compare the imaginary parts of the self-energies at the Fermi level. While the NRG results are indicated by the solid curves in Fig. 6.10, the QMC data are denoted by the circles. $\text{Im} \Sigma_m(i\omega_n = 0, T)$ is determined by a polynomial fit (of order 2, including the first 5-9 data points). The colored vertical bars are corresponding error bars for the fits (dashed curves). In Fig. 6.10 (a) we concentrate on half-filling $\langle N \rangle = 2$. Within the error margins, the NRG results are in agreement with the QMC data. However, the NRG curve for $T/D = 0.02$ and also for $T/D = 0.01$ show an unusual flat top. Note also that the method to determine $\text{Im} \Sigma_m(i\omega_n = 0, T)$ features rather large error margins. In Panel (b) of Fig. 6.10 we compare the imaginary parts of the self-energy at $\omega = 0$ at quarter filling. In this case, it is rather hard to evaluate the accuracy of our results, as the values of the imaginary parts of the self-energy are very close to each other for the different temperatures and the deviation of the filling factor

of about 10% is much too large. Note that we also performed calculations with a numerically determined filling factor with an accuracy of less than 3%. In that case however, the obtained chemical potentials and the values for the self-energy at the Fermi level differ even more from the CT-QMC data. At the present stage, it is not clarified how to judge these deviations. Possibly, the DMFT+NRG calculation have to be further optimized.

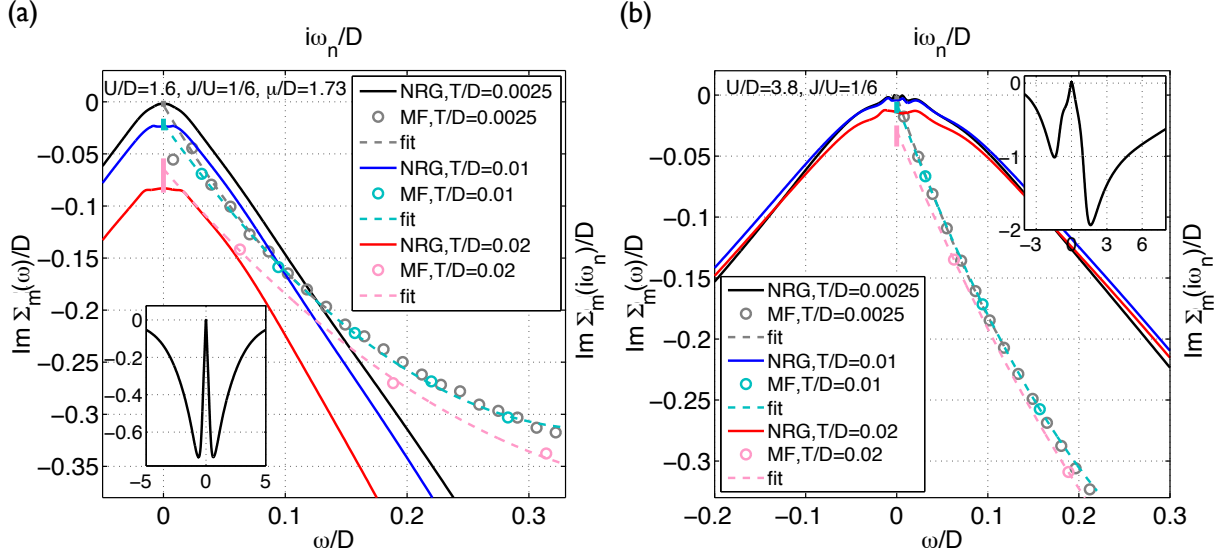


Figure 6.11: Imaginary part of the self-energy for the spectral functions, shown in Fig. 6.9. In panel (a) we plotted the NRG (real-frequency axis) and CT-QMC (imaginary, i.e. Matsubara frequency axis) results from Michel Ferrero (labeled by MF) for the particle-hole symmetric case $\langle N \rangle = 2$ with $U/D = 1.6$, in panel (b) for the asymmetric case $\langle N \rangle = 1$, where we have used $U/D = 3.8$. Note that the axes labeling is on top and to the right for the QMC-data (circles). The dashed curves are polynomial fits for the QMC results with the vertical bars as error margins. The insets illustrate a larger section of the imaginary part of the NRG self-energy for $T/D = 0.0025$.

Altogether, we conclude that our NRG results can be trusted also quantitatively for the half-filled case, while we have to clarify the origin of stronger deviations for quarter filling. However, these DMFT+NRG calculations are first results and there is a range of possibilities for further improvements, such as an adaptive grid, the inclusion of point symmetries, but also smaller discretization Λ and broadening σ with larger N_z . Nevertheless, it is a clear advantage of the NRG method to produce results on the real frequency axis, as the analytical continuation of QMC data from the imaginary to the real frequency axis may become difficult and less reliable for more-band models especially for low temperatures, as could be observed in a direct comparison of the spectral functions in Fig. 6.9.

Chapter 7

Conclusion and Outlook

In this thesis, we introduced the highly evolved and competitive Numerical Renormalization Group program of Andreas Weichselbaum as a solver for the effective quantum impurity problem within the Dynamical Mean-Field Theory in order to solve model Hamiltonians of strongly correlated materials.

Especially multi-band models, partly combined with realistic band structure calculations (LDA), are in the focus of research in the field of DMFT. In this context, our NRG program, being the first one to exploit arbitrary abelian and non-abelian symmetries, may contribute in particular to the investigation of models with high symmetries in the future. In general, using NRG, we are able to provide data on the real frequency axis, which is a clear advantage against the widely used Quantum Monte Carlo approach that works on the imaginary frequency axis.

Nevertheless, the combination of DMFT+NRG yields its own difficulties. We demonstrated, that the conventional logarithmic discretization grid of NRG is not optimal for an application within DMFT. As the hybridization function is frequency-dependent and varies during the DMFT procedure, the basic NRG assumption of energy scale separation is no longer strictly guaranteed, particularly for early NRG iterations. This can be detrimental for the numerical calculation, since a lot more states have to be kept to achieve converged NRG results. In order to reduce this problem, we introduced an altered discretization scheme with an adjusted outer interval. Although based on heuristic grounds, this grid provided solid results. Nevertheless, for future studies, it is advisable to further concentrate on the adaptive logarithmic discretization as suggested in [27]. The related issue of how to broaden the discrete NRG data may be overcome by using a recently published method based on Padé approximants [46]. Another problem is posed by the slight overestimation of the self-energy within NRG, which can lead to a violation of causality during the DMFT iterations for very low temperatures. This was fixed by a manual small change of the self-energy within the DMFT procedure and a redefinition of the zero energy point for the final results (see Sec. 5.3). This procedure turned out to be quite stable and to yield surprisingly accurate results (as demonstrated for the asymmetric one-band Hubbard model). In principle, the overestimation can be downsized by increasing numerical effort like keeping more states within the NRG calculations. However, this is only feasible to a limited extent, especially for more complex systems, and can not completely resolve the problem. Possibly, the slight systematic overestimation of the self-energy may be reduced by a more appropriate discretization and broadening technique. While this issue is of particular relevance for the determination of small energy scales, such as the Fermi liquid temperature, it is, in general, less adverse for the investigation of phase transitions.

Despite these difficulties, we were able to reliably reproduce the MIT for the particle-hole symmetric one-band Hubbard model and obtained quite accurate results for the hole-doped case, investigated in [6]. Besides, we also performed extended preliminary studies for a two-band model, the two-band Hubbard-Kanamori Hamiltonian. The effect of Hund's coupling on the MIT for half and quarter filling of the system could be revealed as known from literature. When compared to QMC data, that have been analytically continued to the real frequency axis, the NRG results appear more solid. However, compared to QMC data on the imaginary (Matsubara) axis in the extrapolated limit $\omega \rightarrow 0$, the accuracy of our NRG results has to be further advanced on a quantitative level. As such the two-band calculations constitute a first test run with several options for improvements. Besides, more direct comparisons to high-quality QMC data (mainly on the Matsubara axis) are needed for a reliable evaluation of our NRG results.

Apart from technical upgrades like the implementation of an adaptive grid with appropriate broadening, possible future projects are linked to multi-band models with high symmetries, such as the three-band model presented at the end of Sec. 6.3.2. A quite general multi-band Hamiltonian in that respect is suggested in the appendix of [3].

Of specific further interest are realistic calculations for nickelate heterostructures. Heterostructuring of transition metals is a recent topic, as electronic structures, analogous to that of high temperature cuprate superconductors, appear to be within reach. In this case, a two-band model similar to the one studied in Chapter 6, but with off-diagonal hybridization matrix elements, has to be investigated. Due to the off-diagonal hybridization matrix elements, a fundamental "sign-problem" emerges for Quantum Monte Carlo techniques [47]. Thus alternative approaches, like the Numerical Renormalization Group, are required.

Appendix A

Equation of motion for the retarded Green's function

For a general retarded Green's function

$$G_{\hat{A}\hat{B}}(t) = \langle \hat{A} \| \hat{B} \rangle_t = -i\Theta(t) \underbrace{\langle \{\hat{A}(t), \hat{B}(0)\} \rangle_T}_{\text{Tr}(\rho\{\hat{A}, \hat{B}\})} \quad (\text{A.1})$$

with fermionic operators \hat{A} and \hat{B} , we can derive an equation of motion in the Heisenberg picture. The time evolution of an operator $\hat{A}(t) = e^{i\hat{H}t} \hat{A} e^{-i\hat{H}t}$ can be expressed as a linear differential equation

$$\frac{d}{dt} \hat{A}(t) = \frac{i}{\hbar} [\hat{H}, \hat{A}](t). \quad (\text{A.2})$$

\hbar is set to 1 in the following. With Eq. (A.2) the time derivative of the retarded Green's function reads

$$\frac{d}{dt} G_{\hat{A}\hat{B}}(t) = -i\delta(t) \langle \{\hat{A}(0), \hat{B}(0)\} \rangle_T - i\Theta(t) \langle \{i[\hat{H}, \hat{A}](t), \hat{B}(0)\} \rangle_T. \quad (\text{A.3})$$

Fourier transformation of the above expression leads to the equation of motion

$$\omega G_{\hat{A}\hat{B}}(\omega) = \langle \{\hat{A}, \hat{B}\} \rangle_T - G_{[i\hat{H}, \hat{A}]\hat{B}}(\omega), \quad (\text{A.4})$$

where ω has been analytically continued to the upper half plane $\omega^+ \equiv \omega + i\delta$ with the positive infinitesimal δ to account for causality of the retarded Green's function. For convenience we only write ω instead of ω^+ .

Appendix B

$G_{\text{latt}}(\omega)$ for a multi-band model

We derive a matrix expression for the lattice Green's function $G_{\text{latt},\mathbf{k}}^{\mu\nu}(\omega) = \langle \hat{c}_{\mathbf{k}\mu} \| \hat{c}_{\mathbf{k}\nu}^\dagger \rangle_\omega$ of a multi-band Hubbard-Kanamori model,

$$\hat{H} = \underbrace{\sum_{\tilde{\mathbf{k}}\tilde{\mu}} (-\mu_{\tilde{\mu}}) \hat{c}_{\tilde{\mathbf{k}}\tilde{\mu}}^\dagger \hat{c}_{\tilde{\mathbf{k}}\tilde{\mu}}}_{\hat{H}^0} + \sum_{\tilde{\mathbf{k}}\tilde{\mu}\tilde{\nu}} \varepsilon_{\tilde{\mathbf{k}}}^{\tilde{\mu}\tilde{\nu}} \hat{c}_{\tilde{\mathbf{k}}\tilde{\mu}}^\dagger \hat{c}_{\tilde{\mathbf{k}}\tilde{\nu}} + \sum_i (\hat{H}_U)_i, \quad (\text{B.1})$$

with the non-interacting part of the Hamiltonian \hat{H}^0 and an arbitrary local interaction term $(\hat{H}_U)_i$, kept in its spatial representation. The greek letters label different orbital ($m = 1, 2, \dots, M$) and spin ($\sigma = \uparrow, \downarrow$) indices : $\mu = \{m\sigma\}$.

Starting from the equation of motion Eq. (A.3) for the non-interacting lattice Green's function $G_{\text{latt},\mathbf{k}}^{0,\mu\nu} = \langle \hat{c}_{\mathbf{k}\mu} \| \hat{c}_{\mathbf{k}\nu}^\dagger \rangle_t^0$,

$$i \frac{d}{dt} \langle \hat{c}_{\mathbf{k}\mu} \| \hat{c}_{\mathbf{k}\nu}^\dagger \rangle_t^0 = \delta(t) \langle \{ \hat{c}_{\mathbf{k}\mu}, \hat{c}_{\mathbf{k}\nu}^\dagger \} \rangle_T + i\Theta(t) \langle \{ [\hat{H}^0, \hat{c}_{\mathbf{k}\mu}], \hat{c}_{\mathbf{k}\nu}^\dagger \} \rangle_T, \quad (\text{B.2})$$

and using

$$\{ \hat{c}_{\mathbf{k}\mu}, \hat{c}_{\mathbf{k}\nu}^\dagger \} = \delta_{\mu\nu} \quad (\text{B.2a})$$

and

$$[\hat{H}^0, \hat{c}_{\mathbf{k}\mu}] = \sum_{\tilde{\mathbf{k}}\tilde{\mu}} (-\mu_{\tilde{\mu}}) \underbrace{[\hat{c}_{\tilde{\mathbf{k}}\tilde{\mu}}^\dagger \hat{c}_{\tilde{\mathbf{k}}\tilde{\mu}}, \hat{c}_{\mathbf{k}\mu}]}_{-\delta_{\tilde{\mu}\mu} \delta_{\tilde{\mathbf{k}}\mathbf{k}} \hat{c}_{\tilde{\mathbf{k}}\tilde{\mu}}} + \sum_{\tilde{\mathbf{k}}\tilde{\mu}\tilde{\nu}} \varepsilon_{\tilde{\mathbf{k}}}^{\tilde{\mu}\tilde{\nu}} \underbrace{[\hat{c}_{\tilde{\mathbf{k}}\tilde{\mu}}^\dagger \hat{c}_{\tilde{\mathbf{k}}\tilde{\nu}}, \hat{c}_{\mathbf{k}\mu}]}_{-\delta_{\tilde{\mu}\mu} \delta_{\tilde{\mathbf{k}}\mathbf{k}} \hat{c}_{\tilde{\mathbf{k}}\tilde{\nu}}}, \quad (\text{B.2b})$$

we obtain

$$i \frac{d}{dt} \langle \hat{c}_{\mathbf{k}\mu} \| \hat{c}_{\mathbf{k}\nu}^\dagger \rangle_t^0 = \delta(t) \delta_{\mu\nu} + i\Theta(t) \mu_\mu \langle \{ \hat{c}_{\mathbf{k}\mu}, \hat{c}_{\mathbf{k}\nu}^\dagger \} \rangle_T - i\Theta(t) \sum_{\tilde{\nu}} \varepsilon_{\tilde{\mathbf{k}}}^{\mu\tilde{\nu}} \langle \{ \hat{c}_{\mathbf{k}\tilde{\nu}}, \hat{c}_{\mathbf{k}\nu}^\dagger \} \rangle_T \quad (\text{B.3a})$$

$$= \delta(t) \delta_{\mu\nu} - \mu_\mu \langle \hat{c}_{\mathbf{k}\mu} \| \hat{c}_{\mathbf{k}\nu}^\dagger \rangle_t^0 + \sum_{\tilde{\nu}} \varepsilon_{\tilde{\mathbf{k}}}^{\mu\tilde{\nu}} \langle \hat{c}_{\mathbf{k}\tilde{\nu}} \| \hat{c}_{\mathbf{k}\nu}^\dagger \rangle_t^0, \quad (\text{B.3b})$$

which can be compactly written as

$$\sum_{\tilde{\nu}} [(i \frac{d}{dt} + \mu_\mu) \delta_{\mu\tilde{\nu}} - \varepsilon_{\tilde{\mathbf{k}}}^{\mu\tilde{\nu}}] \langle \hat{c}_{\mathbf{k}\tilde{\nu}} \| \hat{c}_{\mathbf{k}\nu}^\dagger \rangle_t^0 = \delta(t) \delta_{\mu\nu}. \quad (\text{B.3c})$$

Fourier transformation then leads to

$$\sum_{\tilde{\nu}} [(\omega + \mu_{\mu})\delta_{\mu\tilde{\nu}} - \varepsilon_{\mathbf{k}}^{\mu\tilde{\nu}}] \langle \hat{c}_{\mathbf{k}\tilde{\nu}} \| \hat{c}_{\mathbf{k}\nu}^{\dagger} \rangle_{\omega}^0 = \delta_{\mu\nu}, \quad (\text{B.4})$$

or equivalently in matrix notation

$$[(\omega + \mu_{\mu})\mathbb{1} - \varepsilon_{\mathbf{k}}] \mathbf{G}_{\text{latt},\mathbf{k}}^0(\omega) = \mathbb{1}. \quad (\text{B.5})$$

So the inverse of the non-interacting lattice Green's function reads

$$\mathbf{G}_{\text{latt},\mathbf{k}}^0(\omega)^{-1} = (\omega + \mu_{\mu})\mathbb{1} - \varepsilon_{\mathbf{k}}. \quad (\text{B.6})$$

The interaction is taken into account by the local self-energy matrix $\Sigma(\omega)$, that connects the non-interacting and the interacting Green's function via the Dyson equation,

$$\mathbf{G}_{\text{latt},\mathbf{k}}(\omega)^{-1} = \mathbf{G}_{\text{latt},\mathbf{k}}^0(\omega)^{-1} - \Sigma(\omega), \quad (\text{B.7})$$

resulting in

$$\mathbf{G}_{\text{latt},\mathbf{k}}(\omega)^{-1} = (\omega + \mu_{\mu})\mathbb{1} - \varepsilon_{\mathbf{k}} - \Sigma(\omega). \quad (\text{B.8})$$

For a multi-band model with conserved total spin, we obtain a matrix representation, that is diagonal in the spin index, leading to Eq. (6.3),

$$G_{\text{latt},\mathbf{k}}^{m\sigma,m'\sigma'}(\omega)^{-1} = \langle \hat{c}_{\mathbf{k}m\sigma} \| \hat{c}_{\mathbf{k}m'\sigma'}^{\dagger} \rangle_{\omega}^{-1} = \delta_{\sigma\sigma'} [(\omega + \mu_m)\delta_{mm'} - \varepsilon_{\mathbf{k}}^{mm'} - \Sigma_{mm'}(\omega)].$$

For the one-band Hubbard model Eq. (B.8) reduces to Eq. (2.20),

$$G_{\text{latt},\mathbf{k}} = \frac{1}{\omega + \mu - \varepsilon_{\mathbf{k}} - \Sigma(\omega)},$$

with skipped spin index.

Appendix C

$G_{\text{imp}}(\omega)$ and $\Sigma(\omega)$ for a multi-band model

We want to deduce an expression for the impurity Green's function and the self-energy of a multi-band Anderson model, following an equation of motion ansatz as used by R. Bulla in [16]. For our derivation we concentrate on the model Hamiltonian

$$\hat{H}_{\text{MA}} = \hat{H}_{\text{imp}} + \hat{H}_{\text{bath}} + \hat{H}_{\text{cpl}}, \quad (\text{C.1})$$

with

$$\hat{H}_{\text{imp}} = \sum_{\tilde{\mu}} \varepsilon_d^{\tilde{\mu}} \hat{d}_{\tilde{\mu}}^{\dagger} \hat{d}_{\tilde{\mu}} + \hat{H}_U, \quad (\text{C.1a})$$

$$\hat{H}_{\text{bath}} = \sum_{k\tilde{\nu}} \varepsilon_k^{\tilde{\nu}} \hat{c}_{k\tilde{\nu}}^{\dagger} \hat{c}_{k\tilde{\nu}}, \quad (\text{C.1b})$$

$$\hat{H}_{\text{cpl}} = \sum_{k\tilde{\mu}\tilde{\nu}} V_k^{\tilde{\mu}\tilde{\nu}} (\hat{d}_{\tilde{\mu}}^{\dagger} \hat{c}_{k\tilde{\nu}} + \hat{c}_{k\tilde{\nu}}^{\dagger} \hat{d}_{\tilde{\mu}}), \quad (\text{C.1c})$$

where \hat{H}_U is an arbitrary local interaction term. Greek letters label different orbital ($m = 1, 2, \dots, M$) and spin ($\sigma = \uparrow, \downarrow$) indices: $\mu = \{m\sigma\}$.

For our derivations we start with the equation of motion for the interacting retarded impurity Green's function $G^{\mu\nu}(\omega) = \langle \hat{d}_{\mu} | \hat{d}_{\nu}^{\dagger} \rangle_{\omega}$:

$$\omega \langle \hat{d}_{\mu} | \hat{d}_{\nu}^{\dagger} \rangle_{\omega} = \langle \{ \hat{d}_{\mu}, \hat{d}_{\nu}^{\dagger} \} \rangle_T - \langle [\hat{H}, \hat{d}_{\mu}] | \hat{d}_{\nu}^{\dagger} \rangle_{\omega}. \quad (\text{C.2})$$

To reformulate the right hand side of Eq. (C.2) we insert

$$\{ \hat{d}_{\mu}, \hat{d}_{\nu}^{\dagger} \} = \delta_{\mu\nu}, \quad (\text{C.2a})$$

$$[\hat{H}_{\text{MA}}, \hat{d}_{\mu}] = \sum_{\tilde{\mu}} \varepsilon_d^{\tilde{\mu}} \underbrace{[\hat{d}_{\tilde{\mu}}^{\dagger} \hat{d}_{\tilde{\mu}}, \hat{d}_{\mu}]}_{-\delta_{\tilde{\mu}\mu} \hat{d}_{\tilde{\mu}}} + [\hat{H}_U, \hat{d}_{\mu}] \quad (\text{C.2b})$$

$$+ \sum_{k\tilde{\nu}} \varepsilon_k^{\tilde{\nu}} \underbrace{[\hat{c}_{k\tilde{\nu}}^{\dagger} \hat{c}_{k\tilde{\nu}}, \hat{d}_{\mu}]}_0 \quad (\text{C.2c})$$

$$+ \sum_{k\tilde{\mu}\tilde{\nu}} V_k^{\tilde{\mu}\tilde{\nu}} \left(\underbrace{[\hat{d}_{\tilde{\mu}}^{\dagger} \hat{c}_{k\tilde{\nu}}, \hat{d}_{\mu}]}_{-\delta_{\tilde{\mu}\mu} \hat{c}_{k\tilde{\nu}}} + \underbrace{[\hat{c}_{k\tilde{\nu}}^{\dagger} \hat{d}_{\tilde{\mu}}, \hat{d}_{\mu}]}_0 \right). \quad (\text{C.2d})$$

This leads to the equation of motion in the following form

$$\omega \langle \hat{d}_\mu \| \hat{d}_\nu^\dagger \rangle_\omega = \delta_{\mu\nu} + \varepsilon_d^\mu \langle \hat{d}_\mu \| \hat{d}_\nu^\dagger \rangle_\omega + \langle [\hat{d}_\mu, \hat{H}_U] \| \hat{d}_\nu^\dagger \rangle_\omega + \sum_{\tilde{\nu}k} V_k^{\mu\tilde{\nu}} \langle \hat{c}_{k\tilde{\nu}} \| \hat{d}_\nu^\dagger \rangle_\omega. \quad (\text{C.3})$$

$\langle \hat{c}_{k\tilde{\nu}} \| \hat{d}_\nu^\dagger \rangle_\omega$ can be expressed in terms of the on-site correlator $\langle \hat{d}_\mu \| \hat{d}_\nu^\dagger \rangle_\omega$ via the equation of motion

$$\omega \langle \hat{c}_{k\tilde{\nu}} \| \hat{d}_\nu^\dagger \rangle_\omega = \langle \{ \hat{c}_{k\tilde{\nu}}, \hat{d}_\nu^\dagger \} \rangle_T - \langle [\hat{H}_{\text{MA}}, \hat{c}_{k\tilde{\nu}}] \| \hat{d}_\nu^\dagger \rangle_\omega. \quad (\text{C.4})$$

With

$$\{ \hat{c}_{k\tilde{\nu}}, \hat{d}_\nu^\dagger \} = 0 \quad (\text{C.4a})$$

$$[\hat{H}_{\text{AM}}, \hat{c}_{k\tilde{\nu}}] = \sum_{\tilde{\mu}} \varepsilon_d^{\tilde{\mu}} \underbrace{[\hat{d}_{\tilde{\mu}}^\dagger \hat{d}_{\tilde{\mu}}, \hat{c}_{k\tilde{\nu}}]}_0 + \underbrace{[\hat{H}_U, \hat{c}_{k\tilde{\nu}}]}_0 \quad (\text{C.4b})$$

$$+ \sum_{k\tilde{\nu}} \varepsilon_k^{\tilde{\nu}} \underbrace{[\hat{c}_{k\tilde{\nu}}^\dagger \hat{c}_{k\tilde{\nu}}, \hat{c}_{k\tilde{\nu}}]}_{-\delta_{k\tilde{k}} \delta_{\tilde{\nu}\tilde{\nu}'} \hat{c}_{k\tilde{\nu}}} \quad (\text{C.4c})$$

$$+ \sum_{k\tilde{\mu}\tilde{\nu}} V_k^{\tilde{\mu}\tilde{\nu}} \left(\underbrace{[\hat{d}_{\tilde{\mu}}^\dagger \hat{c}_{k\tilde{\nu}}, \hat{c}_{k\tilde{\nu}}]}_0 + \underbrace{[\hat{c}_{k\tilde{\nu}}^\dagger \hat{d}_{\tilde{\mu}}, \hat{c}_{k\tilde{\nu}}]}_{-\delta_{k\tilde{k}} \delta_{\tilde{\nu}\tilde{\nu}'} \hat{d}_{\tilde{\mu}}} \right) \quad (\text{C.4d})$$

we get

$$\omega \langle \hat{c}_{k\tilde{\nu}} \| \hat{d}_\nu^\dagger \rangle_\omega = \varepsilon_k^{\nu'} \langle \hat{c}_{k\tilde{\nu}} \| \hat{d}_\nu^\dagger \rangle_\omega + \sum_{\tilde{\mu}} V_p^{\tilde{\mu}\nu'} \langle \hat{d}_{\tilde{\mu}} \| \hat{d}_\nu^\dagger \rangle_\omega \quad (\text{C.5})$$

and finally

$$\langle \hat{c}_{k\tilde{\nu}} \| \hat{d}_\nu^\dagger \rangle_\omega = \frac{\sum_{\tilde{\mu}} V_k^{\tilde{\mu}\nu'} \langle \hat{d}_{\tilde{\mu}} \| \hat{d}_\nu^\dagger \rangle_\omega}{\omega - \varepsilon_k^{\nu'}}. \quad (\text{C.6})$$

Inserting Eq. (C.6) into Eq. (C.3) results in

$$\omega \langle \hat{d}_\mu \| \hat{d}_\nu^\dagger \rangle_\omega = \delta_{\mu\nu} + \varepsilon_d^\mu \langle \hat{d}_\mu \| \hat{d}_\nu^\dagger \rangle_\omega + \underbrace{\langle [\hat{d}_\mu, \hat{H}_U] \| \hat{d}_\nu^\dagger \rangle_\omega}_{\equiv F_{\mu\nu}(\omega)} + \sum_{\tilde{\mu}} \underbrace{\sum_{k\tilde{\nu}} \frac{V_k^{\mu\tilde{\nu}} V_k^{\tilde{\mu}\tilde{\nu}}}{\omega - \varepsilon_k^{\tilde{\nu}}}}_{\equiv \Delta_{\mu\tilde{\mu}}(\omega)} \langle \hat{d}_{\tilde{\mu}} \| \hat{d}_\nu^\dagger \rangle_\omega, \quad (\text{C.7})$$

which can be reformulated as

$$\sum_{\tilde{\mu}} [(\omega - \varepsilon_d^\mu) \delta_{\mu\tilde{\mu}} - \Delta_{\mu\tilde{\mu}}(\omega)] \langle \hat{d}_{\tilde{\mu}} \| \hat{d}_\nu^\dagger \rangle_\omega - F_{\mu\nu}(\omega) = \delta_{\mu\nu} \quad (\text{C.8})$$

and brought into compact form using matrix notation:

$$[(\omega - \varepsilon_d^\mu) \mathbf{1} - \mathbf{\Delta}(\omega)] \mathbf{G}(\omega) - \mathbf{F}(\omega) = \mathbf{1}. \quad (\text{C.9})$$

The impurity Green's function then reads

$$\mathbf{G}(\omega)^{-1} = (\omega - \varepsilon_d^\mu) \mathbf{1} - \mathbf{\Delta}(\omega) - \mathbf{\Sigma}(\omega) \quad (\text{C.10})$$

with

$$\mathbf{\Sigma}(\omega) = \mathbf{F}(\omega) \mathbf{G}(\omega)^{-1}. \quad (\text{C.11})$$

For a multi-band model, where the total spin is conserved, we get matrix expressions, that are diagonal in the spin index, resulting in Eq. (6.7):

$$G_{\text{imp}}^{m\sigma, m'\sigma'}(\omega)^{-1} = \langle \hat{d}_{m\sigma} \| \hat{d}_{m'\sigma'}^\dagger \rangle_\omega^{-1} = \delta_{\sigma\sigma'} [(\omega + \mu_m)\delta_{mm'} - \Delta_{mm'}(\omega) - \Sigma_{mm'}(\omega)].$$

For the SIAM (with skipped spin index) the impurity Green's function simplifies to Eq. (2.36),

$$G_{\text{imp}}(\omega) = \langle \hat{d} \| \hat{d}^\dagger \rangle_\omega = \frac{1}{\omega - \varepsilon_d - \Delta(\omega) - \Sigma(\omega)},$$

with

$$\Delta(\omega) = \sum_k \frac{V_k^2}{\omega - \varepsilon_k}$$

as in Eq. (2.34). The self-energy reduces to Eq. (4.1):

$$\Sigma(\omega) = \frac{F(\omega)}{G(\omega)},$$

where $G(\omega) \equiv G_{\text{imp}}(\omega)$.

Appendix D

G_{latt} and non-interacting DOS for the Bethe lattice

In the following, we derive an analytical expression for the local retarded Green's function and the non-interacting density of states (DOS) for the one-band Hubbard model (given in Eq. (2.9)) with hopping amplitude t between nearest neighbors on a Bethe lattice in the limit of infinite coordination number $z \rightarrow \infty$.

To this end, we map the translationally invariant quantum many-body problem onto a semi-infinite chain. The Bethe lattice can be subdivided into successive shells n as in Fig. D.1. The probability $(t^*)^2$ to hop from a given shell n to shell $n+1$, as derived from the tridiagonalization for the local density of states, is given by $t^2(z-1) \stackrel{z \rightarrow \infty}{\sim} t^2 z$. Then, the Hamiltonian \hat{H} can be represented by a tridiagonal matrix with the hopping amplitude $t^* = \sqrt{zt}$ as off-diagonal elements.

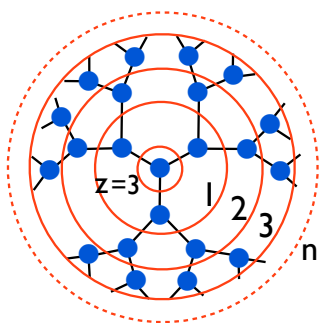


Figure D.1: The Bethe lattice, here illustrated with coordination number $z = 3$, can be subdivided into successive shells. The probability $(t^*)^2$ to hop from a given shell n to shell $n+1$ reads $t^2(z-1) \stackrel{z \rightarrow \infty}{\sim} t^2 z$ for the Bethe lattice with infinite coordination number $z \rightarrow \infty$.

Due to the tridiagonal form of \hat{H} , we can write the local retarded Green's function in terms of a continued fraction expansion (see [33, pp. 18-24]) with respect to the first site of a plain semi-infinite tight binding chain with constant hopping t^* ,

$$G_{\text{latt}}(\xi) = \frac{1}{\xi - \frac{(t^*)^2}{\xi - \frac{(t^*)^2}{\xi - \dots}}}, \quad (\text{D.1})$$

with $\xi = \omega + \mu - \Sigma(\omega)$ for a tight-binding chain including interactions by the DMFT self-energy $\Sigma(\omega)$. Defining

$$q(\xi) \equiv \frac{(t^*)^2}{\xi - q(\xi)}, \quad (\text{D.2})$$

one has a self-consistency equation in the form of a simple quadratic equation in $q(\xi)$, that can be easily solved, leading to

$$q(\xi) = \frac{1}{2} \left(\xi + \sqrt{\xi^2 - 4(t^*)^2} \right). \quad (\text{D.3})$$

Thus we obtain

$$G_{\text{latt}}(\xi) = \frac{1}{\xi - t(\xi)} = \frac{1}{2(t^*)^2} \left(\xi - \sqrt{\xi^2 - 4(t^*)^2} \right), \quad |\xi| < 2t^*. \quad (\text{D.4})$$

The sign of the square root has been chosen such that causality is preserved ($\text{Im } G_{\text{latt}}(\xi) < 0$). The non-interacting density of states is defined as

$$\rho_0^B(\varepsilon) \equiv -\frac{1}{\pi} \lim_{\delta \rightarrow 0^+} \text{Im } G_{\text{latt}}^0(\varepsilon + i\delta) \quad (\text{D.5})$$

with the positive infinitesimal δ and the non-interacting local retarded Green's function

$$G_{\text{latt}}(\varepsilon + i\delta) = \frac{1}{2(t^*)^2} \left(\varepsilon - \sqrt{\varepsilon^2 - 4(t^*)^2} \right), \quad (\text{D.6})$$

resulting in the semi-elliptic density of states

$$\rho_0^B(\varepsilon) = \frac{\sqrt{4(t^*)^2 - \varepsilon^2}}{2(t^*)^2}, \quad |\varepsilon| < 2t^*. \quad (\text{D.7})$$

With the definition of the half bandwidth $D = 2t^*$ of $\rho_0^B(\varepsilon)$, this leads to Eq. (2.27) for the DOS of the Bethe lattice in the limit of an infinite coordination number $z \rightarrow \infty$ and to Eq. (2.30) for the local lattice Green's function.

Bibliography

- [1] A. Avella and F. Mancini, editors. *Lectures on the Physics of Highly Correlated Electron Systems VIII*, volume 715 of *AIP Conference Proceedings*, 2004.
- [2] G. Kotliar and D. Vollhardt. Strongly correlated materials: Insights from dynamical mean-field theory. *Physics Today*, 57:53–59, 2004.
- [3] A. Georges, L. de’ Medici, and J. Mravlje. Strong correlations from hund’s coupling. *Annual Review of Condensed Matter Physics*, 4:137–178, 2013.
- [4] A. Georges, G. Kotliar, W. Krauth, and M. J. Rozenberg. Dynamical mean-field theory of strongly correlated fermion systems and the limit of infinite dimensions. *Rev. Mod. Phys.*, 68:13–125, 1996.
- [5] A. Weichselbaum and J. von Delft. Sum-rule conserving spectral functions from the numerical renormalization group. *Phys. Rev. Lett.*, 99:076402, 2007.
- [6] X. Deng, J. Mravlje, R. Žitko, M. Ferrero, G. Kotliar, and A. Georges. How bad metals turn good: Spectroscopic signatures of resilient quasiparticles. *Phys. Rev. Lett.*, 110:086401, 2013.
- [7] W. Metzner and D. Vollhardt. Correlated lattice fermions in $d = \infty$ dimensions. *Phys. Rev. Lett.*, 62:324–327, 1989.
- [8] A. Georges and G. Kotliar. Hubbard model in infinite dimensions. *Phys. Rev. B*, 45:6479–6483, 1992.
- [9] G. Kotliar and D. Vollhardt. Strongly correlated materials: Insights from dynamical mean-field theory. *Physics Today*, 57:53–59, 2004.
- [10] E. Pavarini, E. Koch, D. Vollhardt, and A. Lichtenstein, editors. *The LDA+DMFT approach to strongly correlated materials - Lecture Notes of the Autumn School 2011 Hands-on LDA+DMFT*, Modeling and Simulation 1, 2011.
- [11] J. Hubbard. Electron correlations in narrow energy bands. *Proceedings of the Royal Society of London. Series A. Mathematical and Physical Sciences*, 276:238–257, 1963.
- [12] R. Bulla. Dynamical mean-field theory: from quantum impurity physics to lattice problems. *Philosophical Magazine*, 86:1877–1889, 2006.
- [13] V. J. Emery, editor. *Correlated Electron Systems*, Lecture-Notes for the 9th Jerusalem Winter School for Theoretical Physics, 1993.

- [14] W. Munder. *Matrix product state calculations for one-dimensional quantum chains and quantum impurity models*. PhD thesis, Ludwig-Maximilians-Universitt Mnchen, Fakultt fr Physik, 2011.
- [15] K. G. Wilson. The renormalization group: Critical phenomena and the kondo problem. *Rev. Mod. Phys.*, 47:773–840, 1975.
- [16] R. Bulla, A. C. Hewson, and Th. Pruschke. Numerical renormalization group calculations for the self-energy of the impurity anderson model. *Journal of Physics: Condensed Matter*, 10:8365, 1998.
- [17] R. Bulla. Zero temperature metal-insulator transition in the infinite-dimensional hubbard model. *Phys. Rev. Lett.*, 83:136–139, 1999.
- [18] R. Žitko and Th. Pruschke. Energy resolution and discretization artifacts in the numerical renormalization group. *Phys. Rev. B*, 79:085106, 2009.
- [19] Th. Pruschke and R. Bulla. Hund’s coupling and the metal-insulator transition in the two-band hubbard model. *The European Physical Journal B - Condensed Matter and Complex Systems*, 44:217–224, 2005.
- [20] R. Peters and Th. Pruschke. Orbital and magnetic order in the two-orbital hubbard model. *Phys. Rev. B*, 81:035112, 2010.
- [21] R. Peters, N. Kawakami, and Th. Pruschke. Orbital order, metal-insulator transition, and magnetoresistance effect in the two-orbital hubbard model. *Phys. Rev. B*, 83:125110, 2011.
- [22] H. R. Krishna-murthy, J. W. Wilkins, and K. G. Wilson. Renormalization-group approach to the anderson model of dilute magnetic alloys. i. static properties for the symmetric case. *Phys. Rev. B*, 21:1003–1043, 1980.
- [23] R. Bulla, T. A. Costi, and Th. Pruschke. Numerical renormalization group method for quantum impurity systems. *Rev. Mod. Phys.*, 80:395–450, 2008.
- [24] A. Weichselbaum. Discarded weight and entanglement spectra in the numerical renormalization group. *Phys. Rev. B*, 84:125130, 2011.
- [25] A. Weichselbaum. Non-abelian symmetries in tensor networks: A quantum symmetry space approach. *Annals of Physics*, 327:2972 – 3047, 2012.
- [26] V. L. Campo and L. N. Oliveira. Alternative discretization in the numerical renormalization-group method. *Phys. Rev. B*, 72:104432, 2005.
- [27] R. Žitko. Adaptive logarithmic discretization for numerical renormalization group methods. *Computer Physics Communications*, 180:1271–1276, 2009.
- [28] M. Yoshida, M. A. Whitaker, and L. N. Oliveira. Renormalization-group calculation of excitation properties for impurity models. *Phys. Rev. B*, 41:9403–9414, 1990.
- [29] U. Schollwck. The density-matrix renormalization group in the age of matrix product states. *Annals of Physics*, 326:96 – 192, 2011.

BIBLIOGRAPHY

- [30] F. B. Anders and A. Schiller. Spin precession and real-time dynamics in the kondo model: time-dependent numerical renormalization-group study. *Phys. Rev. B*, 74:245113, 2006.
- [31] W. Hofstetter. Generalized numerical renormalization group for dynamical quantities. *Phys. Rev. Lett.*, 85:1508–1511, 2000.
- [32] A. Weichselbaum. Tensor networks and the numerical renormalization group. *Phys. Rev. B*, 86:245124, 2012.
- [33] G. Grosso and G. Pastori Parravicini. *Solid State Physics*. Academic Press, San Diego, London, 2. edition, 2003.
- [34] E. Müller-Hartmann. The hubbard model at high dimensions: some exact results and weak coupling theory. *Zeitschrift für Physik B Condensed Matter*, 76:211–217, 1989.
- [35] H. Bruus and K. Flensberg. *Many-Body Quantum Theory in Condensed Matter Physics*. Oxford University Press, Oxford, 8. edition, 2011.
- [36] T. Giamarchi, A. Iucci, and C. Berthod. Introduction to Many Body physics. http://dpmc.unige.ch/gr_giamarchi/Solides/Files/many-body.pdf, 2009. [Online; accessed on January 3, 2013].
- [37] S. I. Mirzaei, D. Stricker, J. N. Hancock, C. Berthod, A. Georges, E. van Heumen, M. K. Chan, X. Zhao, Y. Li, M. Greven, N. Barišić, and D. van der Marel. Evidence for a fermi liquid in the pseudogap phase of high- t_c cuprates. arXiv:1207.6704.
- [38] E. Pavarini, E. Koch, and A. I. Lichtenstein. Mechanism for orbital ordering in KCuF_3 . *Phys. Rev. Lett.*, 101:266405, 2008.
- [39] J. Kanamori. Electron correlation and ferromagnetism of transition metals. *Progress of Theoretical Physics*, 30:275–289, 1963.
- [40] F. Hund. Zur deutung verwickelter spektren, insbesondere der elemente scandium bis nickel. *Zeitschrift für Physik*, 33:345–371, 1925.
- [41] D. van der Marel and G. A. Sawatzky. Electron-electron interaction and localization in d and f transition metals. *Phys. Rev. B*, 37:10674–10684, 1988.
- [42] J. E. Han, M. Jarrell, and D. L. Cox. Multiorbital hubbard model in infinite dimensions: quantum monte carlo calculation. *Phys. Rev. B*, 58:R4199–R4202, 1998.
- [43] A. Koga, Y. Imai, and N. Kawakami. Stability of a metallic state in the two-orbital hubbard model. *Phys. Rev. B*, 66:165107, 2002.
- [44] S. Florens, A. Georges, G. Kotliar, and O. Parcollet. Mott transition at large orbital degeneracy: dynamical mean-field theory. *Phys. Rev. B*, 66:205102, 2002.
- [45] L. de’ Medici, J. Mravlje, and A. Georges. Janus-faced influence of hund’s rule coupling in strongly correlated materials. *Phys. Rev. Lett.*, 107:256401, 2011.
- [46] Ž. Osolin and R. Žitko. Padé approximants for improved finite-temperature spectral functions in the numerical renormalization group. arXiv:1302.3334.
- [47] A. Georges and M. Ferrero, 2012. internal communication.